Search for $\Lambda_c^+ \to p e^\pm \mu^\mp$ decays at LHCb

Jakub Jacek Malczewski

Henryk Niewodniczański Institute of Nuclear Physics,
Polish Academy of Sciences,
Kraków, Poland

A Dissertation for a PhD Degree

Supervisors:
prof. dr hab. Mariusz Witek, IFJ PAN, Poland
prof. Massimiliano Fiorini, UNIFE, Italy

March 27, 2025

Abstract

This thesis presents the search for the lepton-flavour violating decays of the charmed baryon, $\Lambda_c^+ \to pe^+\mu^-$ and $\Lambda_c^+ \to pe^-\mu^+$, and their charge conjugates. It is performed using 5.4 fb^{-1} of the pp collision data, collected at the centre-of-mass energy of 13 TeV by the LHCb experiment. These decays are effectively forbidden within the Standard Model, which makes them sensitive probes for effects beyond the Standard Model. Finding any significant $\Lambda_c^+ \to pe^\pm\mu^\mp$ signal would be a clear sign of New Physics.

The primary challenge in this study lies in identifying and suppressing background. The dominant background stems from frequent $\Lambda_c^+ \to p\pi^+\pi^-$ decays, with pions misidentified as leptons, and from random $pe^\pm\mu^\mp$ combinations. Multivariate classification models based on kinematical, topological and particle-identification observables are employed to reduce these backgrounds. Signal decays are identified with the reconstructed mass of the Λ_c^+ candidates, $m(\Lambda_c^+)$. The selection efficiencies for the signal and misidentified decays are determined using the calibrated simulations. Expected yields and shapes of the combinatorial background are estimated through fitting the data in the $m(\Lambda_c^+)$ sidebands, as well as the data with the wrong-charge $pe^\pm\mu^\pm$ combinations. The decay $\Lambda_c^+ \to p\phi$, with $\phi \to \mu^+\mu^-$, is chosen as the reference channel, with respect to which the branching fractions of the signal decays are measured. Selection requirements on the multivariate classifier output, and electron and muon identifications are optimised to provide the best (i.e. lowest) upper limits on $\mathcal{B}(\Lambda_c^+ \to pe^\pm\mu^\mp)$. These limits are calculated using the CLs statistical method. To avoid any experimental bias, the analysis is conducted with the $m(\Lambda_c^+)$ signal region blinded until the methods have been established and the final selection optimised. No significant signal has been observed, and the upper limits at 90% confidence level are set as:

$$\mathcal{B}(\Lambda_c^+ \to pe^+\mu^-) < 7.7 \times 10^{-8}, \text{ and } \mathcal{B}(\Lambda_c^+ \to pe^-\mu^+) < 9.5 \times 10^{-8}.$$

They are dominated by the statistical uncertainty, while the largest systematic contribution comes from the branching fraction of the reference channel. The measured limits improve those previously set by the BaBar experiment by about two orders of magnitude. The presented study is one of the most sensitive New Physics searches performed so far in the charm sector.

In addition, the thesis also presents a contribution into the development of Magnet Stations, in particular various software and simulation studies. The Magnet Stations subdetector is planned by the LHCb experiment for its Upgrade II, in order to improve the reconstruction of low-momentum particles. It will increase sensitivities of many charm studies, including future searches for $\Lambda_c^+ \to pe^\pm\mu^\mp$ decays.

Streszczenie

Niniejsza rozprawa przedstawia poszukiwanie rozpadów powabnych barionów, zachodzących z naruszeniem zasady zachowania liczby leptonowej, $\Lambda_c^+ \to pe^+\mu^-$ and $\Lambda_c^+ \to pe^-\mu^+$, oraz ich sprzężeń ładunkowych. Analiza oparta jest na danych eksperymentalnych pochodzących ze zderzeń protonów przy energii w układzie środka masy wynoszącej 13 TeV, zebranych przez eksperyment LHCb i odpowiadających zintegrowanej świetlności około 5.4 fb^{-1}. Poszukiwane rozpady są praktycznie zabronione w Modelu Standardowym, co czyni je czułymi na efekty spoza Modelu Standardowego. Zaobserwowanie znaczącego sygnału rozpadów $\Lambda_c^+ \to pe^\pm\mu^\mp$ stanowiłoby jednoznaczny efekt Nowej Fizyki.

Największym wyzwaniem w przeprowadzonej analizie jest identyfikacja i redukcja tła. Głównymi źródłami tła są częste rozpady $\Lambda_c^+ \to p\pi^+\pi^-$, w których piony są błędnie zidentyfikowane jako leptony, a także przypadkowe kombinacje $pe^\pm\mu^\mp$. Do ich stłumienia wykorzystane są modele klasyfikacji wielowymiarowej opartej na zmiennych kinematycznych, topologicznych oraz identyfikacji cząstek. Rozpady sygnałowe są identyfikowane przy użyciu zrekonstruowanej masy barionów Λ_c^+, $m(\Lambda_c^+)$. Wydajności selekcji rozpadów sygnałowych, a także tych błędnie zidentyfikowanych, są oszacowane przy pomocy skalibrowanych symulacji. Oczekiwane liczby przypadków tła kombinatorycznego, a także jego kształt są wyznaczone poprzez dopasowania do rozkładów $m(\Lambda_c^+)$ poza obszarem sygnałowym oraz do danych uzyskanych ze złych kombinacji ładunkowych $pe^\pm\mu^\pm$. Rozpady $\Lambda_c^+ \to p\phi$, gdzie $\phi \to \mu^+\mu^-$, stanowią rozpady referencyjne, względem których mierzone są stosunki rozgałęzień rozpadów sygnałowych. Selekcja w przestrzeni rozpiętej przez wynik wielowymiarowego klasyfikatora, a także zmienne identyfikacyjne elektronu i mionu, jest zoptymalizowana tak aby uzyskać najlepsze (t.j. najniższe) górne ograniczenia na częstości rozpadów sygnałowych. Ograniczenia te są wyznaczane z wykorzystaniem metody statystycznej CLs. Aby uniknąć nieprawidłowści eksperymentalnych, analiza jest prowadzona z zaślepionym obszarem sygnałowym w rozkładzie $m(\Lambda_c^+)$, aż do sfinalizowania metod pomiarowych i wyboru optymalnej selekcji. Nie zaobserwowano znaczącego sygnału dla poszukiwanych rozpadów, a górne ograniczenia na ich stosunki rozgałęzień, wyznaczone na poziomie ufności 90%, są następujące:

$$\mathcal{B}(\Lambda_c^+ \to pe^+\mu^-) < 7.7 \times 10^{-8} \text{ oraz } \mathcal{B}(\Lambda_c^+ \to pe^-\mu^+) < 9.5 \times 10^{-8}.$$

Pomiar jest zdominowany przez niepewności statystyczne, natomiast głównym źródłem niepewności systematycznych jest niepewność częstości dla rozpadów referencyjnych. Wyznaczone ograniczenia są o około dwa rzędy wielkości lepsze niż te pochodzące z wcześniejszych poszukiwań przez eksperyment BaBar. Prezentowana analiza jest jednym z najbardziej czułych poszukiwań efektów Nowej Fizyki w sektorze powabu.

Ponadto, niniejsza rozprawa prezentuje również wkład do opracowania i budowy detektora Magnet Stations, w szczególności wkład do rozbudowy jego oprogramowania i symulacji. Ten detektor jest planowany jako część detektora LHCb w jego kolejnej fazie Upgrade II, i ma na

celu poprawę rekonstrukcji cząstek o niskich pędach. Zwiększy on czułość wielu badań w sektorze powabu, w tym również przyszłe poszukiwania rozpadów $\Lambda_c^+ \to pe^\pm\mu^\mp$.

Acknowledgments

This thesis represents years of dedicated effort and could not have been realized without the invaluable support from numerous individuals and institutions.

I would like to express my gratitude to the National Science Centre NCN in Poland, for financial support under the contract no. 2018/29/B/ST2/01644. This research was also supported in part by PL-Grid Infrastructure.

I am grateful to my supervisors, Mariusz Witek and Massimiliano Fiorini, for their guidance and support. I owe a particular debt of gratitude to Jolanta Brodzicka, whose expertise and mentorship were invaluable throughout this project. I also thank Marcin Chrząszcz for his fitting advice and encouragement. Developing my skills and knowledge, in this scientific community, was a unique privilege.

I am profoundly thankful to my teachers, Agnieszka Proszek and Jacek Ślósarz, who inspired my passion for physics. Their influence has been profound in shaping my academic path. My deepest gratitude goes to my parents for their constant support and care.

Finally, I thank my wife, Anna, for her unwavering love, kindness, patience and inspiring scientific passion.

Contents

Chapter I

Introduction

A theory in physics usually aims to explain known phenomena and predict new ones. The better the theory is, the more detailed conclusion can be drawn. In particle physics, the most successful theoretical model, valid at least up to the multi-TeV energy scale, is the Standard Model (SM). It is an effective quantum field theory that describes elementary particles and their interactions. The SM was developed in the 1970's [1]–[3] and, since then, it has undergone rigorous experimental verification, with one of the most astonishing results being that on the anomalous magnetic dipole moment of a muon $(g-2)$ [4]–[6]. So far, the only *failure* of the SM is related to neutrinos, which contrary to the SM predictions, are not massless [7].

The SM has some further limitations, in particular, it neither incorporates gravity nor explains important cosmological observations. While matter and antimatter had been equally created in the Big Bang, the Universe as we know it is by far dominated by the matter. The observed matter-antimatter asymmetry cannot be explained within the SM by a charge-parity (CP) asymmetry between processes involving particles and antiparticles [8][9]. Another problem comes from the dark matter, which after almost a century of research is still not understood [10][11]. If the dark matter consists of particles, it would likely require an extension of the SM. Similarly, the dark energy, responsible for the expansion of the Universe, does not have a valid explanation [12][13].

Nowadays, the main challenge of the particle physics lays in finding effects from beyond the SM (BSM). This can be done through searching for new particles directly produced in high-energy experiments, or indirectly, through searching for deviations from the SM predictions in various physics observables. The former approach requires large enough energy to reach a new physics scale, while the latter requires precise experimental measurements and precise theoretical calculations of the SM predictions.

This thesis presents an indirect search for BSM effects by looking for a lepton-flavour violation (LFV), which is forbidden within the SM. The decays of interest, $\Lambda_c^+ \to p e^\pm \mu^\mp$,[1] have both a muon and an electron in the final state, thus they violate the lepton-flavour number. They can occur in the SM via the neutrino oscillations, but the expected rates [14]–[16] are many orders of magnitude too small to be observed in any current or feasible-future experiment; hence such processes are considered, and referred to, as *forbidden*. Because of that, these semileptonic decays of charm baryons are a clean probe of the SM. Any significant signal observed would be a sign of BSM physics. In addition, this study of charm decays is complementary to numerous LFV searches performed for beauty decays, as they may involve different BSM particles.

The structure of this thesis is as follows. Chapter **II** presents a brief introduction to the

[1] Throughout this thesis, charge conjugation is implied, unless explicitly stated otherwise.

Standard Model, focused on the lepton-flavour violation. Chapter **III** describes the experimental setup, with sections dedicated to the Large Hadron Collider (LHC), the LHCb experiment and detector, its subdetectors and their role. Chapter **IV** describes my work on a planned LHCb subdetector, which could increase sensitivity of many flavour physics measurements, including the presented one. Chapter **V** contains all the methodology of my search for $\Lambda_c^+ \to pe^\pm\mu^\mp$ decays. The results are presented in Chapter **VI**, while the summary and outlook are given in Chapter **VII**.

Statement on my contribution

This thesis project has been carried out within the LHCb collaboration, and the analysis presented here relies on a wide range on internal and external tools, developed and supported by many skilled physicists, programmers and engineers. The search for $\Lambda_c^+ \to pe^\pm\mu^\mp$ decays, being the main part of this thesis, has been carried out by myself, with a guidance from my supervisors. The only external contributions to this study involve: the production of simulation samples (Section **V.2**), and corrections to the phase-space of simulated $\Lambda_c^+ \to p\pi^+\pi^-$ background decays (Section **V.7.3**).

Throughout my PhD programme, I have contributed to the Upgrade II of the LHCb experiment [17], which will enhance the LHCb detector capabilities to a wider range of physics signatures. I have worked on software and simulation studies for the Magnet Station (MS) subdetector development (Chapter **IV**). This involves mainly: detector geometry implementation, integration with the central simulation framework, occupancy studies, spillover analysis, estimation of background sources and characteristics, optimisation of the scintillating bars' shape, implementation of a temporary energy deposition model, tracking algorithm proof of concept development, and preparation of simulated data for the detector support structure and track reconstruction efficiency optimisation. Although, the MS detector is not directly related to the $\Lambda_c^+ \to pe^\pm\mu^\mp$ search performed within this thesis, it is an important part of the LHCb upgrade programme. Therefore, selected parts of my contribution to the MS project are summarised in this thesis (Chapter **IV**).

Chapter II

Theoretical Foundations

II.1 Overview of the Standard Model

Fundamental particles in the SM, presented in Fig. **II-1**, include spin-$\frac{1}{2}$ fermions (quarks and leptons), gauge bosons mediating the elementary interactions, as well as the Higgs boson, responsible for generating particle masses. Fermions are grouped into three generations. Within each of the quark generations, there is an up-type quark (u, c, t) and a down-type quark (d, s, b), having the electric charge of $+\frac{2}{3}$ and $-\frac{1}{3}$, respectively. Each lepton generation contains a charged lepton (e, μ, τ), and a corresponding neutral lepton (ν_e, ν_μ, ν_τ).

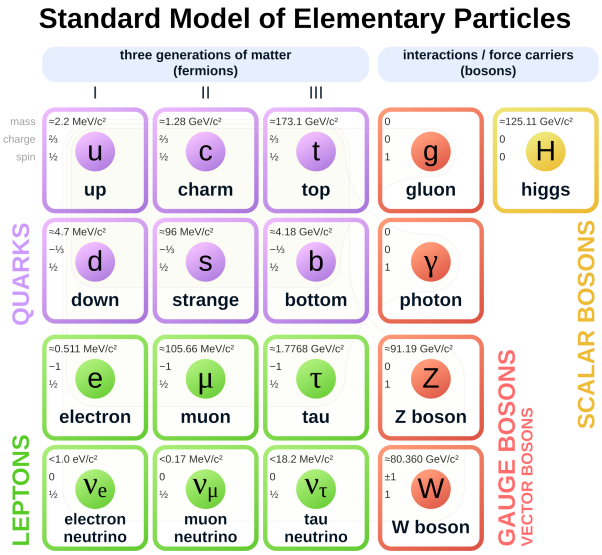

Figure **II-1**: Elementary particles in the Standard Model.

The strong interactions are mediated by gluons, and occur between gluons and quarks carrying the colour charge. The electroweak interactions involve all fermions, and are mediated by the vector bosons, γ, $W^{\pm}$ and Z^0. The scalar Higgs boson allows for the mechanism of a spontaneous symmetry breaking, in which particles obtain their masses.

II.2 The Standard Model as quantum field theory

The SM is a theoretical framework that combines Quantum Field Theory (QFT) with experimental results. It is widely accepted as the best description of the particles and their interactions at the energy scales of the current experiments. The SM was formulated between 1960 and 1980 as a result of join work of many physicists [18]. Its dynamics is described by the fundamental Lagrangian that combines: Quantum Chromodynamics (QCD), Electroweak Interactions (EW), Higgs Boson and Yukawa Interactions.

In classical mechanics, the conservation laws and equations of motion can be derived from the continuous global symmetries. Similar applies to QFT, when the Lagrangian is invariant under a local transformation, referred to as a gauge symmetry. Gauge symmetries lead to the formulation of gauge theories, such as Quantum Electrodynamics (QED) and QCD. Both of them are an integral part of the SM. The chosen transformation operator determines the properties of the corresponding Lagrangian. Those transformations can be represented as generators of Lie groups and, in principle, have to be chosen as a starting point of a given QFT. The SM consists of the symmetries defined as transformations under the three unitary groups:

$$SU(3)_C \otimes SU(2)_L \otimes U(1)_Y, \tag{II.1}$$

where C refers to the colour charge in QCD, L refers to the left chirality of fermions, and Y denotes a weak hypercharge defined as $Y = 2(Q - T_3)$, with electric charge Q and weak isospin T_3. The N in a $SU(N)$ is referred to as rank, and is related to the number of generators of such group representation, by the formula $N^2 - 1$. The $U(1)$ group has only one generator. The invariance is achieved by introducing of covariant derivatives into the Lagrangian, which are realised by adding vector gauge fields.

In general, within the SM the fields are interpreted as particles, more precisely gauge fields represent bosons that mediate interactions between fermions that themselves are described by the matter fields with the Dirac spinor form. The Dirac spinor field ψ can be decomposed into two independent components of left-handed (L) and right-handed (R) chiralities, as:

$$\psi_L = \frac{1}{2}(1 - \gamma^5)\psi \quad \text{and} \quad \psi_R = \frac{1}{2}(1 + \gamma^5)\psi. \tag{II.2}$$

In the SM, left and right chiralities are treated differently by the gauge interactions. Under the weak-isospin $SU(2)$ transformation, left-handed particles are weak-isospin doublets with $T_3 = \pm\frac{1}{2}$, and right-handed particles are singlets with $T_3 = 0$. This means that the weak interaction can transform a left-handed particle into another left-handed particle (e.g. an electron into a neutrino), but cannot do so with right-handed particles.

The gauge interactions are mediated by their corresponding bosons, which in the scope of the EW theory are massless. The introduction of the Higgs field allows for providing mass to the gauge bosons, while preserving a local gauge invariance. Through the Higgs mechanism, the initial symmetry group $SU(2)_L \times U(1)_Y$ is spontaneously broken down to the $U(1)_Q$ group associated with the electric charge. Consequently, this leads to a mixing between the gauge fields (W^1_μ, W^2_μ, W^3_μ, and B_μ) into the observable bosons (charged W^+, W^-, and neutral Z^0 and γ), as:

$$W^\pm_\mu = \frac{1}{\sqrt{2}}(W^1_\mu \pm W^2_\mu) \tag{II.3}$$

and

$$\begin{pmatrix} A_\mu \\ Z_\mu \end{pmatrix} = \begin{pmatrix} \cos\theta_W & \sin\theta_W \\ -\sin\theta_W & \cos\theta_W \end{pmatrix} \begin{pmatrix} B_\mu \\ W^3_\mu \end{pmatrix}, \tag{II.4}$$

where θ_W is the Weinberg angle, defined as the ratio of coupling constants by $\tan\theta_W = \frac{g}{g'}$. The coupling constants g and g' refer to the $SU(2)_L$ and $U(1)_Y$ group, respectively. Such $W^\pm$ and Z^0 bosons have masses and mediate the weak interactions, while γ, responsible for the electromagnetic interactions, remains massless. Although the Higgs mechanism provides the means for the massive bosons, it does not dictate the mass values. The mechanism includes the Higgs field, and the corresponding Higgs boson which couples to the weak bosons, the fermions, as well as to itself, and as such, it is responsible for generating the masses of all massive particles in the SM.

II.2.1 Quark-mixing matrix

A notable aspect of the weak interactions is how $W^\pm$ boson differently couples to different quarks, as described by the Cabibbo-Kobayashi-Maskawa (CKM) matrix:

$$V_{\text{CKM}} = \begin{pmatrix} V_{ud} & V_{us} & V_{ub} \\ V_{cd} & V_{cs} & V_{cb} \\ V_{td} & V_{ts} & V_{tb} \end{pmatrix}. \tag{II.5}$$

Given $V_{q_1 q_2}$ element of the CKM matrix represents the strength of the coupling (or mixing) between an up-type quark (q_1) and a down-type quark (q_2). It also determines the probability amplitudes for the flavour-changing transitions $q_1 \to W^+ q_2$.

The matrix elements are complex numbers, allowing for charge-parity (CP) symmetry violation in the quark sector due to a phase difference in quark transitions. The magnitudes of the CKM elements [19] are:

$$|V_{CKM}| = \begin{pmatrix} 0.97435 \pm 0.00016 & 0.22500 \pm 0.00067 & 0.00369 \pm 0.00011 \\ 0.22486 \pm 0.00067 & 0.97349 \pm 0.00016 & 0.04182^{+0.00085}_{-0.00074} \\ 0.97435^{+0.00020}_{-0.00018} & 0.4110^{+0.00083}_{-0.00072} & 0.999118^{+0.000031}_{-0.000036} \end{pmatrix}. \tag{II.6}$$

The hierarchy of the CKM matrix is such that the diagonal elements dominate, suggesting that the largest mixing is between quarks from the same generation.

II.2.2 Flavour-Changing Currents

Flavour-changing charged current transitions, such as $c \to W^+ s$ and $c \to W^+ d$, occur at a tree level, meaning they are underlain by a single CKM element, V_{cd} and V_{cs}, respectively. This is a direct consequence of the weak interaction, where a quark changes flavour while emitting (or absorbing) a $W^\pm$ boson.

On the other hand, flavour-changing neutral current (FCNC) transitions, such as $c \to u$, occur at a higher level, namely through loop diagrams involving an additional quark (d, s or b) running in a loop. Specifically, these processes require at least two CKM elements, which means they are

suppressed relative to tree-level transitions. Processes involving loop-level amplitudes are good to search for BSM effects, as some new particles can enter the loops.

II.3 Testing the SM in charm sector

The SM is extensively tested through both direct searches for BSM particles and indirect tests involving flavour observables. While the former approach requires large enough energy in the collisions to produce a wanted particle, the latter one probes the SM via precise measurements of rare or forbidden processes.

The charm sector is a good testing ground for indirect searches. It complements studies in the beauty sector, which is well established for testing flavour observables. In beauty decays, quark loops involve up-type quarks, and are significantly increased by a t quark contribution. Charm decays feature contributions to loop diagrams from down-type quarks. By analysing rare charm decays, one can investigate processes sensitive to potential BSM contributions. Such tests provide constraints on BSM effects, and thus can be useful for ruling out various theoretical models. An example of such a rare charm decay is $\Lambda_c^+ \to p\mu^+\mu^-$ involving the loop-level transitions shown in Fig. **II-2**.

Despite its potential, testing the SM in charm decays presents challenges. The lack of top-quark contribution into loop transitions, makes FCNC processes in the charm sector very suppressed. Measuring those decays is technically difficult due to their low BFs and large background from decay channels favoured by the CKM matrix elements. Precise measurements demand high statistics, excellent detector performance, and detailed analysis to suppress background and extract signal. On the theoretical side, calculating SM predictions for rare charm processes is very difficult due to, so called, long-distance contributions, which are significant as the charm quark, unlike the beauty quark, is not very heavy.

II.4 BSM searches with rare and forbidden charm decays

Rare decays are processes that occur via loop diagrams induced by EW interactions but not mediated directly through tree-level transitions. A prominent example is $\Lambda_c^+ \to p\mu^+\mu^-$ decay, which proceeds via EW loop-level amplitudes (a.k.a EW penguins) presented in Fig. **II-2**. In the SM, this decay is highly suppressed, down to the 10^{-8} level [20]. However, long-distance contributions from tree-level processes affect rare short-distance decays, complicating any interpretation of experimental results. For $\Lambda_c^+ \to p\mu^+\mu^-$ decay, these contributions arise through resonant $V \to \mu^+\mu^-$ transitions, with $V = \phi$, ρ^0, ω states, as presented in Fig. **II-3**. Such resonant $\Lambda_c^+ \to p\mu^+\mu^-$ decays have BFs at the level of 10^{-6}, thus much higher than non-resonant rare $\Lambda_c^+ \to p\mu^+\mu^-$ decays.[2] As shown in Fig. **II-4**, tails of these resonances are present in the full spectrum of the dimuon mass squared, $q^2 = m^2(\mu^+\mu^-)$. Thus, they impede an access to non-resonant $\Lambda_c^+ \to p\mu^+\mu^-$ decays occurring at the short distance.

Much cleaner probes of the SM are forbidden charm decays, in which a certain quantum number is violated. In the context of discussed BSM searches, the violation applies in particular to lepton flavour, lepton number, or baryon number. Lepton number (L) is the difference between the number of leptons and the number of antileptons in a given process (counted regardless of a lepton flavour). Baryon number (B) is defined analogously to the lepton number. Lepton flavour

[2] In the analysis presented in Chapters **V** and **VI**, $\Lambda_c^+ \to p\phi$ decay is used as the reference channel.

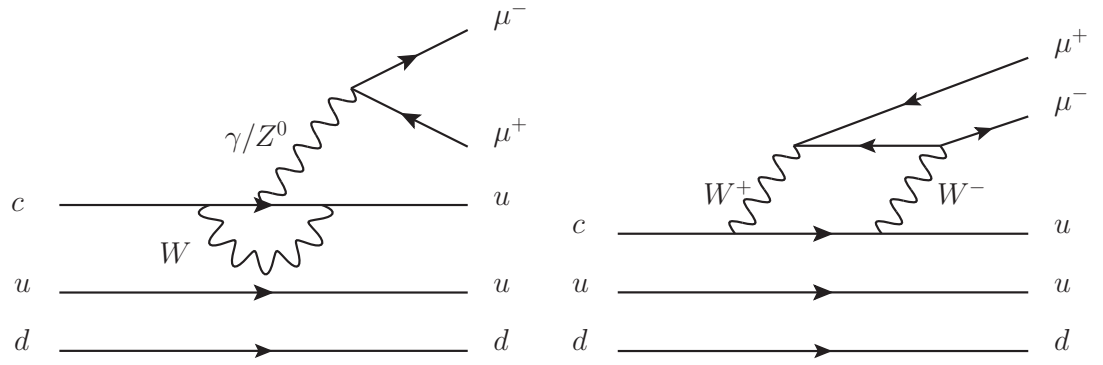

Figure **II-2**: Examples of short-distance loop-level contributions to $\Lambda_c^+ \to p\mu^+\mu^-$decay.

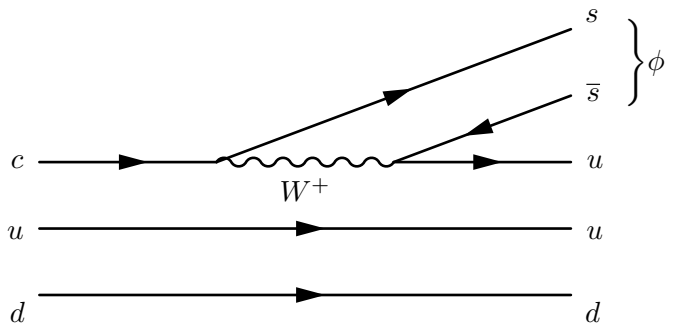

Figure **II-3**: Example of a long-distance tree-level contribution to $\Lambda_c^+ \to p\mu^+\mu^-$decay via $\phi \to \mu^+\mu^-$ resonance decay.

number is specific for leptons within each family, L_e, L_μ, L_τ. It is $+1$ for leptons, and -1 for antileptons. Thus one can define:

- **Lepton Flavour Violation** (LFV) is non-conservation of a lepton flavour number. LFV processes are, for instance, $\Lambda_c^+ \to pe^\pm\mu^\mp$, $D^0 \to e^\pm\mu^\mp$, $\mu^- \to e^-\gamma$, $\tau^- \to \mu^-\mu^+\mu^-$.
- **Lepton Number Violation** (LNV) is non-conservation of the lepton number. Example LNV processes are decays with same-sign leptons, e.g. $D^+ \to \pi^-\mu^+\mu^+$, or neutrinoless double-beta decay $2n \to 2p2e^-$.
- **Baryon Number Violation** (BNV) is non-conservation of the baryon number. BNV processes are, for example, $\Lambda_c^+ \to \bar{p}\mu^+\mu^+$, $\Lambda_c^+ \to \bar{p}e^+\mu^+$, $p \to e^+\pi^0$. BNV processes are often also LNV or LFV ones.

In the SM, LNV and BNV are forbidden due to the absence of any mechanism that can induce such transitions. LFV is allowed for neutrinos through oscillations; for example, a muonic neutrino can change into an electron/tau neutrino over time, making it not strictly forbidden. However, such a neutral lepton flavour violation (NLFV) is highly suppressed in the SM.[3] Consequently, processes with charged lepton flavour violation (CLFV), like $D^0 \to e^\pm\mu^\mp$, can proceed through $\nu_\mu - \nu_e$ neutrino oscillations, but their rates are tens of orders below the reach of any feasible experiment. Thus, CLFV channels are generally considered as effectively forbidden. LFV, LNV

[3]Massive neutrinos are now considered a part of the SM.

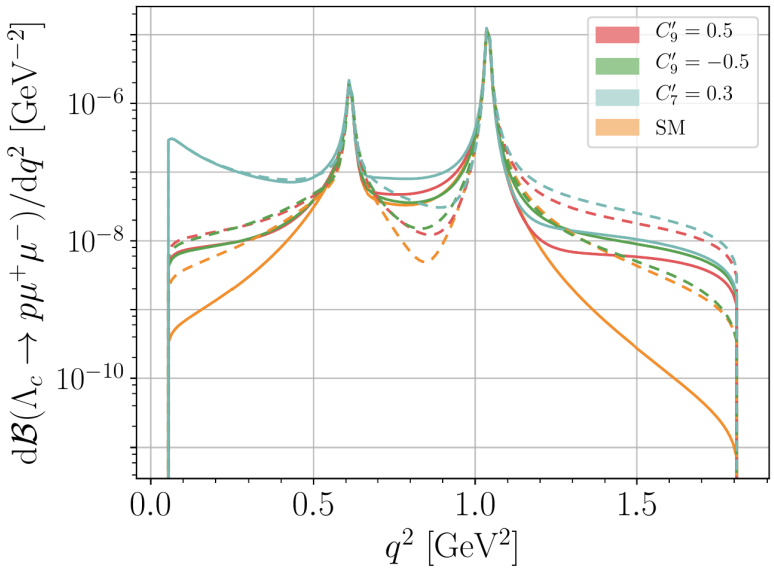

Figure **II-4**: The differential BF as a function of $q^2 = m^2(\mu^+\mu^-)$ for resonant $\Lambda_c^+ \to p\mu^+\mu^-$ decays in (orange) SM and various BSM scenarios. Taken from Ref. [20].

and/or BNV processes are allowed in various BSM models and some of the predicted rates are already within reach of current experiments.

The primary advantage of studying forbidden decays lies in the absence of any SM contributions, making these channels an ideal tool for BSM searches. Unlike rare charm decays, which require model-dependent methods to isolate BSM signals from long-distance effects, forbidden decays do not suffer from this problem: any significant signal observed is a clear BSM sign. This lack of the SM background simplifies BSM searches and enhances their sensitivity.

II.4.1 Experimental status of rare/forbidden charm decays with leptons

One of the most important results in rare charm decays comes from the first observation of the $D^0 \to \pi^+\pi^-\mu^+\mu^-$ decay in the dimuon-mass region below $V \to \mu^+\mu^-$ resonances [21]. This measurement was performed by LHCb using pp collision data collected between 2011 and 2016, and corresponding to integrated luminosity of 2 fb^{-1}. It is the rarest charm decay observed so far, with BF at the 10^{-8} level. However, it most likely includes a significant resonant contribution. There is an evidence for the $D^0 \to K^+K^-\mu^+\mu^-$ decay [21], while other rare or forbidden charm decays involving leptons have only upper limits (ULs) set. Some of them are given in Table **II-1**. In general, decays with muons have better (lower) ULs, than decays with electrons in the final state. At LHCb, any measurement involving electrons is more complicated due to backgrounds from hadrons and photons in the calorimeters, which is not the case for the muon detector. This is discussed in more detail in Chapter **III**.

In addition to BFs, other observables have been also tested for $D^0 \to \pi^+\pi^-\mu^+\mu^-$ and $D^0 \to K^+K^-\mu^+\mu^-$ decays. Namely, forward-backward asymmetry, triple-product asymmetry and CP asymmetry, measured in dimuon-mass regions dominated by resonances and away from them [37]. These observables have been measured to be consistent with the SM predictions, up to the current experimental sensitivity.

Decay	SM BF	BF or UL at 90% CL	Experiment
EW penguins			
$D^0 \to \pi^+\pi^-\mu^+\mu^-$	$O(10^{-9})$ [22][23]	$(7.8 \pm 1.9 \pm 0.5 \pm 0.8) \times 10^{-8}$	LHCb [21]
$D^0 \to K^+K^-\mu^+\mu^-$		$(2.6 \pm 1.2 \pm 0.2 \pm 0.3) \times 10^{-8}$	LHCb [21]
$D^+ \to \pi^+\mu^+\mu^-$	$O(10^{-9})$ [24][25][26][27]	$< 6.7 \times 10^{-8}$	LHCb [28]
$D^+ \to \pi^+e^+e^-$		$< 1.1 \times 10^{-6}$	BaBar [29]
$D^+ \to K^+\mu^+\mu^-$		$< 5.4 \times 10^{-8}$	LHCb [28]
$D^+ \to K^+e^+e^-$		$< 85 \times 10^{-8}$	LHCb [28]
$D_s^+ \to \pi^+\mu^+\mu^-$		$< 18 \times 10^{-8}$	LHCb [28]
$D_s^+ \to \pi^+e^+e^-$		$< 5.5 \times 10^{-8}$	LHCb [28]
$D_s^+ \to K^+\mu^+\mu^-$		$< 14 \times 10^{-8}$	LHCb [28]
$D_s^+ \to K^+e^+e^-$		$< 3.7 \times 10^{-6}$	BaBar [29]
$\Lambda_c^+ \to p\mu^+\mu^-$		$< 2.9 \times 10^{-8}$	LHCb [30]
$D^0 \to \mu^+\mu^-$	$O(10^{-13})$ [31][32]	$< 3.1 \times 10^{-9}$	LHCb [33]
$D^0 \to e^+e^-$		$< 7.9 \times 10^{-8}$	Belle [34]
LFV or LNV			
$D^0 \to e^\pm\mu^\mp$	0	$< 1.3 \times 10^{-8}$	LHCb [35]
$D^+ \to \pi^-\mu^+\mu^+$		$< 1.4 \times 10^{-8}$	LHCb [28]
$D_s^+ \to K^-\mu^+\mu^+$		$< 2.6 \times 10^{-8}$	LHCb [28]
$D^0 \to K^-K^-\mu^+\mu^+$		$< 1.0 \times 10^{-7}$	BaBar [36]
$D^0 \to K^-K^-e^+e^+$		$< 3.4 \times 10^{-7}$	BaBar [36]
$\Lambda_c^+ \to pe^+\mu-$		$< 9.9 \times 10^{-6}$	BaBar [29]
$\Lambda_c^+ \to pe^-\mu+$		$< 1.9 \times 10^{-5}$	BaBar [29]

Table **II-1**: Selected results on rare or forbidden charm decays involving leptons. The most precise BF or best UL at 90% confidence level (CL) is given for each channel. Measurements for three- and four-body channels involving a $\mu^+\mu^-$ or e^+e^- pair, have excluded dilepton mass regions dominated by resonances. BFs for $D^0 \to \pi^+\pi^-\mu^+\mu^-$ and $D^0 \to K^+K^-\mu^+\mu^-$ decays are measured for $m(\mu^+\mu^-) < 525$ MeV.

II.5 $\Lambda_c^+ \to pe^\pm\mu^\mp$ decays

The process studied in the presented thesis is $\Lambda_c^+ \to pe^\pm\mu^\mp$. These decays involve both an electron and a muon in the final state, without corresponding neutrinos, making them CLFV channels. As explained in Section **II.4**, CLFV processes are highly suppressed within the SM, with the only SM contribution coming from neutrino oscillations. A diagram for such a transition is presented in Fig. **II-5**. The decay rate resulting from this SM contribution is negligibly small.

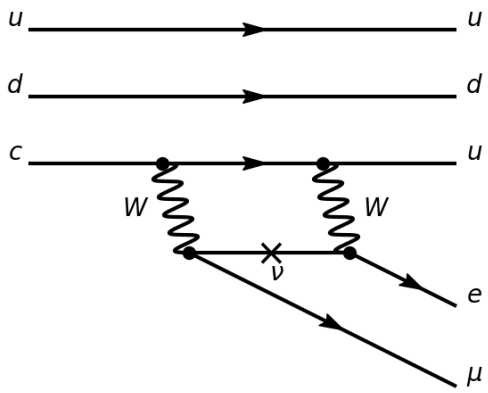

Figure **II-5**: The SM contribution to $\Lambda_c^+ \to pe^\pm\mu^\mp$ decays through $\nu_\mu - \nu_e$ neutrino oscillations.

Various BSM models allow for non-negligible contributions to $\Lambda_c^+ \to pe^\pm\mu^\mp$. Several relevant theoretical models include: leptoquarks (LQs), supersymmetry (SUSY), and additional heavy Z^0 boson (Z'). These models can introduce new couplings that enhance CLFV processes. Figure **II-6** shows predicted BFs of $\Lambda_c^+ \to pe^\pm\mu^\mp$ decays in various BSM scenarios. The most favourable model involves a hypothetical particle - leptoquark, which carries both lepton and baryon number [38]. It is expected to decay into a quark (or anti-quark) and a lepton, charged or neutral. A leptoquark carries colour and electric charge. To conserve the electric charge, a leptoquark must have a charge that is equal to the sum of its decay products' charges, which results in Q_{LQ} equal to $\pm 5/3$, $\pm 4/3$, $\pm 2/3$ or $\pm 1/3$, depending on a quark-lepton combination.

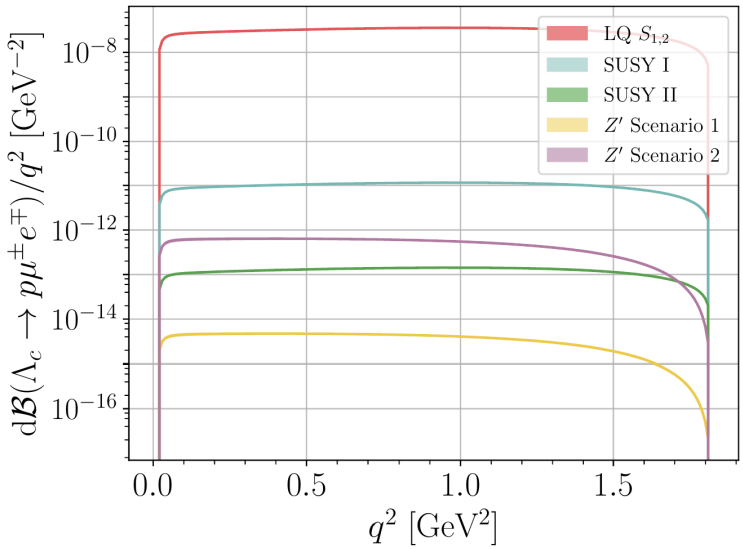

Figure **II-6**: The differential BF as a function of $q^2 = m^2(e^\pm\mu^\mp)$ for $\Lambda_c^+ \to pe^\pm\mu^\mp$ decays in various BSM models: leptoquark, SUSY (I) with and (II) without R-parity violation, and two different Z' scenarios. Taken from Ref. [20].

The current ULs on BFs of $\Lambda_c^+ \to pe^\pm\mu^\mp$ decays were set by the BaBar experiment [29]:

$$\begin{aligned}\mathcal{B}(\Lambda_c^+ \to pe^+\mu^-) &< 9.9 \times 10^{-6} \text{ at } 90\% \text{ CL},\\ \mathcal{B}(\Lambda_c^+ \to pe^-\mu^+) &< 1.9 \times 10^{-5} \text{ at } 90\% \text{ CL}.\end{aligned} \tag{II.7}$$

The ULs are set independently on the two charge combinations as, in principle, different BSM models may distinguish them by favouring one over the other. The current ULs are about two orders of magnitude above the most favourable BSM scenario with LQs. With the data collected by the LHCb experiment, one can expect to reach a sensitivity level needed to verify this LQ model.

Chapter III

Experimental environment

III.1 The Large Hadron Collider

The Large Hadron Collider (LHC) is a particle collider with the highest, at the time of writing, centre-of-mass (cms) energy in the world. It is capable of delivering proton beams with energy up to 6.8 TeV, which results in collisions at $\sqrt{s} = 13.6$ TeV. The LHC ring is placed underground and have the circumference of 27 km. The entire LHC complex contains two linear accelerators that are responsible for the initial acceleration of protons or heavy ions, and three synchrotrons that increase beam energy before the final injection into the LHC ring. Four big experiments are taking advantage of the LHC beam: Atlas, Alice, CMS and LHCb. Atlas and CMS are general-purpose detectors designed to study highly massive particles and their interactions. Their most famous results include the discovery of the Higgs boson in 2012. Alice is focused on heavy-ion collisions and studying of the quark-gluon plasma properties. The main goal of the LHCb experiment is to study particles that contain heavy quarks, b or c.

The data taking periods are called *runs* and last for a few years. The LHC finished two runs: Run-1, with the proton-proton (pp) collisions at $\sqrt{s} = 7$ and 8 TeV, took place during 2010-2013, and Run-2 with $\sqrt{s} = 13$ TeV during 2015-2018. Throughout the downtime, upgrades and maintenance tasks were carried out, thanks to which the LHC performance improved. In 2022, the LHC started its Run-3 with pp collisions at $\sqrt{s} = 13.6$ TeV. The data sample used in the presented analysis is from 2016-2018 period of Run-2.

During Run-1 and Run-2, the LHCb experiment operated at the instantaneous luminosity of $\mathcal{L} \simeq (2-4) \times 10^{32}$ cm^{-2}s^{-1}, which is lower than the nominal luminosity intended for experiments like Atlas and CMS ($\mathcal{L} \simeq 10^{34}$ cm^{-2}s^{-1}). This reduction was achieved by adjusting the beam focus at the LHCb collision point, thereby significantly decreasing the number of *pile-up* events caused by multiple proton-proton collisions within a single bunch crossing. This lower luminosity is necessary for effectively collecting and analysing data from decays of beauty and charm particles. In Run-3, the luminosity for LHCb was increased to about 2×10^{33} cm^{-2}s^{-1}.

III.2 The LHCb experiment

The LHCb detector is a single-arm forward spectrometer with an acceptance and capabilities complementary to the Atlas and CMS detectors, which cover almost the full solid angle. It was optimized for studying beauty and charm hadrons, which are produced in pp collisions at the small angle with respect to the beam direction. The forward LHCb configuration, covering pseu-

dorapidity range of $2 < \eta < 5$, assures that about 30% of the produced heavy hadrons are within the LHCb acceptance.

III.2.1 Charm data samples at LHCb

Due to the large cross-section for charm production in pp collisions, LHCb has collected the world's largest sample of charm hadrons. Consequently, LHCb is considered as a *charm factory*. The cross-section for producing a charm hadron within the LHCb acceptance region is approximately 1400 μb at $\sqrt{s} = 7\,\text{TeV}$ [39] and about 2400 μb at $\sqrt{s} = 13\,\text{TeV}$ [40]. This value is one order of magnitude larger than the cross-section for producing beauty hadrons, which is around 100 μb [41].

The primary production of charm hadrons directly from *pp* collisions is the dominant process at the LHC. Given that both colliding particles are protons, this *prompt* production exhibits asymmetry: more charm baryons than anti-baryons are produced, and fewer charm mesons than anti-mesons to maintain zero charm content in the initial *pp* system. The production asymmetry for charm mesons is measured to be at the percent level [42][43]; no measurement exists for charm baryons.

Another production process used at LHCb is *secondary* production, in which charm hadrons originate from decays of beauty hadrons. For Λ_c^+ baryons, the dominant secondary sample comes from decays of Λ_b^0 baryons. Any secondary charm sample is smaller than the corresponding prompt sample, due to the lower beauty cross-section. In most of the LHCb studies exploiting the prompt sample, such as the analysis presented in this thesis, any secondary charm contribution is considered as background and suppressed. The suppression relies on distinct topologies of the two samples: secondary charm hadrons are more displaced from the *pp* interaction point than prompt ones, due to the large lifetime of beauty hadrons. If a secondary contribution was retained, and secondary hadrons were reconstructed assuming that they were produced from the *pp* interaction point, an analysis could suffer from sub-optimal selection or even experimental biases.

III.2.2 The LHCb detector

The LHCb detector is composed of various subdetectors that allow for a reconstruction of particle properties, such as: trajectory (track), velocity, energy, electric charge and mass. Relatively stable particles, such as pions, electrons and muons, are measured directly, while particles that decay before reaching subdetectors are reconstructed from their decay products. Each of them is first reconstructed independently, then the particles are combined to find a decay-vertex position, which is necessary to correctly calculate the momentum and the invariant mass of the mother particle. An uncertainty associated with such a measurement comes from a global fit, which includes all the information from the associated decay products.

Precise studies of decays of heavy hadrons require that their decay vertices and impact parameters (IPs)[4] of daughter tracks are measured with high resolutions. This allows to identify (relatively) long-lived heavy particles, and distinguish them from background due to random combinations of tracks that are consistent with being produced from initial *pp* collisions. Also, particle momenta have to be measured with an excellent resolution, so that the invariant mass of decay products can be precisely reconstructed. As a result, a signal decay of interest can be identified with good efficiency and purity. Finally, precise identification of various (meta-)stable

[4]IP is defined as the distance of the closest approach (DOCA) of a particle track to its origin vertex.

particles is necessary in order to discriminate between heavy-hadron decays to final states of similar topologies. The LHCb detector meets all these requirements.

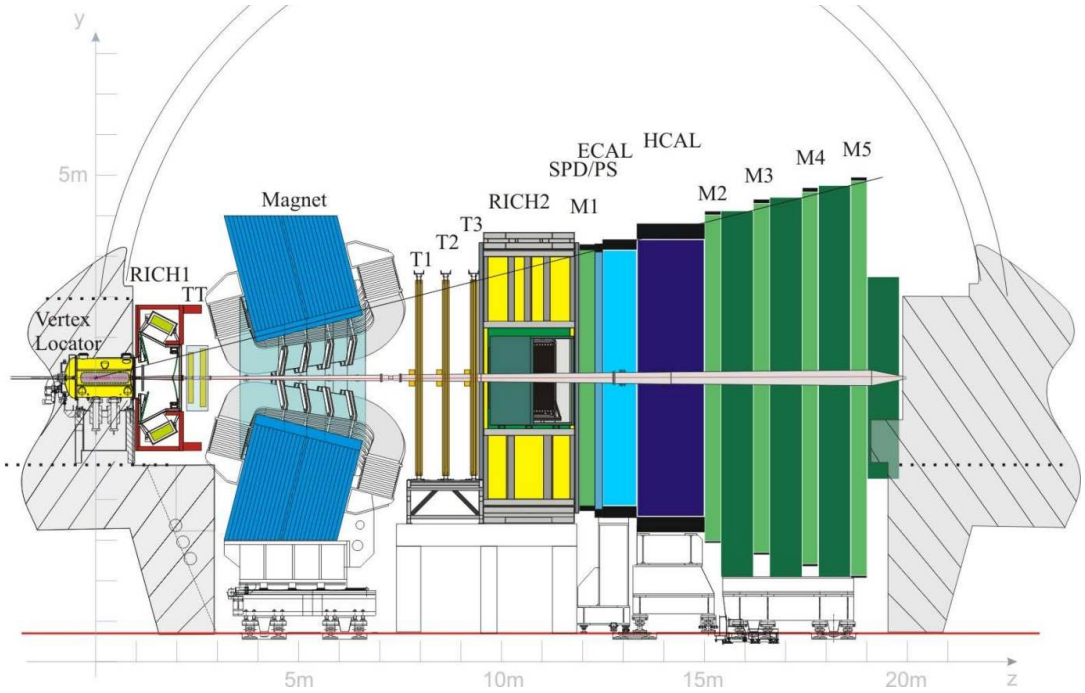

Figure **III-1**: Side-view layout of the LHCb detector during Run-1 and Run-2 [44]. The detector is composed of: Vertex Locator (VELO), RICH1, Trigger Tracker (TT), Magnet, Tracking Stations (T1–T3), RICH2, Scintillating Pad Detector (SPD), Preshower Detector (PS), ECAL, HCAL and Muon Stations (M1–M5).

The layout of the LHCb detector is shown in Fig.**III-1**. The primary *pp* collision, associated with primary vertex (PV), occurs inside Vertex Locator (VELO). Produced particles traverse first of the two Ring Imaging Cherenkov detectors (RICH1) and Trigger Tracker (TT), where charged particles start to interact with the magnetic field provided by the LHCb magnet. After the magnet, particles pass through the three Tracking Stations, RICH2, Preshower (PS) and the Scintillating Pad Detector (SPD). Then, particle energy is measured in the electromagnetic and hadronic calorimeters (ECAL and HCAL). At the end of the spectrometer, muons are measured in Muon Stations.

VELO, TT and Tracking Stations comprise the tracking system, which reconstructs tracks formed by charged particles, measures their momenta using the magnetic field to bend them, and reconstructs decay vertices. On the other hand, RICH1 and RICH2, the full calorimeter system (SPD/PS, ECAL and HCAL) and Muon Stations comprise the particle identification (PID) system at LHCb. It allows for distinguishing between various types of charged particles by combining information on measured momentum and velocity or energy. Neutral particles (photons and neutral pions) are identified using information from SPD/PS and ECAL.

All the mentioned subdetectors are described in more detail in the following sections. The presented description does not include the changes introduced between 2019-2021 for Run-3 [45].

III.2.3 Vertex Locator

VELO is positioned closest to the beam, and has the best spatial resolution. It consists of 42 double-sided silicon modules arranged in pairs of the semi-circular sensors (Fig. **III-2**) installed perpendicularly to the beam axis [46]. One side of each module has silicon micro-strips arranged radially to measure the angular position, while the other side is arranged in rings to measure the radial coordinate. The sensors are placed around the interaction point, and cover a wider acceptance along the beam direction than the other LHCb subdetectors. Charged particles interact electromagnetically with a semiconductor depletion region, generating currents in each strip independently. Those electric signals are then amplified, digitized and registered. The active material budget of this detector was minimized to reduce a probability of nuclear interactions of detected particles, to avoid generating undesired background.

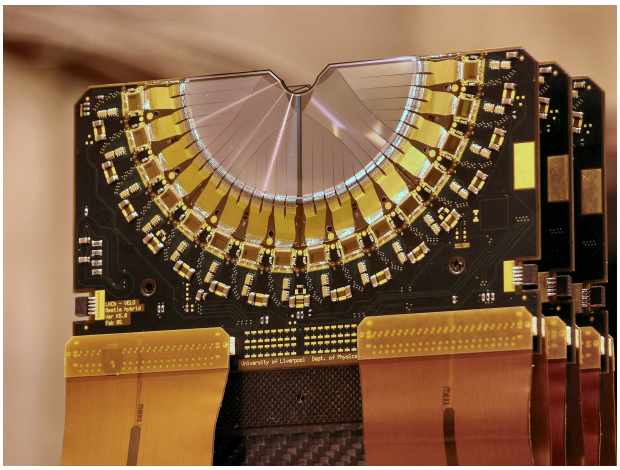

Figure **III-2**: VELO sensors. Picture taken from Ref. [47].

The spatial resolution of the VELO detector is high enough to measure a PV, as well as decay vertex of a heavy hadron, called secondary vertex (SV). The typical PV resolution is between 9 and 35 μm for the x and y, and between 50 and 280 μm for the z coordinate[5], depending on how many tracks are used in the PV reconstruction. In the presented work, this feature is especially useful in order to distinguish between Λ_c^+ baryons produced promptly at PV from those originating from decays of $\Lambda_b^0 \to \Lambda_c^+ X$.

III.2.4 RICH detectors

RICH1 is placed right behind VELO, whereas RICH2 about 10 m from the pp collision point. The main task of these subdetectors is to provide information about the hadron velocity for the PID purpose. They exploit the Cherenkov radiation i.e. the emission of photons by a charged particle moving faster than the speed of light in a given medium. The direction of the emission is strictly related to the particle velocity, and allows for distinguishing between particles with similar momenta, but different masses. In Run-2, both RICH1 and RICH2 were filled with (different) gas mixtures. RICH1 covers a momentum range from 1 to 60 GeV,[6] whereas RICH2 is able to provide a good particle discrimination up to 100 GeV [46].

[5]The LHCb coordinate system has the origin at the pp collision point, the z axis is along the beam direction, the y axis points vertically upwards, and the x axis points horizontally towards the LHC centre.

[6]Natural units with $\hbar = c = 1$ are used in this thesis.

III.2.5 Tracking Stations

The LHCb tracking system is designed around the central dipole magnet. The magnetic field is along the y direction and bends trajectories of charged particles in the x-z plane, with a bending power of 4 Tm. This is exploited to measure a particle momentum: the greater the momentum, the smaller the trajectory curvature.

The tracking system consists of TT placed upstream the magnet, and three Tracking Stations (T1-T3) located downstream the magnet. Each station is divided, according to the distance from the beam, into Inner Tracker (IT) and Outer Tracker (OT). The positions and relative sizes of IT and OT are shown in Fig. **III-3**. TT and IT are based on silicon micro-strip detectors, whereas OT on gaseous drift tube detectors. IT and OT are placed at the same z, and are complementary to each other. IT is situated closer to the beam axis, where the increased occupancy would overwhelm OT. While less accurate, the gaseous drift tube technology used in OT is much more cost-efficient.

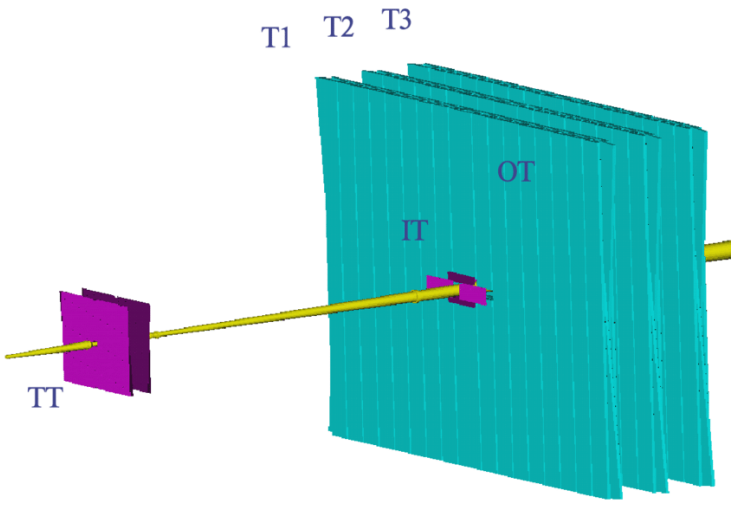

Figure **III-3**: The LHCb tracking system [48].

Charged particles traversing the tracking subdetectors deposit energy in their sensitive layers. These energy deposits are referred to as *hits*. When reconstructing charged-particle tracks, one can use hits detected in various subdetectors of the tracking system. This specifies the range of tracks, depending on which one can characterize: VELO tracks, upstream tracks, downstream tracks, T-tracks and long tracks, as shown in Fig. **III-4**. During the reconstruction of a collision event, upstream tracks and T-tracks are matched together to form long tracks, which are used in most of the LHCb studies, including the presented one. The relative momentum resolution for the long tracks is about 0.5% for particles with $p < 10$ GeV, and about 2% at 200 GeV. With the current LHCb configuration, low-momentum particles are often bent out of the LHCb acceptance, and thus do not form a long track. The particle momentum measured for upstream tracks carries an uncertainty of about 20% [49]. A possible solution to this problem is presented in Chapter **IV**.

The tracking efficiency is defined as the probability that the trajectory of a charged particle passing through the entire tracking system is successfully reconstructed. This definition does not include effects such as interactions with material, decays in flight, or particles that fly outside the detector acceptance. For muons produced in $J/\psi \to \mu^+\mu^-$ decays, the tracking efficiency is

measured to be above 96% [50]. Similar measurement for electrons from $J/\psi \to e^+e^-$ decays, results in the tracking efficiency being about 80% for electrons with the transverse momentum (p_T) above 1 GeV, and significantly decreasing for the lower-p_T electrons [51].

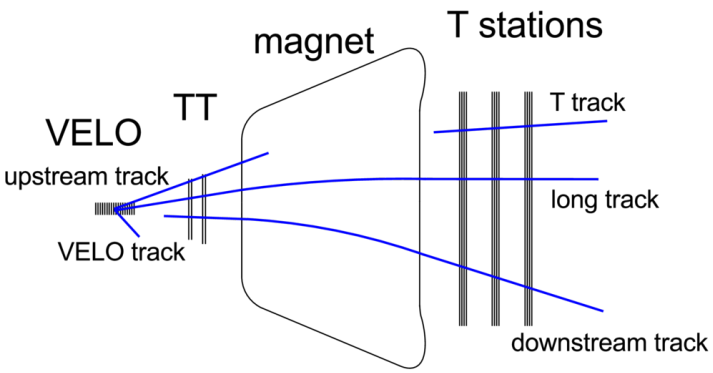

Figure **III-4**: Track types reconstructed at the LHCb tracking system [50].

III.2.6 Calorimeter system

The LHCb calorimeter system is composed of SPD, PS, ECAL for electromagnetically interacting particles (electrons and photons) and HCAL for hadronic particles. Both, ECAL and HCAL are designed around a scintillating material that converts particle energy into light, whose intensity is then measured. To stimulate generation of particle showers, the scintillating material is placed alternately with layers of lead. The generated light is transported to photo-multipliers via fiber optics. The spatial resolution of the measurement comes from the segmentation of the scintillator. Calorimeter cells closer to the beam pipe have higher granulation. For ECAL the size of a cell is equal to 4×4, 6×6 or 12×12 cm^2, and for HCAL it is 13×13 and 26×26 cm^2.

Additionally, the functionality of ECAL is extended by SPD and PS, which are situated just before ECAL. The SPD/PS detector comprises two scintillator pads separated by a layer of lead, which initiates photon conversions. SPD identifies charged particles, and allows electrons to be separated from photons, whereas PS identifies electromagnetic particles by distinguishing them from charged hadrons.

Measurement of energy in the calorimeter system starts from clustering, namely cells that have energy deposits are grouped together to form clusters. A single cluster comprises 3×3 cells around the cell with the largest local energy deposit. Each cluster is characterized by its total energy, energy-weighted position and various shape parameters on the x-y plane. Similar method is used in PS, ECAL and HCAL. A simpler, 2×2 clusters are considered in HCAL for the triggering purpose (Section **III.2.9**).

ECAL measures energy (E) of electromagnetic showers. Its resolution is $\sigma(E)/E = 10\%/\sqrt{E} \oplus 1\%$, where E is given in GeV, and $\oplus$ denotes the sum in quadrature. The main task of HCAL is to measure energy of hadronic showers, which is important for the hardware-level trigger (Section **III.2.9**). The energy resolution of HCAL is quite limited, and amounts to $\sigma(E)/E = 69\%/\sqrt{E} \oplus 9\%$.

III.2.7 Muon detector

At the energy range typical for LHCb, muons are relatively low interacting particles. To identify muons, and properly measure their tracks and energies, the LHCb detector is equipped with the dedicated Muon Stations. They also provide fast information on high-p_T muons to the hardware-level trigger (Section **III.2.9**). The first station, M1, is located before the calorimeters to minimize multiple scattering and improve p_T resolution. The remaining stations, M2 through M5, are located after HCAL, where muons dominate.

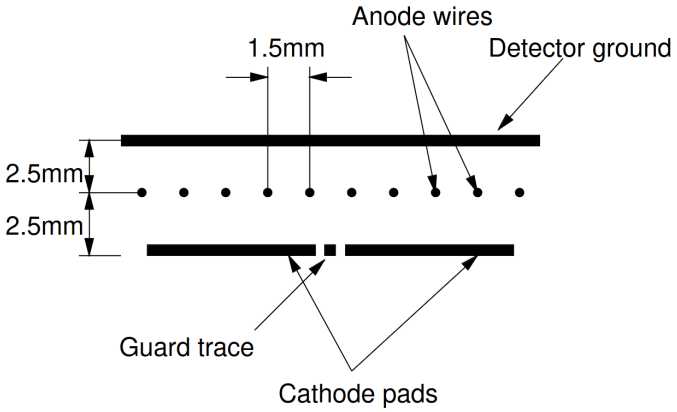

Figure **III-5**: Schematic diagram of one sensitive gap in a multi-wire proportional chamber of the muon detector [52].

The sensitive parts of the muon detector consist of gaseous chambers; their design is outlined in Fig. **III-5**. Particles passing through the chambers ionize gas along their trajectories. Due to applied electric field, electrons are collected by the wires, while positive ions by the pads. The pads and wires are spread along different directions to assure measuring x and y coordinates of hits. Between M2-M5 stations, 80 cm-thick iron plates are inserted, corresponding in total to about 20 nuclear-interaction lengths for muons [52]. Muon Stations have adjusted segmentation, increasing with the distance from the beam, to compensate for an uneven occupancy.

III.2.8 Particle identification

PID is performed at LHCb using information from the RICH detectors, the calorimeter system and Muon Stations. Charged particles to identify are: e, μ, π, K and p. These particle hypotheses are tested for each detected track. This is done by calculating a likelihood function that describes a probability that a given track is an electron, muon, etc., considering the properties measured in the mentioned subdetectors. Such a likelihood is the product of independent likelihoods for individual subdetectors [46], as following:

$$\begin{aligned}
\mathcal{L}(e) &= \mathcal{L}^{\mathrm{RICH}}(e)\,\mathcal{L}^{\mathrm{CALO}}(e)\,\mathcal{L}^{\mathrm{MUON}}(\text{non } \mu)\,, \\
\mathcal{L}(\mu) &= \mathcal{L}^{\mathrm{RICH}}(\mu)\,\mathcal{L}^{\mathrm{CALO}}(\text{non } e)\,\mathcal{L}^{\mathrm{MUON}}(\mu)\,, \\
\mathcal{L}(h) &= \mathcal{L}^{\mathrm{RICH}}(h)\,\mathcal{L}^{\mathrm{CALO}}(\text{non } e)\,\mathcal{L}^{\mathrm{MUON}}(\text{non } \mu)\,,
\end{aligned} \tag{III.1}$$

where h refers to hadron species, pion, kaon or proton. The particle hypothesis chosen as the best for a given track, is the one giving the largest likelihood value.

Physics analyses use a PID classifier which discriminates between different particle hypotheses. Usually it is defined as the log-likelihood difference between two particle hypotheses, $p1$ and $p2$, namely $\mathrm{DLL}_{p1,p2} = \log \mathcal{L}(p1) - \log \mathcal{L}(p2)$. Another group of PID classifiers are `ProbNN` variables. Those are based on Deep Neural Networks, tasked with distinguishing between a given particle type and all other species. This approach improves the PID efficiency over the standard $\mathrm{DLL}_{p1,p2}$ method [53]. The presented analysis relies on the `ProbNNmu`, `ProbNNe` and `ProbNNp` variables, for the final PID selection.

Within $\mathcal{L}^{\mathrm{RICH}}$ in Eq. **III.1**, RICH provides an information about rings of the Cherenkov light measured from positions of activated photon detectors. They are compared against a prediction for each particle species depending on the particle momentum. Electron and non-electron hypotheses in $\mathcal{L}^{\mathrm{CALO}}$ are based on energy deposits in the calorimeter system, as well as on matching between ECAL clusters and any track reconstructed in the tracking system. Muon and non-muon hypotheses in $\mathcal{L}^{\mathrm{MUON}}$ are estimated through matching of energy deposits measured in Muon Stations with reconstructed long and downstream tracks.

Let us consider the electron identification procedure, which relies primarily on $\mathcal{L}^{\mathrm{CALO}}$ (Eq. **III.1**). It is evaluated using the E/p ratio of the energy measured in ECAL and the momentum measured in the tracking system. As shown in Fig. **III-6** (left), this ratio is close to unity for electrons, and is significantly smaller for hadrons, which deposit most of their energy in HCAL. Another highly discriminating quantity is χ^2 derived from the cluster-track matching. To calculate this χ^2, an expected cluster position in ECAL is extrapolated based on the measured particle trajectory, and compared to the centre of the measured energy cluster. Additionally, the information about any associated energy deposits in PS and HCAL is also considered. As shown in Fig. **III-6** (right), this identification procedure leads to efficient discrimination between electrons and hadrons.

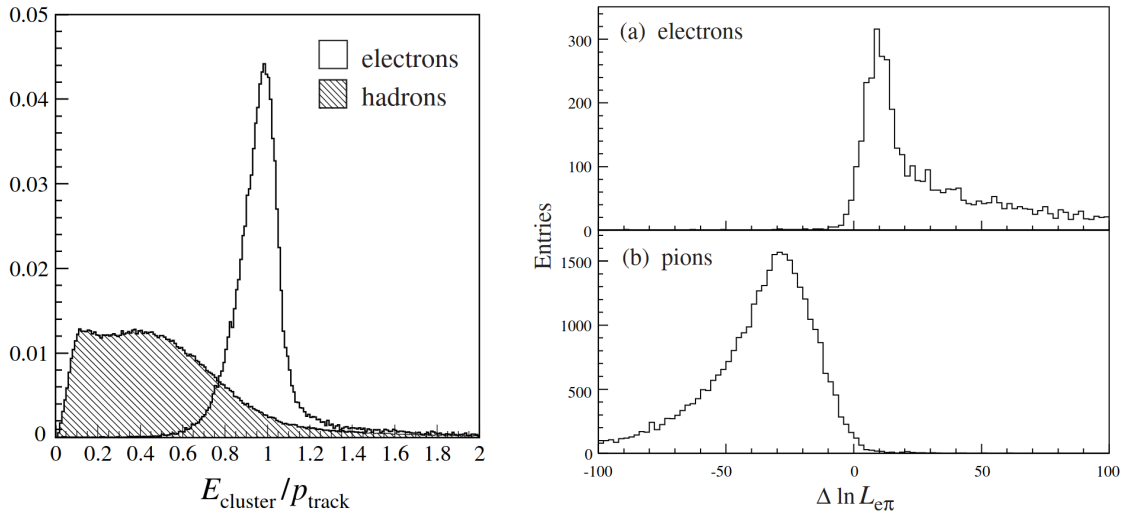

Figure **III-6**: (Left) Ratio of ECAL cluster energy and track momentum for electrons and hadrons. (Right) Difference in log-likelihood between electron and pion hypotheses for tracks with the calorimeter information for (top) electrons and (bottom) pions from simulated sample of $B^0 \to J/\psi(\to e^+e^-)K^0_S(\to \pi^+\pi^-)$ decays. Plots are taken from Ref. [46].

Bremsstrahlung recovery

Additional complexity in the electron reconstruction comes from bremsstrahlung radiation. It is emitted during an acceleration of a charged particle, and usually refers to acceleration in electric fields of surrounding charged particles and atom nuclei. All charged particles produce bremsstrahlung radiation, but electrons are especially prone to it, because of their low mass.

At LHCb, electrons can emit bremsstrahlung photons before or after the magnet; both cases are illustrated in Fig. **III-7**. If a photon is emitted before the magnet, it is registered in ECAL as a separate energy cluster, usually far from the electron cluster. At LHCb, most electrons emit one photon before the magnet. If a photon is emitted after the magnet, its energy deposit is either included within the electron cluster or it forms a cluster nearby.

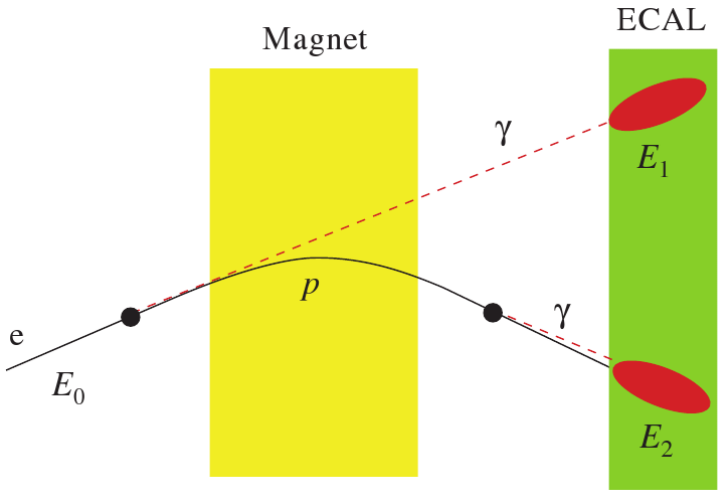

Figure **III-7**: Bremsstrahlung photons emitted by electron before and after the magnet. Energies of corresponding ECAL clusters are denoted as E_1 and E_2, respectively.

Bremsstrahlung photons can carry a substantial fraction of electron energy, so it is necessary to correct electron kinematics by including bremsstrahlung photons. In this brem-recovery procedure, the upstream track of each electron is extrapolated to ECAL, and photons (with transverse energy $E_T > 75$ MeV) measured around such an extrapolated region are added to the electron momentum and energy. Missing bremsstrahlung photons or wrongly recovered photons significantly lower the momentum and energy resolution for electrons.

III.2.9 Trigger system

In the LHC, proton bunches cross each other at the 40 MHz rate. At LHCb, the number of visible pp interactions in most of the bunch crossings is one or two. Most of the collisions do not result in production of particles interesting for the LHCb physics programme. To reduce the computing power required to process events before writing them to storage, the LHCb uses the trigger system to decide which events to save. The trigger system in Run-1 and Run-2 involved two stages: Low Level Trigger (L0) and High Level Trigger (HLT), which itself was split into two steps, HLT1 and HLT2.[7] A conceptual diagram of the LHCb trigger is presented in Fig. **III-8**.

[7] In Run-3, the LHCb trigger system changed significantly. In particular, there is no L0 and the trigger is fully software.

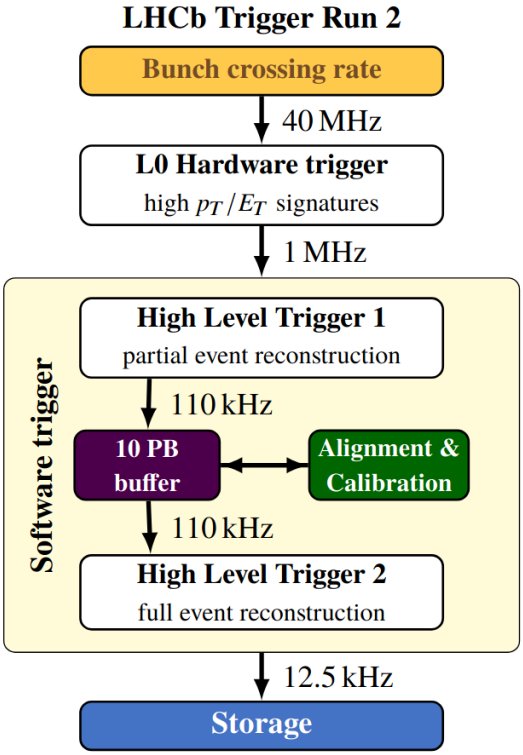

Figure **III-8**: Overview of the LHCb trigger system in Run-2 [54].

The L0 is a fully hardware-based system, which relies on thresholds on p_T or transverse energy[8] (E_T) of particles within given event [55]. The information required by L0 is provided by the calorimeter system and the muon detector. The calorimeter-based trigger selects high-E_T energy clusters, which are identified as electrons, photons or hadrons using the calorimeter system. The distinction between electrons and photons comes from SPD and PS. As PID information is limited at this stage, all hadron species are grouped together. The muon trigger selects high-p_T tracks based on (fast) track reconstruction and (rough) p_T estimation in Muon Stations.

The L0 trigger has a few independent channels: L0Hadron, L0Photon, L0Electron, L0Muon, which are single-particle channels, and L0DiMuon based on a muon pair. The single-particle channels accept events in which largest-E_T particle or largest-p_T particle is above the corresponding thresholds. For L0DiMuon, the threshold is set on the p_T product of the largest and second largest p_T muons. The exact threshold values are tuned, so the trigger performance varies between the data-taking years. For example, in 2017 the L0 thresholds were: $E_T > 3.46$ GeV in L0Hadron, $E_T > 2.47$ GeV in L0Photon, $E_T > 2.11$ GeV in L0Electron, $p_T > 1.35$ GeV in L0Muon and $p_T(1) \times p_T(2) > 1.69$ GeV^2 in L0DiMuon [55].

For events that have passed the L0 trigger, all the information from the LHCb subdetectors is collected and transferred to HLT, which is a software trigger based on applications run in a cluster of compute nodes. It contains two consecutive levels: HLT1 and HLT2. HLT1 lines are inclusive i.e. utilize only partial information from given event (e.g. one track or two tracks, and their momentum, IP, vertices) to minimize a required computing power. HLT2 operates on the full event information. HLT2 lines either perform a full reconstruction of given decays, or a partial

[8]Transverse energy is defined as $E_T = \sum_i E_i \sin\theta_i$, where E_i is energy deposit in calorimeter cell i, and θ_i is the angle between z axis and the line from i-th cell centre to PV.

reconstruction aimed at classes of similar decays. HLT2 does not have a capability to process all HLT1 data streams in real time. A 10 PB event buffer is deployed to allow for a continuous event processing during the beam downtime, such as the LHC beam injections. Events that have passed at least one line in each trigger step, L0, HLT1 and HLT2, are saved to a long term storage, and can be used in offline analyses.

III.2.10 Data flow and simulation

The data flow in LHCb, between collisions and offline analysis, is presented in Fig. **III-9**. Raw events accepted by the trigger system (Section **III.2.9**) are stored and undergo the full reconstruction. The reconstructed quantities describing a given event (tracks, charges, PID, momenta, energies) are saved into output (FULLSTREAM) in files called DSTs.

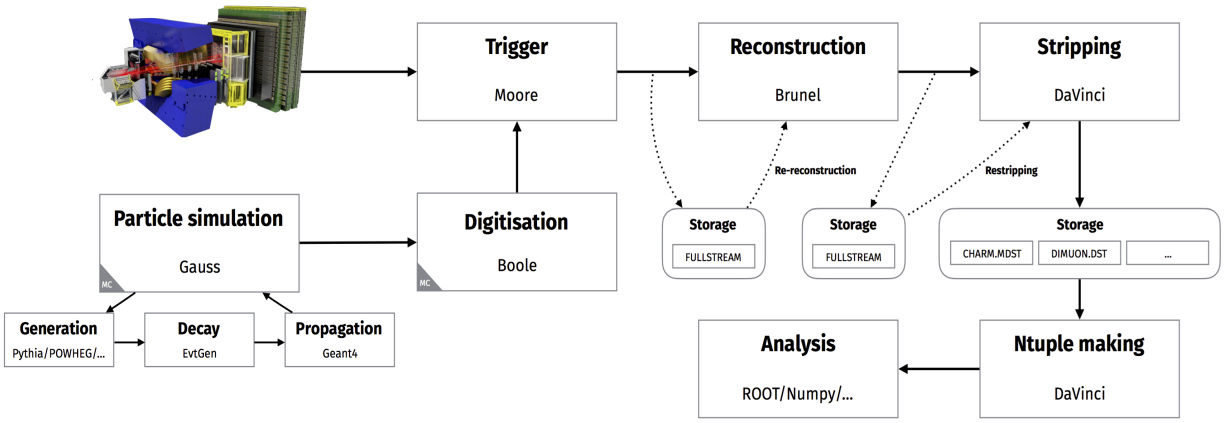

Figure **III-9**: Data flow in LHCb. The application used at each step of the process is also specified.

Even after the trigger filtering, the amount of data recorded remains too large to access and analyse. Therefore, an offline preselection, called *stripping*, is ran centrally for each analysis. A preselection algorithm, a stripping line, builds candidates for decays of interest, and performs their initial selection based on kinematic and topological properties expected for these decays. Stripping lines for similar processes are grouped into streams; lines for charm decays are saved within the CHARM stream. Based on the striping output, analysts can produce data files (n-tuples) using the DaVinci application. The n-tuples are relatively easy to perform offline analysis. The stripping lines used in the presented analysis are described in Section **V.3.1**.

A distinct part of the diagram in Fig. **III-9** corresponds to simulations. This is because, besides the measured experimental data, a typical analysis benefits from simulated data, usually produced with Monte Carlo (MC) methods. Such simulations are essential for modelling a response of the detector to measured observables (resolution, efficiency, acceptance), which then allows to disentangle physics quantities of interest. Another typical use case is modelling a simulation-based prediction for a given physical process or quantity, and comparing it to that measured in experimental data.

Production of MC simulation in the LHCb experiment is split into several steps: particle generation, decay, and propagation (Fig. **III-9**). The generation step corresponds to modelling of the pp collisions at the nominal LHC energy. It includes, in particular, kinematic distributions of produced particles, which are randomly sampled. The particle decay step incorporates known kinematic distributions of given decay. For a new (unobserved) decay channel, predictions

according to different models are implemented. Finally, the particle propagation step calculates trajectories of particles and their interactions with the detector material. The interaction model includes but is not limited to: elastic and non-elastic scatterings, magnetic field acceleration and bremsstrahlung. This step requires a detailed detector model with the element content of each subdetector, as well as the magnetic-field map. It is the most computationally demanding step, as each particle is propagated through the detector individually. The energy deposited in each subdetector is then summed across all particles. It is passed further to a digitisation program, in which the actual detector response is modelled. This step relies heavily on the readout calibration, with the primary objective being to ensure that the simulated event closely resembles the actual event. The resulting simulation data are then processed by the trigger, reconstruction and stripping selection in the same way as real data.

In LHCb, *pp* collisions are generated using Pythia8 [56], [57] with a specific LHCb configuration, Gauss [58]. Particle decays are described using models implemented in EvtGen [59], with final-state radiation generated using Photos [60]. Interactions of particles with the detector material, and the detector response, are implemented using the Geant4 toolkit [61].

Chapter IV

Magnet Stations

IV.1 Motivation

The LHCb collaboration continuously works on improving the current experiment and designing future upgrades that would extend the detector performance. Magnet Stations (MS) is a proposed subdetector (Fig. **IV-1**) that will improve the reconstruction of low-momentum particles (with $p < 5$ GeV). It is a part of the LHCb Upgrade II [17]. The MS prototype tests are planned for 2025.

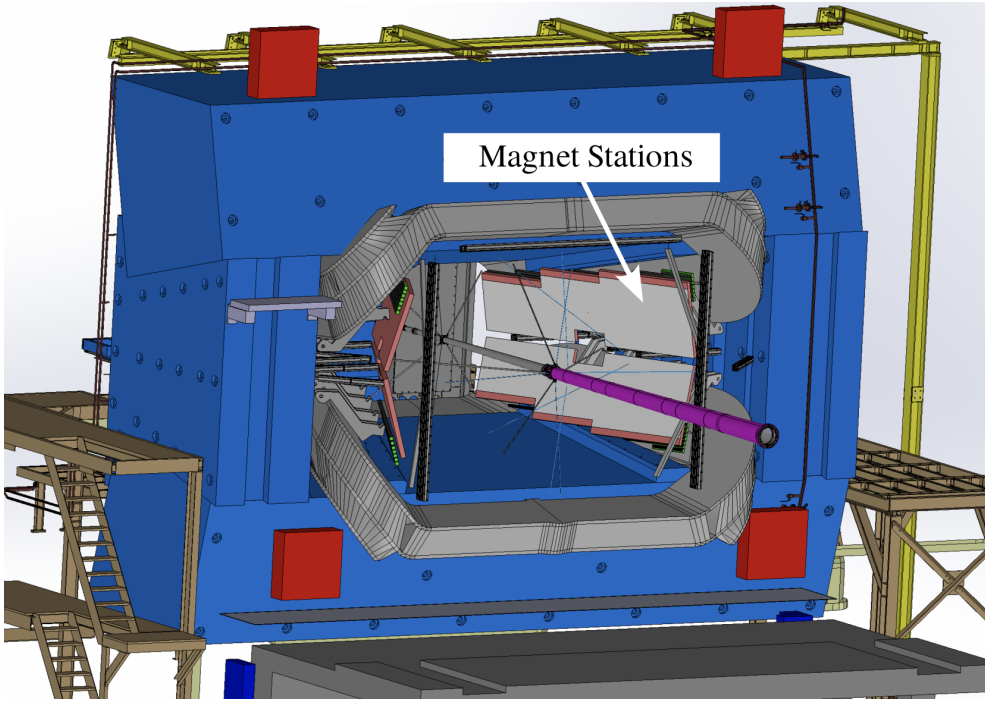

Figure **IV-1**: Layout of Magnet Stations and their surrounding parts at the LHCb detector after Upgrade II [62].

Typically, subdetectors of the LHCb detector are positioned perpendicular to the beam axis, whereas sensitive planes of MS are placed in a more parallel orientation inside the magnet. Figure **IV-2** presents the placement of MS within the LHCb tracking system, and expected increase of its acceptance.

The MS role is to detect charged particles that, due to the magnetic field, are bent outside

the detector acceptance. Before the magnet, such particles are tracked by VELO and Upstream Tracker (UT). Some of the magnetic field reaches UT, allowing for momentum measurement with the relative resolution of $\sigma(p)/p = 12.3\%$ [63]. With MS installed, the momentum resolution of those particles is expected to improve to about 1%.

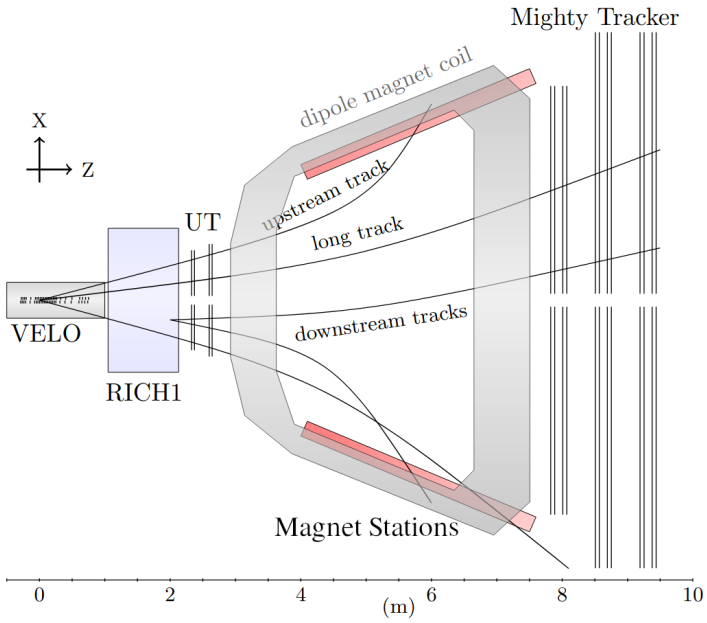

Figure **IV-2**: Different types of tracks reconstructed within the LHCb detector after Upgrade II [17]. Long tracks traverse the entire spectrometer giving hits in VELO, UT and Mighty Tracker. Downstream tracks have hits in UT and Mighty Tracker alone. Upstream tracks are low-momentum particles that are deflected into the magnet coils and give hits in VELO, UT and MS.

An improved tracking of low-momentum particles can improve the sensitivity of numerous analyses within the LHCb physics programme, and enable new studies. For example, by introducing the MS subdetector, measurements involving $D^{*+} \to D^0\pi^+$ decays will have significantly better elimination of ghost tracks for *soft* pions from D^{*+} decays, as well as improved resolution of the invariant-mass difference, $m(D^{*+}) - m(D^0)$. Figure **IV-3** presents three distinct scenarios of the π^+ tracking and expected improvements. Other processes that will also experience a significant increase in the tracking efficiency, are in particular all the channels that contain electrons, soft pions or soft kaons in final states. Some key examples are given in Table **IV-1**. Consequently, measurements involving these processes will have improved sensitivities, which is crucial in particular for studies limited by statistical uncertainties.

IV.2 Geometry

As of the time of writing, the MS detector is still under active development. The current version consists of four modules located inside the LHCb magnet. Figure **IV-1** shows the upper-left and lower-left modules, as well as the magnet yoke and coils. In the middle, one can spot the beam pipe, which is almost parallel to the MS modules. The design aims to achieve symmetry between the sensitive parts of the stations. The upper and lower stations are symmetric relative to the x-z plane, while the left and right stations are symmetric relative to the y-z plane in the LHCb

Decay channel	Efficiency increase
$\rho^0 \to \pi^+\pi^-$	1.5
$K_S^0 \to \pi^+\pi^-$	1.9
$K^{*0} \to K^+\pi^-$	1.5
$D^{*+} \to D^0\pi^+$ [π^+ in MS]	2.0
$D^{*0} \to D^0\gamma(\to e^+e^-)$ [e^+e^- in MS]	3.0
$B^+ \to \bar{D}^0(\to (K_S^0(\to \pi^+\pi^-)\pi^+\pi^-)K^+$	1.7
$\Omega_c^{*0}(3067) \to \Xi_c^+(\to pK^-\pi^+)K^+$	1.3

Table **IV-1**: Expected increase of the tracking efficiency due to the MS subdetector [63].

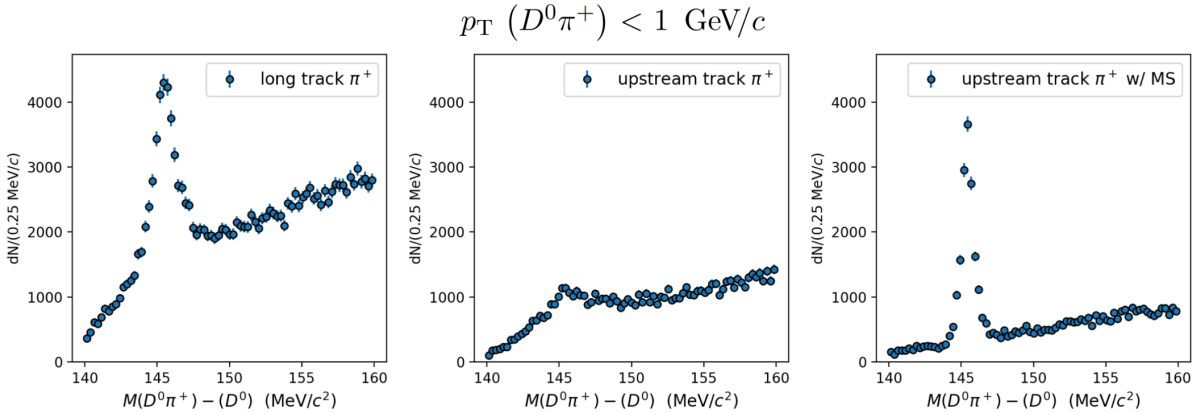

Figure **IV-3**: Distribution of invariant-mass difference, $m(D^{*+}) - m(D^0)$, for $D^{*+} \to D^0(\to K^-\pi^+)\pi^+$ decays with soft π^+ track reconstructed as (left) long track, (middle) upstream track and (right) upstream track measured with MS. Distributions are for D^{*+} decays obtained using the full detector simulation. D^0 candidates are selected to have $m(D^0)$ within 20 MeV of the nominal D^0 mass; no PID is required for the soft π^+ track. The MS condition is emulated by smearing the true pion momentum assuming $\sigma(p)/p = 1\%$. Figure taken from Ref. [63].

coordinate system.

As shown in Fig. **IV-4**, each module is built of four parallel planes, spaced by a few centimetres, whereas each plane consists of scintillating bars. The dimensions of the bars are 5 mm along the z-axis, and between 30 mm and 300 mm along the y-axis, depending on their distance from the x-z plane. This non-uniformity reflects changes in the occupancy along the y-axis.

Optic fibres are used to transmit light from the bars to outside of the magnet, where it can be collected. The light is registered by photo-multipliers and converted to digital signals in the dedicated analog-to-digital converter (ADC) boards. The digital signals are processed by field-programmable gate array (FPGA) boards, which perform a basic hit processing before passing signals to the readout system.

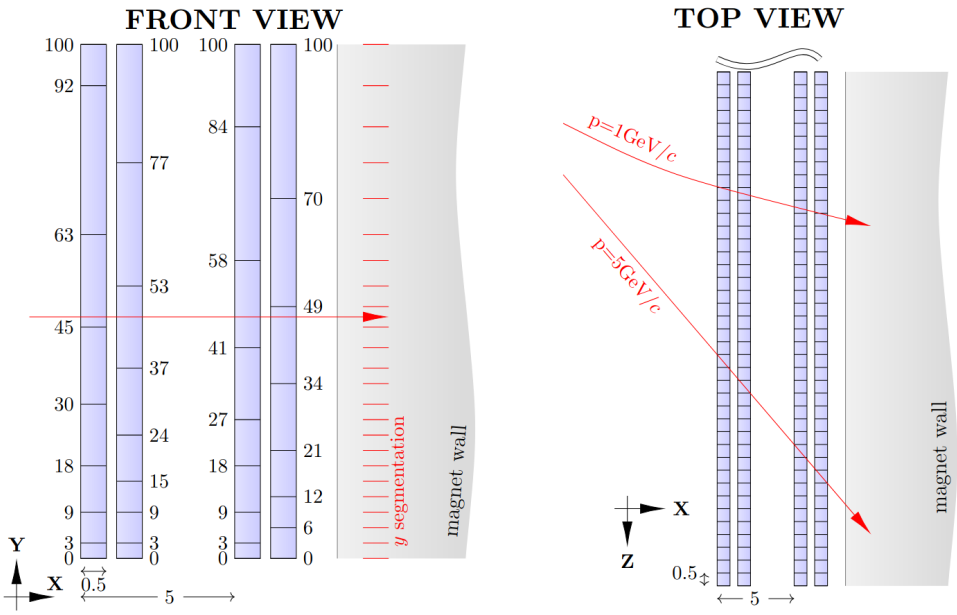

Figure **IV-4**: The segmentation of scintillators in a module of the MS subdetector [63].

IV.3 Simulation

Throughout the development process, the MS geometry underwent several modifications to address technical constraints, whilst maintaining the physics performance. Simulations have been used to select the optimal geometry.

The detector description includes the geometry, materials, alignment constants and readout segmentation. The detector description for MS is prepared in the DD4hep framework [64]. DD4hep is a relatively new description standard chosen for all the future LHCb subdetectors. It is integrated with the GEANT4 application [61] for simulating the passage of particles through the detector material. The description includes two components: XML with definitions of all variables and basic geometry, and C++ code that translates the XML files into more complex, simulation ready, structures.

At the early stage of the detector development, the MS panels were rectangular, but the need for maximising the available space inside the magnet, pushed the design into a more fitted shape. Figure **IV-5** presents the results of the simulation for both designs. With the positive results of the corresponding analysis performed on the simulated data, the change in the panel shape has been accepted by the MS working group.

IV.4 Shape optimisation and expected performance

The shape of the scintillating bars has been also optimised. Originally, they were intended to have a triangular cross-section. However, this required an extensive number of optical fibres, which presented significant technical difficulties. The simulation has been performed, to determine if moving to a diamond shape (rhombus), and thus reducing the number of channels by half, would not result in a significant resolution deterioration.

The GEANT4 simulation calculates energy deposition in volumes crossed by each particle. The more details defined in the detector description, the more complex the simulation becomes.

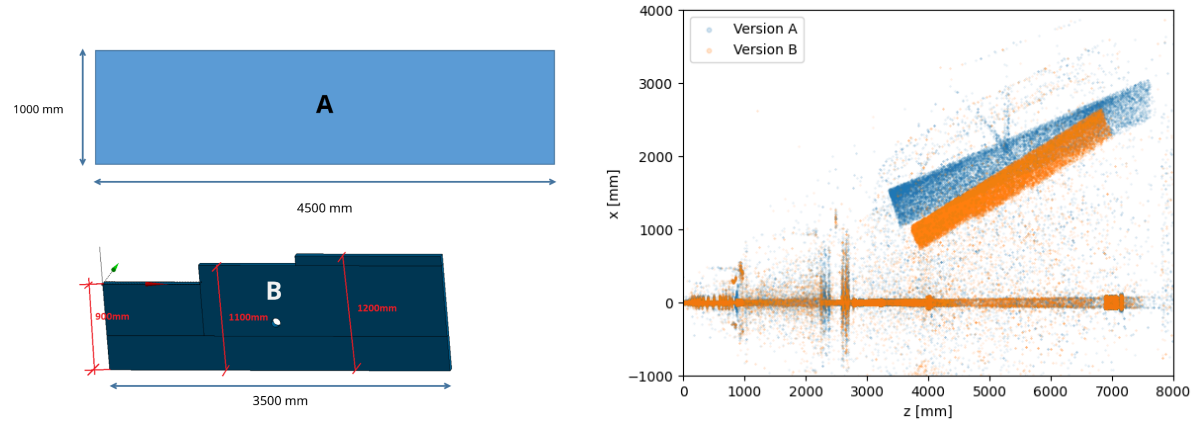

Figure **IV-5**: (Left) Two versions of the MS panel shapes: A - rectangular and B - fitted to the available space. (Right) Simulated origin vertices for all particles that have hits inside MS, for both versions of the MS panel shapes. Vertices across the bottom of the plot are from particles produced within the beam pipe, VELO and UT.

With the reduction in the number of channels, there are still nearly 80000 channels planned. Instead of adding all of them to the detector description, the GEANT4 simulation is based on just a few rectangular volumes per panel. A similar approach, in which a proper segmentation and digitisation is done after the initial simulation, is also used for other LHCb subdetectors. The transition to the DD4hep description in the LHCb experiment was done at the same time as the described MS development, and because of that, central tools for the segmentation and digitisation were not ready to use at the time. To proceed with the segmentation testing, a simplified deposition model has been implemented.

The model assumes a uniform energy distribution inside the scintillating material, along an approximated particle trajectory. A relatively thin panel, in comparison to the typical curvature corresponding to the targeted momentum range, enables a trajectory to be simplified to the straight line - from the point of entry into the sensitive volume, to the point of exit or decay vertex. The particles created in the interactions with the detector material have been also included in the total energy deposition distribution.

The MS detector is uniquely positioned. It is subject to a high magnetic field, and particles cross it at various angles. Light particles with low momentum are highly bent, and can start going upstream (having the velocity with a negative z-component) inside the magnet. On the other hand, some high-p_T particles moving between the magnet and the outermost MS panel can hit MS from the back. In general, the design goal has been to reconstruct tracks in the widest possible range of crossing angles.

The track reconstruction requires a position measurement from each MS panel crossed by a particle. As particles can cross at various angles, they typically deposit energy in more than one bar, creating a cluster. The ADC boards digitise the deposited energy into four discrete levels. The cluster position is then calculated by weighting the bars' positions according to their corresponding energy levels, and finding the weighted average. This is why the optimal cell shape is crucial for the precise measurement of the cluster position. A diagram of the track that creates a three-bar cluster, in the rhombus bar configuration, is presented in Fig. **IV-6**. To find an optimal scintillating bar shape, a range of the angles α between two adjacent walls has been tested.

In this analysis, the reconstructed cluster position is compared to its true simulated value.

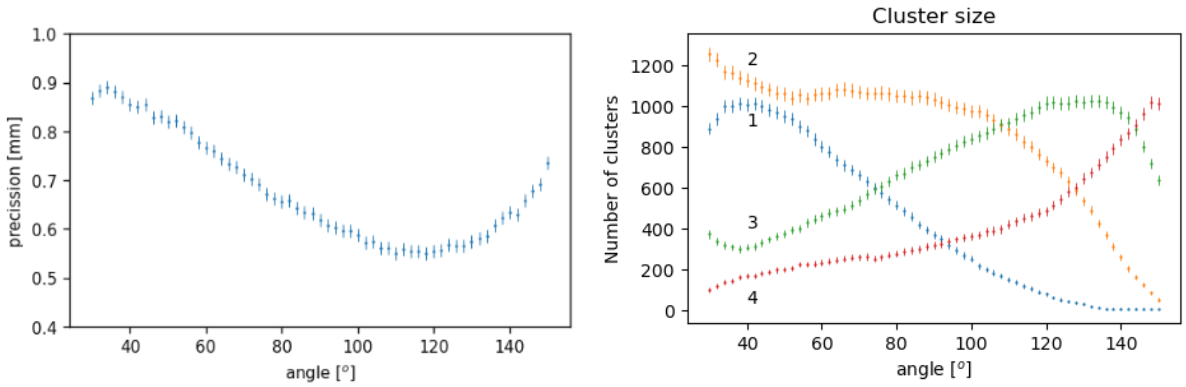

Figure **IV-7**: (Left) Uncertainty of the average cluster position measured as a a function of the cell angle α using simulated data. (Right) Number of clusters of a given size (1, 2, 3 or 4) measured as a function of the cell angle α using simulated data.

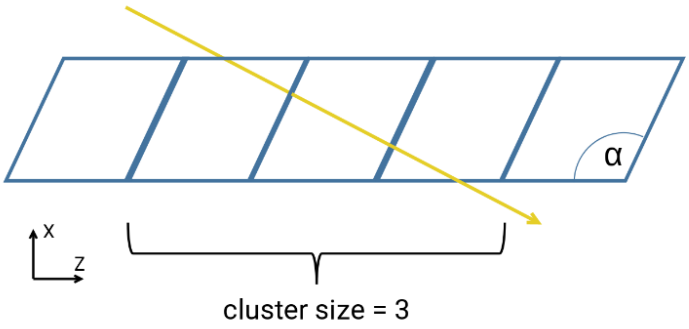

Figure **IV-6**: MS segmentation in the z-direction, with an example of a particle track and corresponding energy deposition clustering.

The particles selected are required to have their origin vertex near PV, and the energy higher than the minimal threshold. Each analysed angle α has its specific deposited energy distribution, so the energy levels for the quantisation are selected based on the 10%, 40% and 70% quantiles. The analysis results are presented in Fig. **IV-7**. The optimal angle is found to be $\alpha = 120°$. At this angle, most of the targeted clusters are composed of three bars.

IV.4.1 Occupancy

The MS readout involves three stages: ADC boards, FPGA clustering boards and FPGA tracking boards. The tracking boards are responsible for processing the information from the whole station and sending it to the central LHCb readout system. The clustering boards collect the signals from the individual bars, perform zero suppression and clustering. The number of channels is too high for a single clustering board per panel, mainly due to the limited connectivity and processing power of a single board. The optimal number and type of boards are selected based on the MS occupancy. To estimate that, the simulation with the Run-3 luminosity is performed. The results, presented in Fig. **IV-8**, have been passed to the MS working group for further analysis.

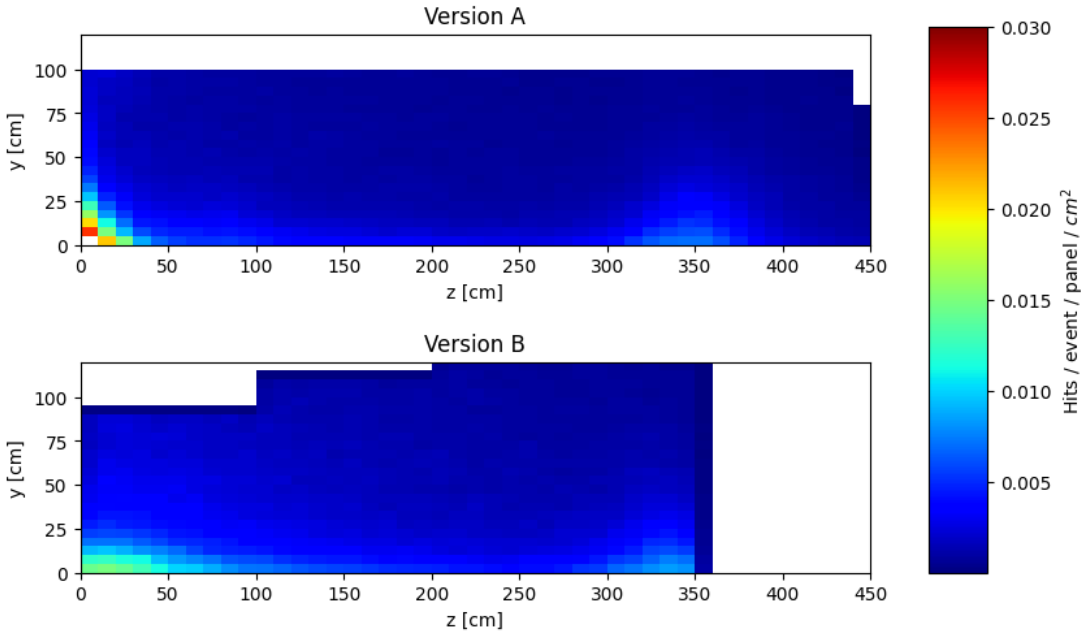

Figure **IV-8**: Simulated hit rates in one of the upper MS panels for two panel shapes: (top) A and (bottom) B (see Fig. **IV-5**). The minimal deposited energy $E > 0.15\,\text{MeV}$ is required.

In Fig. **IV-8**, the occupancy at the lower edges of panels is higher, due to the magnetic field impact on particles with low p_T. The geometry in the version B, has a slightly wider gap between the upper and lower stations than in the version A. It was necessary to introduce this gap in order to fit the support structure for the MS into the tight space inside the magnet. The occupancy increase (hot-spot) at around $z = 350$ cm comes from the beam-pipe support structure. The beam pipe is the main source of background in the MS subdetector.

Chapter V

Search for $\Lambda_c^+ \to pe^\pm\mu^\mp$ decays

V.1 Analysis strategy

The presented analysis comprises a search for $\Lambda_c^+ \to pe^\pm\mu^\mp$ decays, which are forbidden within the SM. In terms of numerical results, the goal is to measure (or set UL on) BF for the signal channels, $\Lambda_c^+ \to pe^+\mu^-$ and $\Lambda_c^+ \to pe^-\mu^+$, with respect to the known BF for the reference decay, $\Lambda_c^+ \to p\phi$, followed by $\phi \to \mu^+\mu^-$. The topology of the reference channel is similar to that of the signal decays, which assures cancellation of many systematic uncertainties in the BF ratio to be measured. For the signal decays, the two charge combinations are measured separately, as, in principle, they could be affected by different BSM effects. Previously, $\Lambda_c^+ \to pe^\pm\mu^\mp$ decays were searched for by the BaBar experiment [29]. The presented analysis is based on the LHCb data collected during the Run-2 data taking, between 2016 and 2018. This large data sample, corresponding to the integrated luminosity of 5.4 fb^{-1}, is expected to provide significantly better sensitivity compared to the ULs set by BaBar.

A diagram presenting the analysis flow is shown in Fig. **V-1**. The analysis uses MC simulations of the signal decays, the reference channel, as well as decays being the main source of misidentified background, $\Lambda_c^+ \to p\pi^+\pi^-$. Simulation samples are calibrated to reliably describe the data. Both, data and simulation samples undergo the selection procedure, which includes stripping, trigger, preselection and two-step selection involving Boosted Decision Trees (BDTs). Candidates for the signal and reference decays are constructed at the stripping level. Signal decays are identified with the reconstructed mass of Λ_c^+ candidates, $m(\Lambda_c^+)$, measured as the invariant mass of the $pe^\pm\mu^\mp$ final states. Similarly, the reference decays are identified using the invariant mass of the $p\phi$ final state.

The selection is meant to increase the signal efficiency, and to suppress misidentified and combinatorial backgrounds. It is based on kinematic and topological observables for Λ_c^+ and final-state particles, as well as PID classifiers for final-state proton, muon and electron. In addition, isolation variables, which describe signal properties with relation to the underlying event, are exploited in the second BDT classifier. The final selection is three-dimensional, performed in the space formed with electron PID, muon PID and output of the second BDT classifier. The selection requirements are optimized to provide the best (lowest) UL on BF of the signal decays. This approach is based on the assumption that the signal decays will not be observed. Due to different $m(\Lambda_c^+)$ shapes of the signal and misidentified background, the signal decays with and without reconstructed bremsstrahlung photons are considered separately in the final optimization.

In the presented analysis, MC simulations are used to calculate efficiencies of the reconstruc-

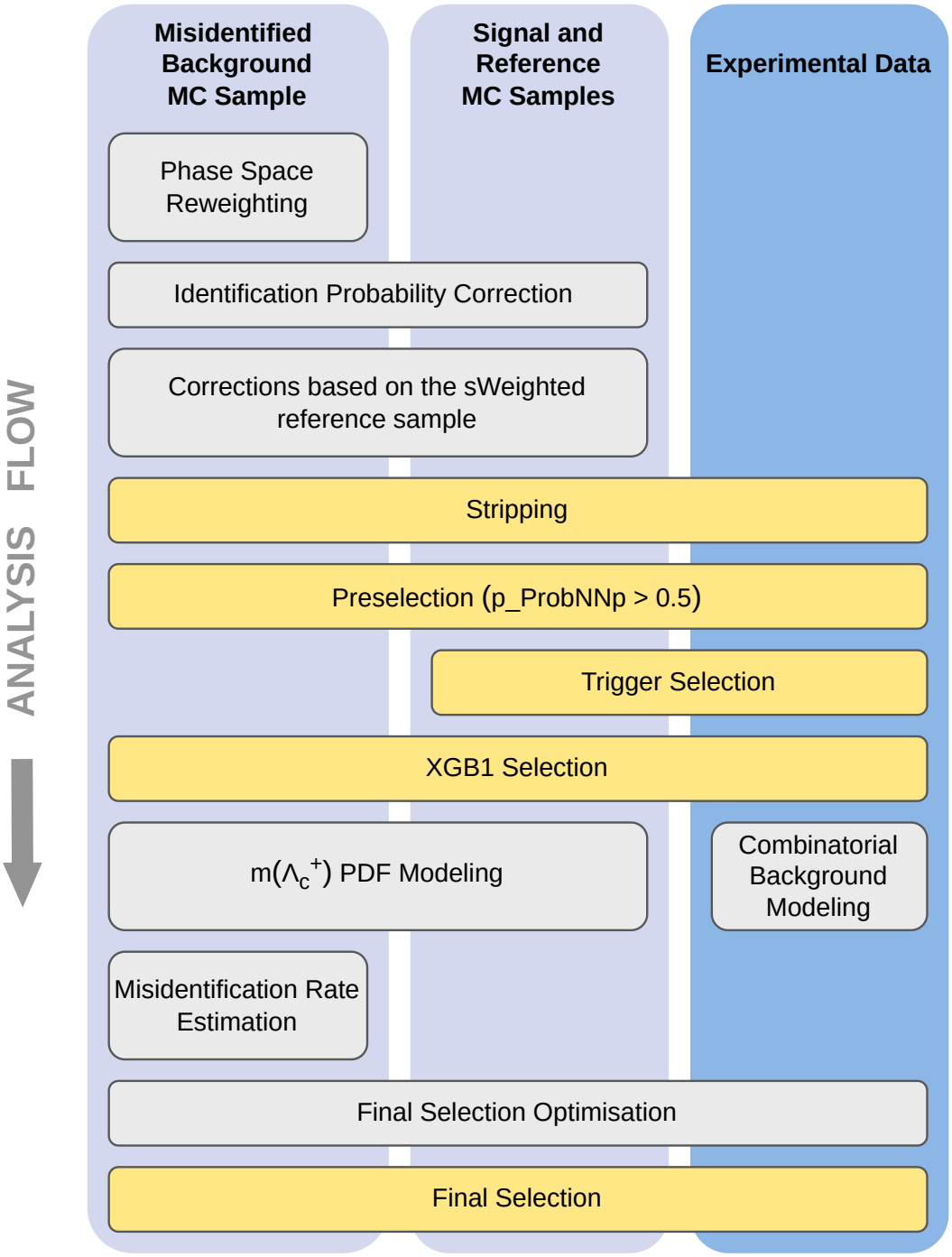

Figure **V-1**: Diagram presenting the analysis flow.

tion/selection for the signal and reference decays, to estimate expected number of background events from $\Lambda_c^+ \to p\pi^+\pi^-$ due to $\pi^+\pi^-$ being misidentified as $e^+\mu^-$, and to model $m(\Lambda_c^+)$ shapes for the signal and reference decays, as well as for the misidentified background. PID responses,

usually poorly modelled in simulations, are calibrated to better match those in the data. Some event and signal properties in MC samples (Λ_c^+ kinematics, track multiplicity) are also calibrated using the $\Lambda_c^+ \to p\phi$ sample obtained before the final selection. In addition, the phase-space (Dalitz) distribution of $\Lambda_c^+ \to p\pi^+\pi^-$ decays is reweighted to account for contributions from intermediate resonances.

The number of the signal decays for each of the two channels, $\Lambda_c^+ \to pe^+\mu^-$ and $\Lambda_c^+ \to pe^-\mu^+$, is measured with unbinned maximum-likelihood fits performed to the $m(\Lambda_c^+)$ distributions. In these fits, probability distribution functions (PDFs) for the signal and misidentified background are based on the corresponding simulations, while the combinatorial background is modelled using data for candidates formed with non-physical particle combinations, in particular with same-sign leptons. For each signal channel, Λ_c^+ candidates with and without bremsstrahlung photons are fitted simultaneously with independent signal and background shapes, and shared signal yield and misidentified background yield.

The analysis is performed as *blind*, meaning that Λ_c^+ candidates having reconstructed masses close to the known Λ_c^+ mass are removed till the final selection has been optimized and all the analysis steps scrutinized. These Λ_c^+ candidates have been unblinded only for the final fits. This procedure ensures that the measurement is unbiased.

Following sections of this Chapter present all the analysis steps. The data and simulation samples used in the analysis are described in Section **V.2**. Section **V.3** presents the signal selection applied prior to the final selection, which itself is discussed in Section **V.5**. Categories of the signal decays and their MC-based shapes are presented in Section **V.4**. The reference-channel selection, and preselected $\Lambda_c^+ \to p\phi$ sample used for the MC calibration, are presented in Section **V.6**. The calibration of MC samples is presented in Section **V.7**. MC-based studies of the misidentified background are discussed in Section **V.8**. Calibration of signal MC samples is presented in Section **V.7**. Modelling of $m(\Lambda_c^+)$ shapes for all the signal and background components is presented in Section **V.9**. The details of the BFs to be measured, and the method used for the UL estimation are presented in Section **V.10**, while the estimation of the efficiencies in Section **V.11**. The optimisation of the final selection is presented in Section **V.12**, whereas the systematic uncertainties are discussed in Section **V.13**.

V.2 Data and simulation samples

The presented analysis is based on the experimental data from the pp collisions at the centre-of-mass energy of $\sqrt{s} = 13$ TeV, collected by the LHCb experiment in 2016, 2017 and 2018 during Run-2 of the LHC. The integrated luminosities in these data-taking years are 1.6 fb^{-1}, 1.7 fb^{-1} and 2.1 fb^{-1}, adding up to 5.4 fb^{-1}. In these data, $\Lambda_c^+ \to pe^\pm\mu^\mp$ candidates for signal decays, as well as $\Lambda_c^+ \to p\phi$ candidates, with $\phi \to \mu^+\mu^-$, for the reference (normalisation) channel are constructed at the stripping level (Section **V.3.1**). In addition, non-physical candidates containing same-charge leptons, are also constructed, giving "Λ_c" $\to pe^\pm\mu^\pm$ candidates. Their wrong-charge combinations assure a purely combinatorial nature rather than any physics origin. Therefore, these data samples are used to model the combinatorial background in reconstructed samples of the signal candidates (Section **V.9.4**).

The analysis is supported by MC simulations of the signal channels, the reference channel, as well as $\Lambda_c^+ \to p\pi^+\pi^-$ decays being the main source of misidentified background. Each of these samples is separately produced for each data-taking year, with various parameters (related to trig-

ger, reconstruction, calibration) tuned to match those specific for a given year. The samples from different data-taking years are weighted according to the corresponding integrated luminosities. This assures that each data-taking period is properly represented in the MC-based analysis steps (BDT training, efficiency calculation, obtaining signal shapes). The samples are also simulated separately for the two magnet polarity configurations, designated as: *MagUp* when the magnetic field is pointing upwards, and *MagDown* in the opposite scenario. In a typical data taking year, the polarity of the magnetic field is periodically reversed in order to control possible left-right asymmetries of the detector, and to assure cancellation of related systematic uncertainties.

Both signal decays, $\Lambda_c^+ \to pe^-\mu^+$ and $\Lambda_c^+ \to pe^+\mu^-$, have their dynamics described with a phase-space model, meaning that they proceed without any intermediate resonances. This is chosen in order to perform the analysis in the model-independent way, i.e. without assuming any specific BSM contribution. In the reference decay, $\Lambda_c^+ \to p\phi$ is described with a phase-space model, whereas $\phi \to \mu^+\mu^-$ with a model meant for a decay of a vector meson into two leptons (`VLL` model in EvtGen [59]). For $\Lambda_c^+ \to p\pi^+\pi^-$decays, a phase-space model is chosen ignoring any resonance contributions. However, the $\Lambda_c^+ \to p\pi^+\pi^-$ phase-space distribution is reweighted to describe resonance structures observed in data (Section **V.7.3**).

All the simulation samples contain the standard mixture of the prompt Λ_c^+ production and the secondary Λ_c^+ production from decays of beauty hadrons (Section **III.2.1**). Their relative contributions are determined by the charm and beauty production cross-sections implemented in the Pythia8 generator [57]. Including both production mechanisms is necessary to reliably describe the data properties, although the selection is designed to favour the prompt production and to suppress the secondary contribution. In particular, the BDT-based selection (Section **V.5**) is optimized for promptly-produced signal, with secondary signal removed using the `TruthMatching` method[9].

In order to avoid performing the full detector simulation for candidates which do not satisfy the selection requirements, loose kinematic and topological requirements are applied at the generator level. These requirements are significantly looser than those applied in the selection, to account for the fact that resolution effects are unknown prior to the full simulation. The efficiency of these generator-level cuts is considered in the BF calculation (Section **V.11**).

The simulation events undergo the standard LHCb processing, which includes reconstruction, trigger and stripping, in the same way as the experimental data. The $\Lambda_c^+ \to pe^\pm\mu^\mp$ simulations undergo the signal selection, whereas the $\Lambda_c^+ \to p\phi$ simulation undergoes the reference selection. The $\Lambda_c^+ \to p\pi^+\pi^-$simulation sample is reconstructed as either the signal decays or the reference decay, in order to study misidentified background contributing into these channels.

V.3 Selection of signal decays

An environment of the pp collider is busy, meaning that the multiplicity of particles produced in the pp collisions is high. As a result, the number of reconstructed tracks per event is also high, leading to a significant combinatorial background in the studied decays. Another background, which significantly contaminates reconstructed samples of the $\Lambda_c^+ \to pe^\pm\mu^\mp$ signal candidates is from $\Lambda_c^+ \to p\pi^+\pi^-$ hadronic decays due to $\pi^\pm \to e^\pm$ and $\pi^\pm \to \mu^\pm$ misidentification.

Both these backgrounds have to be filtered out through the selection procedure. This is the

[9]It is the MC tool which allows to associate particles reconstructed in simulations with generated particles and their mother particles.

main challenge of the presented analysis, as the presence of the backgrounds heavily impacts the measurement sensitivity. The selection contains multiple steps: stripping selection, (hardware and software) trigger selection, preselection, and two-step selection involving multivariate analysis (MVA) based on BDTs.

V.3.1 Stripping and preselection

The stripping step is a crucial part of the signal reconstruction, in which candidates for $\Lambda_c^+ \to pe^\pm\mu^\mp$ signal decays, and their charge conjugates, are constructed. The candidates are built by combining two oppositely-charged leptons (electron and muon) with a proton. The stripping line used for the signal channel, `StrippingLc23MuLc2pemuLine`, contains requirements on PID, kinematics and track quality of the daughter particles, as well as on kinematics, topology and reconstructed mass of the Λ_c^+ candidates. The stripping selection is summarized in Table **V-1**.

The PID selection on daughter tracks is performed in terms of $\mathrm{DLL}_{p1,p2}$ quantities comparing between two particle hypotheses (Section **III.2.8**). The requirement on the ghost probability (P_{ghost}) removes false (ghost) tracks reconstructed from unrelated hits in the tracking system. An important topological quantity, IP significance (χ^2_{IP}) is defined as the difference between the vertex-fit χ^2 of a PV reconstructed with and without the considered particle. Here, χ^2_{IP} is calculated with respect to the best PV (BPV),[10] defined as a PV with respect to which a given particle has the smallest IP. The χ^2_{IP} cut on the daughter particles removes those originating from BPV, and along with the p_T requirement, helps to suppress combinatorial background. The χ^2_{IP} cut applied for Λ_c^+ candidates suppresses the secondary contribution. The flight distance (FD) of a Λ_c^+ candidate is measured as the distance between BPV and the Λ_c^+ decay vertex. The requirement on the reconstructed Λ_c^+ mass is with respect to the known Λ_c^+ mass, $M_{\Lambda_c} = 2286.5$ MeV [19]. Overall, the stripping selection is loose, to allow for optimising requirements at the later analysis stages.

The basic preselection is applied for the Λ_c^+ candidates that have passed the stripping selection. It restricts the proton PID as: `p_ProbNNp` > 0.5 (Section **III.2.8**), in order to suppress combinatorial background, without significantly affecting the signal. This preselection assures the signal efficiency of about 91%, while keeping only around 57% of the background candidates. More detailed discussion of the efficiencies at the individual analysis steps is given in Section **V.11**.

V.3.2 Trigger selection

The trigger selection is based on the signal-preserving lines, meaning high efficiency without distorting signal properties. The lines chosen at each trigger level are:

```
Lc_L0MuonDecision_TOS==1,                                              (V.1)
```

```
Lc_Hlt1TrackMVADecision_TOS==1 OR Lc_Hlt1TwoTrackMVADecision_TOS==1,   (V.2)
```

and additionally, for the $\Lambda_c^+ \to pe^+\mu^-$decay:

```
Lc_Hlt2RareCharmD2KEMuOSDecision_TOS==1 OR Lc_Hlt2RareCharmD2PiEMuOSDecision_TOS==1,
                                                                       (V.3)
```

[10] Alternatively, BPV is denoted as OWNPV, or called associated PV.

Observable	Cut	Description of observable
	Daughter tracks	
p_T	> 300 MeV	Transverse momentum
χ^2_{track}	< 4	Track quality
P_{ghost}	< 0.4	Probability that track is a ghost
χ^2_{IP}	> 9	IP significance with respect to BPV
e: DLL$e\pi$	> 2	Electron PID relative to π hypothesis
p: DLL$p\pi$	> 5	Proton PID relative to π hypothesis
p: DLLpK	> 0	Proton PID relative to K hypothesis
μ: DLL$\mu\pi$	> -5	Muon PID relative to π hypothesis
μ: DLLμK	> -5	Muon PID relative to K hypothesis
	Two-track combination	
DOCA(p,e)	< 0.3 mm	Distance of closest approach
DOCA(p,μ)	< 0.3 mm	Distance of closest approach
DOCA(μ,e)	< 0.3 mm	Distance of closest approach
	$\Lambda_c^+ \to pe^\pm\mu^\mp$	
χ^2_{VTX}	< 15	Vertex quality
χ^2_{IP}	< 100	IP significance with respect to BPV
FD(Λ_c^+)	> 70 μm	Flight distance of Λ_c^+
$\lvert m(\Lambda_c^+) - M_{\Lambda_c}\rvert$	< 350 MeV	Reconstructed mass relative to the known Λ_c^+ mass

Table **V-1**: Stripping selection in `StrippingLc23MuLc2pemuLine` used for $\Lambda_c^+ \to pe^\pm\mu^\mp$ signal channels.

and for the $\Lambda_c^+ \to pe^-\mu^+$decay:

```
Lc_Hlt2RareCharmD2KMuEOSDecision_TOS==1 OR Lc_Hlt2RareCharmD2PiMuEOSDecision_TOS==1,
```
(**V.4**)

where `TOS` stands for Trigger On Signal[11], and means that given trigger line has been fired by a specified particle or its daughters. Here, the selected L0 and Hlt1 lines are required to be fired by any daughter particles of a Λ_c^+ candidate, whereas the Hlt2 lines by a Λ_c^+ candidate itself. The Hlt1 selection is applied to the Λ_c^+ candidates that have fulfilled the L0 selection, and the Hlt2 selection to the candidates that have passed both, the L0 and Hlt1 requirements.

The `L0Muon` trigger is based on information from Muon Stations (Section **III.2.9**). The Hlt1 lines are based on BDT classifiers using properties of a single track (in `Hlt1TrackMVA`) or two tracks (in `Hlt1TwoTrackMVA`) forming Λ_c^+ candidates. The observables used in these BDT clas-

[11] As opposed to `TIS` (Trigger Independent of Signal), which is fired by any particle from an underlying event, except for a specified one.

sifiers are presented in Tables **V-2** and **V-3**. Direction angle ($DIRA$) in Table **V-3** is defined as the angle between the momentum vector of two-track combination and the direction vector between two-track vertex and BPV. The corrected mass (m_{corr}) for two-track (t_1t_2) combination in Table **V-3** is defined as $m_{corr} = \sqrt{m^2(t_1t_2) + p'^2_T(t_1t_2)} + p'_T(t_1t_2)$, where the invariant mass of t_1t_2 pair is *corrected* for its momentum transverse with respect to its flight direction [65].

As the names of the Hlt2 lines in Eqs. **V.3** and **V.4** suggest, these lines are in principle dedicated for decays of charm D^+ mesons to $\pi^+e^\pm\mu^\mp$ or $K^+e^\pm\mu^\mp$ final states,[12] rather than for $\Lambda_c^+ \to pe^\pm\mu^\mp$. However, the underlying selection (no PID cuts, broad range of reconstructed meson mass) makes these lines suitable also for the $\Lambda_c^+ \to pe^\pm\mu^\mp$ decays. Selection requirements of the Hlt2 lines are presented in Table **V-4**.

Observable	Description of observable
p_T	Transverse momentum
χ^2_{IP}	IP significance with respect to BPV
χ^2_{track}	Track quality
P_{ghost}	Probability that track is a ghost

Table **V-2**: Observables used in the `Hlt1TrackMVA` trigger line. The observables are calculated for a single track forming Λ_c^+ candidate.

Observable	Description of observable
p	Momentum
p_T	Transverse momentum
χ^2_{IP}	IP significance with respect to BPV
χ^2_{track}	Track quality
P_{ghost}	Probability that track is a ghost
η	Pseudorapidity
$\sum p_T$	Sum of p_T for two tracks
χ^2_{VTX}	Two-track vertex quality
χ^2_{VD}	Significance of two-track vertex displacement from BPV
$DIRA$	Cosine of direction angle of two-track combination
m_{corr}	Corrected mass of two-track combination

Table **V-3**: Observables used in the `Hlt1TwoTrackMVA` trigger line. The observables are calculated for two tracks forming Λ_c^+ candidate.

The two Hlt2 lines chosen for given signal decay are complementary in terms of the selected $m(\Lambda_c^+)$ distributions. After the final selection presented in Section **V.12.1**, Λ_c^+ candidates accepted by `Hlt2RareCharmD2KEMuOS` contribute more to a lower-$m(\Lambda_c^+)$ region, while Λ_c^+ can-

[12]The Hlt2 line dedicated to $\Lambda_c^+ \to pe^\pm\mu^\mp$ decays was rejected due to its too restrictive selection on $m(\Lambda_c^+)$.

didates from `Hlt2RareCharmD2PiEMuOS` to a higher-$m(\Lambda_c^+)$ region (Fig. **V-2**). Using both lines assures more uniform mass distribution of the combinatorial background. As a result, the combinatorial background is easier to model, and can be more reliably separated from the signal.

Observable	Cut	Description of observable
	Daughter tracks	
χ^2_{track}	< 3	Track quality
p_T	> 300 MeV	Transverse momentum
p	> 2000 MeV	Momentum
χ^2_{IP}	> 5	IP significance with respect to BPV
	Two-track combination	
DOCA$_{max}$	< 0.15 mm	The largest DOCA between two tracks
$m(e^\pm\mu^\mp)$	> 250 MeV	Invariant mass of lepton pair
	$D^+ \to \pi^+ e^\pm \mu^\mp$ or $D^+ \to K^+ e^\pm \mu^\mp$	
χ^2_{VTX}	< 5	Vertex quality
χ^2_{IP}	< 25	IP significance with respect to BPV
χ^2_{VD}	> 20	Significance of vertex displacement from BPV
DIRA	> 0.9999	Cosine of direction angle
$\lvert m(D^+) - M_{D^+}\rvert$	< 200 MeV	Reconstructed mass relative to the known D^+ mass

Table **V-4**: Selection of the HLt2 lines. The Hlt2 lines in Eqs. **V.3** and **V.4** have different underlying final states, $D^+ \to \pi^+ e^\pm \mu^\mp$ or $D^+ \to K^+ e^\pm \mu^\mp$, but share the same selection requirements.

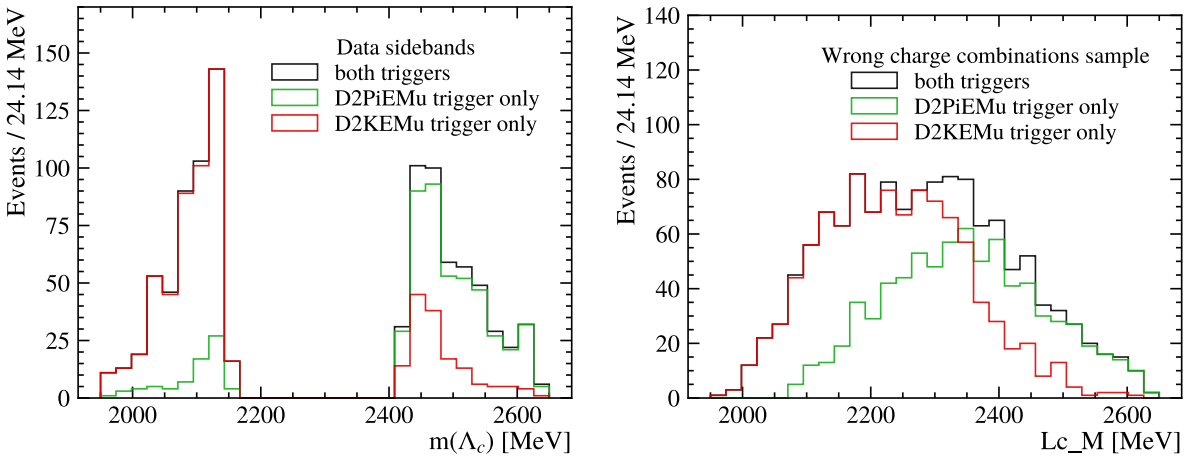

Figure **V-2**: Reconstructed Λ_c^+ mass distributions for candidates accepted by (red) `Hlt2RareCharmD2KEMuOS` only and by (green) `Hlt2RareCharmD2KEMuOS` only for (left) signal $\Lambda_c^+ \to pe^\pm\mu^\mp$ candidates with Λ_c^+ signal region blinded, and (right) wrong-charge "Λ_c" $\to pe^\pm\mu^\pm$ candidates. All the selection steps, including the final selection, have been applied.

The Λ_c^+ mass region considered in the analysis is $1786 < m(\Lambda_c^+) < 2786$ MeV. The signal region is defined as $2146 < m(\Lambda_c^+) < 2426$ MeV, and is blinded till the final fit (Section **VI**). The mass regions below and above the signal region, called *sidebands*, are used for estimating an expected yield of the combinatorial background (Section **V.9.4**).

V.4 Categories of signal decays

As already mentioned, depending on the charge combination of the final-state proton and electron, there are two signal channels considered: $\Lambda_c^+ \to pe^+\mu^-$and $\Lambda_c^+ \to pe^-\mu^+$. The former is refereed to as same-sign (SS) decay, while the latter as opposite-sign (OS) decay. Any underlying BSM effects could potentially be sensitive to these charge combinations, therefore the optimization of the final selection and UL calculations are performed independently for the two signal channels. From an experimental point of view, signal $m(\Lambda_c^+)$ shapes and efficiencies of the common selection steps are similar between the two channels. However, some differences of the combinatorial background, in its shapes and yields, are observed, as shown in Fig. **V-3**.

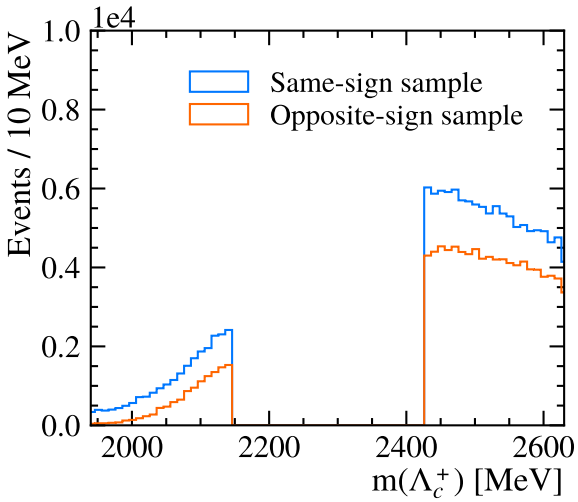

Figure **V-3**: Distributions of $m(\Lambda_c^+)$ for Λ_c^+ candidates in data sidebands for (blue) SS sample and (orange) OS sample after the stripping, triggers and preselection applied.

Additional signal categories are chosen for purely reconstruction reasons. These are signal decays reconstructed with or without bremsstrahlung photons emitted by the final-state electron (Section **III.2.8**). The corresponding samples of Λ_c^+ candidates are throughout the thesis called *brem* and *no-brem* samples, respectively. These two samples have significantly different signal $m(\Lambda_c^+)$ shapes (Fig. **V-4**). Notably, the mass distribution of the brem sample has better resolution, and the shape symmetric with respect to the known Λ_c^+ mass. A significant low-mass tail in the no-brem sample is due to the missing energy carried by unreconstructed bremsstrahlung photons. The contribution fractions of the brem and no-brem samples into the total sample are fixed based on the signal simulations to, respectively, about 36% and 64%.

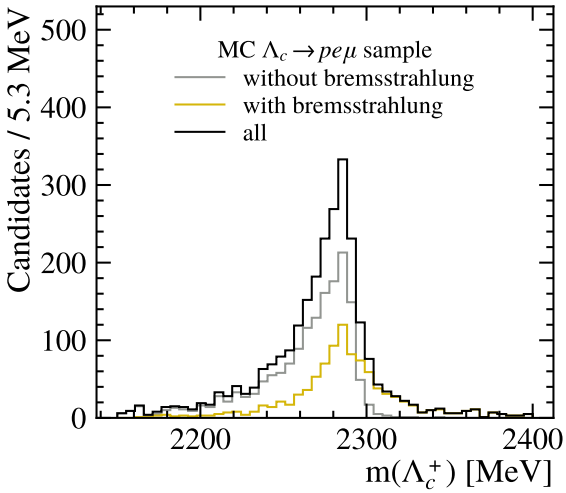

Figure **V-4**: Distributions of $m(\Lambda_c^+)$ for $\Lambda_c^+ \to pe^\pm\mu^\mp$ decays reconstructed in signal MC (orange) with and (grey) without bremsstrahlung photon, before the final selection.

Another important difference between brem and no-brem samples is in contributions of the misidentified background coming from $\Lambda_c^+ \to p\pi^+\pi^-$ decays. As pions do not emit bremsstrahlung radiation, the brem sample in simulated $\Lambda_c^+ \to p\pi^+\pi^-$ decays, reconstructed as the signal decays, is negligibly small (Section **V.8**). Therefore, the brem samples reconstructed in the data are almost free from the misidentified background.

Because of these differences in the signal shapes and background properties, the final selection is optimized independently for brem and no-brem samples; the optimization is based on independent signal and background PDFs. The final $m(\Lambda_c^+)$ fit is performed simultaneously to the brem and no-brem samples, with independent PDFs and combinatorial background yields, and the shared signal yield. The relative contributions of the misidentified background in brem and no-brem sample is fixed, which results in the shared background yield in each sample.

With these signal categories, based on the bremsstrahlung radiation and the charge combinations, the final selection is optimized independently for the four samples: SS brem, SS no-brem, OS brem and OS no-brem. The final $m(\Lambda_c^+)$ fit (Section **VI**) is performed simultaneously to SS brem and SS no-brem samples, as well as to OS brem and OS no-brem samples. Consequently, two ULs are set for the two signal decays, the SS and OS decays.

V.5 Signal and background discrimination with MVA

V.5.1 MVA methods

To efficiently distinguish between signal and background, supervised machine learning methods are employed in the analysis. The corresponding selection includes two steps, XGB1 and XGB2, and both of them are based on BDTs, from the XGBoost library [66].

Decision trees are a type of machine learning model that uses many one-dimensional cuts to classify or predict outcomes. Each internal node in a tree represents a feature or attribute, while each leaf node is assigned to a class label, in this case, signal and background. The decision-making process starts at the root node and flows down through the branches until it reaches a leaf node, which corresponds to the predicted outcome.

Ensemble methods, such as XGBoost, combine multiple models to produce a more accurate result. In the case of tree ensembles, multiple decision trees are trained, but each tree has a different subset of features, a data sample slice or a different hyperparameter setting. Predictions from each individual tree are then combined using techniques such as averaging or voting to produce a final prediction.

XGBoost stands for *Extreme Gradient Boosting*, which is an implementation of the gradient boosting algorithm. XGBoost uses an ensemble of decision trees, where each new tree is trained to correct mistakes made by the previously trained trees, with a focus on optimizing the objective function. The objective function is using a Taylor expansion up to the second order to approximate a given loss function and a regularization term that penalize model complexity.

V.5.2 Training of XGB1 and XGB2 classifiers

The XGB1 and XGB2[13] are trained on the signal MC samples, as a proxy for the signal decays in the data, while the data from the $m(\Lambda_c^+)$ sidebands in the $\Lambda_c^+ \to pe^\pm\mu^\mp$ samples are used as a combinatorial-background representation. In the MC samples, any secondary contribution is removed in order to optimize the selection for promptly-produced Λ_c^+ baryons. This approach was used in a similar analysis, comprising the search for $\Lambda_c^+ \to p\mu^+\mu^-$ decays [30], and resulted in improved discrimination capabilities.

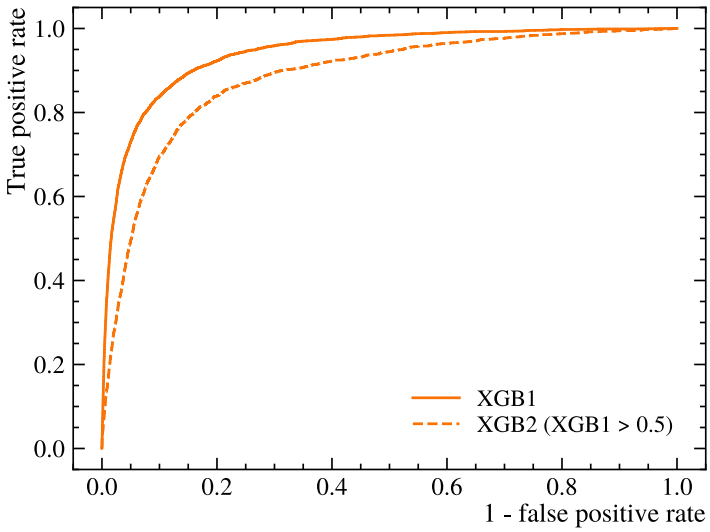

Figure **V-5**: ROC curves for XGB1 and XGB2 classifiers trained on $\Lambda_c^+ \to pe^\pm\mu^\mp$ simulations and data sidebands, calculated with folds not used during the training. XGB2 is obtained for XGB1>0.5.

The variables are selected for the MVA training based on their impact on the area under the ROC (Receiver Operating Characteristic) curve, presented in Fig. **V-5**. Initially, the model is trained with a wide set of variables, that is then reduced until the area under the ROC curve started to be significantly increased. The variables selected for both XGB1 and XGB2 are presented in Table **V-5**, additional variables underlying XGB2 are listed in Table **V-6**. The distributions comparing the MC signal and data sidebands are shown in Fig. **V-6** for the XGB1 variables, and in Fig. **V-7** for the XGB2 variables. It is important to emphasize that no observable specific

[13]XGB1 and XGB2 notation refers to either the classifiers or their outputs, depending on the context.

for electrons has been employed in these classifiers. This way, the same classifiers can also be applied to the reference decays. In addition, one avoids introducing electron-related systematic uncertainties that would not cancel out in the BF measurement relative to the reference channel.

Additional variables incorporated in the XGB2 classifier (Table **V-6**) are mainly isolation variables, which are crucial in distinguishing the signal decays from the combinatorial background. These isolation variables are based not only on features of the signal decays but also on properties of the underlying event. In particular, they quantify the degree of a spatial separation between a final-state particle trajectory and nearby tracks or decay vertices.

Variable notation	Variable description
Lc_IP_OWNPV	IP of a Λ_c^+ candidate with respect to OWNPV
Lc_IPCHI2_OWNPV	χ^2_{IP} of a Λ_c^+ candidate with respect to OWNPV
Lc_FD_OWNPV	FD of a Λ_c^+ candidate with respect to OWNPV
Lc_FDCHI2_OWNPV	significance of Λ_c^+ flight distance (χ^2_{FD})
exp(−1000Lc_TAU)	transformed decay time of a Λ_c^+ candidate
Lc_ENDVERTEX_CHI2	χ^2_{VTX} of a Λ_c^+ candidate
Lc_PT	p_T of a Λ_c^+ candidate
p_IP_OWNPV	proton IP with respect to OWNPV
p_IPCHI2_OWNPV	proton χ^2_{IP} with respect to OWNPV
p_PT	proton p_T
p_ProbNNp	proton PID
DTF_CHI2	global χ^2 of the decay-tree kinematic fit (χ^2_{DTF})

Table **V-5**: List of variables used in both, XGB1 and XGB2 classifiers. OWNPV is equivalent to BPV.

Variable notation	Variable description
mu_PT	muon p_T
mu_IP_OWNPV	muon IP with respect to OWNPV
mu_IPCHI2_OWNPV	muon χ^2_{IP} with respect to OWNPV
VTXISOBDTHARDFIRSTVALUE	vertex isolation
BSMUMUCDFISO	Λ_c^+ cone isolation
TrackIsoBDTp_TRKISOBDTTHIRDVALUE	proton track isolation

Table **V-6**: Additional variables used in the XGB2 classifier. OWNPV is equivalent to BPV.

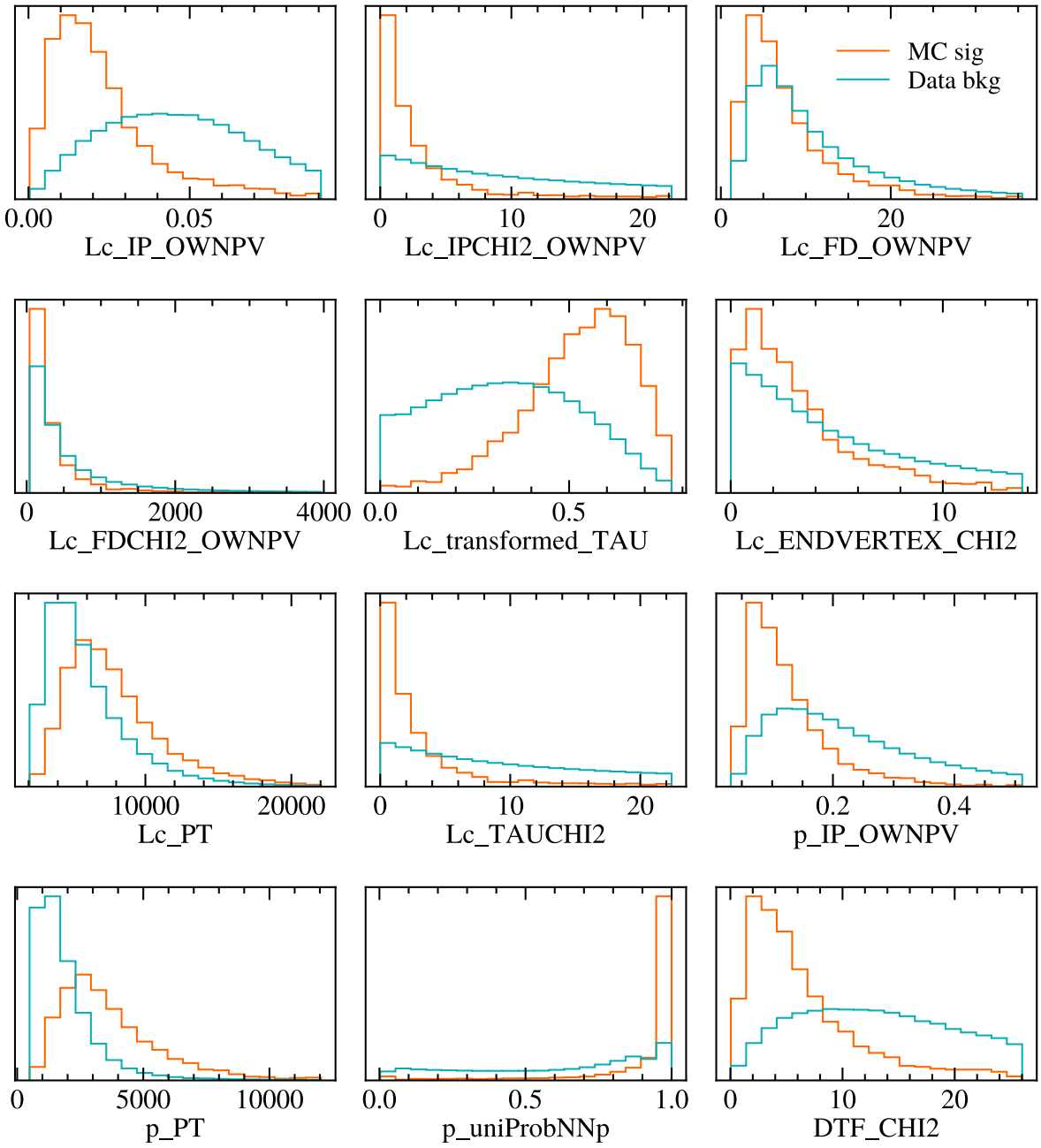

Figure **V-6**: Normalised distributions of XGB1 variables comparing (orange) MC signal and (blue) background from data sidebands. Notation used for the variables is explained in Table **V-5**.

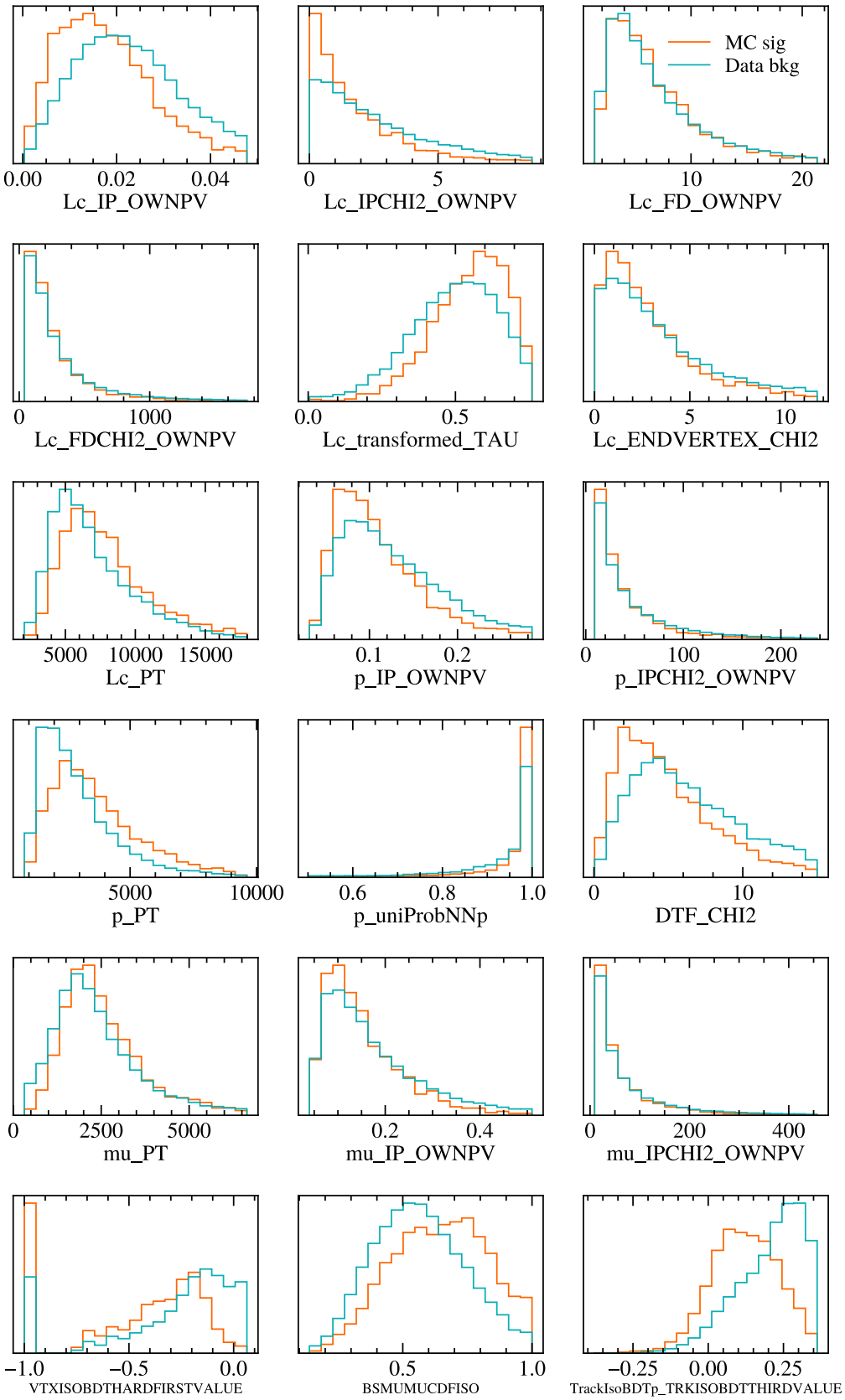

Figure **V-7**: Normalised distributions of XGB2 variables comparing (orange) MC signal and (blue) background from data sidebands. Notation used for the variables is explained in Table **V-6**.

In general, the level of a combinatorial background increases with the complexity of high-energy collisions, where numerous particles are produced simultaneously. Combinatorial background arises when unrelated particles are combined into signal candidates. This issue is more prevalent in regions with a higher density of tracks and vertices surrounding the analysed signal decay. Therefore, by utilizing isolation variables, one can suppress combinatorial background by selecting signal candidates featuring a distinct spatial separation between their daughter particles and surrounding particles from the rest of event.

Isolation variables utilized in the analysis are:

1. VTXISOBDTHARDFIRSTVALUE - a vertex isolation, calculated by refitting Λ_c^+ decay vertex with additional tracks and estimating its isolation using BDT. The exact value of this variable is equal to the highest BDT score calculated during refitting, multiplied by -1. The variables used in the BDT involve: track type, minimal value of track χ^2_{IP} relative to all PVs, track p_T, opening angle between track momentum and Λ_c^+ momentum, track χ^2_{IP}, difference in flight distance calculated with and without additional track, and χ^2_{FD} of a refitted Λ_c^+ candidate. The track in the above consideration refers to the additional track combined with given $\Lambda_c^+ \to pe^{\pm}\mu^{\mp}$ signal candidate.

2. BSMUMUCDFISO - a cone isolation [67] [68], defined as: $\frac{p_T(\Lambda_c^+)}{\sum_i p_T(x_i)+p_T(\Lambda_c^+)}$, where index i refers to particles with tracks close to a Λ_c^+ candidate. The track is counted as a close track if it fits in the 45° cone around the Λ_c^+ momentum at BPV.

3. TrackIsoBDTp_TRKISOBDTTHIRDVALUE - a track isolation between the final-state proton and other tracks reconstructed in a given event. It is the third-highest value of the BDT classifier obtained by matching the proton with other tracks, one by one. This BDT algorithm uses variables such as: track type, minimal value of track χ^2_{IP} relative to all PVs, angle between the trajectories of the proton and a matched particle, DOCA between the trajectories of the proton and a matched particle, distance between BPV and the vertex formed by the proton and a matched particle, distance between Λ_c^+ decay vertex and the vertex formed by the proton and a matched particle, and a topological variable fc, defined as:

$$fc = \frac{|\vec{p}(x) + \vec{p}(p)| \cdot \alpha^{x+p,PV}}{|\vec{p}(x) + \vec{p}(p)| \cdot \alpha^{x+p,PV} + p_T(x) + p_T(p)} \qquad \textbf{(V.5)}$$

   where x denotes matched particle, $\alpha^{x+p,PV}$ is the angle between the sum of vector-momenta of the proton and a particle x, $\vec{p}(x) + \vec{p}(p)$, and the straight line from BPV to the vertex formed by the proton and a particle x [69]. The third-highest BDT value is useful in the context of this analysis, because except proton, there are two other particles in the signal final state, electron and muon. Those are expected to be scored high by the BDT classifier. Any next particle considered is not expected to get a high score, as it is likely to originate from some other decay, and thus to be more isolated.

To maximize use of the available MC samples, a 10-fold (5-fold) cross-validation technique is used during XGB1 (XGB2) training. In this approach, the training data are split randomly into N-folds and N models are trained. Each model learns from the N$-$1 folds, and uses one remaining fold during the inference. This allows for classification of the whole dataset, without introducing any data leak into the training dataset. Given classifier predicts a value between 0 and 1 for each decay candidate, to describe probability for this candidate to be the signal decay.

For samples that are not included in the training process, namely the reference and misidentified samples, predicted XGB1 and XGB2 values are calculated as the averages from all the folds. A loose requirement on the XGB1 output, XGB1> 0.5, has been applied before the XGB2 training.

The distributions of the XGB1 and XGB2 responses for the signal and reference MC samples, as well as the background sample, are presented in Fig. **V-8**. Both classifiers give good separation between the signal and the background. One can notice that the distributions for the signal MC sample and the reference MC sample are similar, which is important for retaining high efficiency for selecting the reference decays as well.

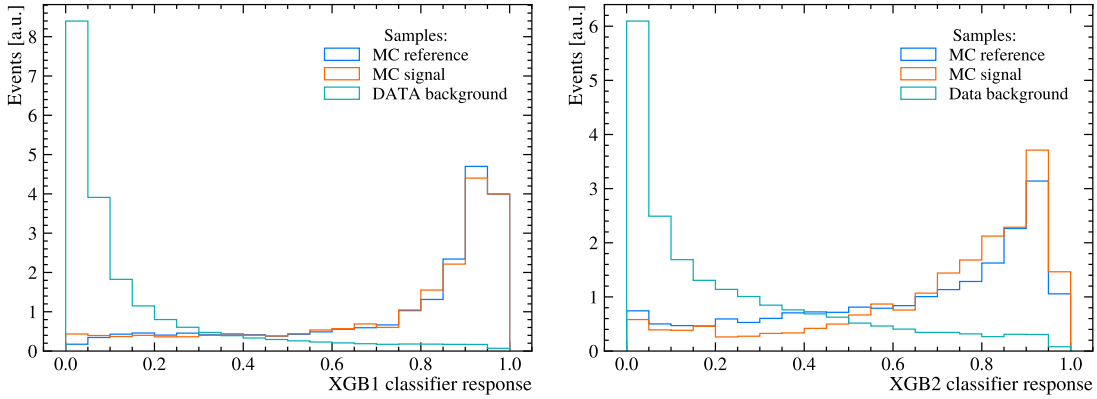

Figure **V-8**: Response of (left) XGB1 classifier and (right) XGB2 classifier for MC of the (orange) signal and (blue) reference decays, and (green) background from $\Lambda_c^+ \to pe^\pm\mu^\mp$ data sidebands. Distributions are normalized to have the same areas.

V.6 Selection of reference channel

The selection applied when reconstructing reference decays, $\Lambda_c^+ \to p\phi$, with $\phi \to \mu^+\mu^-$, is as much as possible aligned with that used at each analysis step for the signal decays. The stripping line employed is `StrippingLc23MuLc2pmumuLine`, within which the $\Lambda_c^+ \to p\mu^+\mu^-$ candidates are constructed. The selection is the same as for the signal decays (Table **V.3.1**), except that the muon PID requirements are applied for both leptons. The trigger selections at the L0 and Hlt1 levels are also the same as for the signal decays (Eqs. **V.1** and **V.2**), whereas the selection at the Hlt2 level is:

```
Lc_Hlt2RareCharmD2KMuMuOSDecision_TOS ==1 OR
Lc_Hlt2RareCharmD2PiMuMuOSDecision_TOS ==1.
```
(**V.6**)

The Hlt2 lines used are dedicated for reconstructing charm mesons decays to $K^+\mu^+\mu^-$ and $\pi^+\mu^+\mu^-$ final states. The reason behind this choice is the same as for the Hlt2 lines chosen for the signal channels (Section **V.3.2**). The selection of these lines is the same as of the Hlt2 lines used for the signal decays (Table **V-4**).

The preselection involves proton PID requirement, `p_ProbNNp`> 0.5, as well as the ϕ region selection imposed by requiring that the $\mu^+\mu^-$ invariant mass is consistent with the known mass and natural width of the ϕ state, $959 < m(\mu^+\mu^-) < 1079$ MeV. As already mentioned, the XGB1 and XGB2 classifiers are constructed in such a way that they are straightforward to apply also for the reference channel (Fig. **V-8**). Similar to the signal selection, XGB1> 0.5 requirement is imposed.

V.6.1 Reference sample after the preselection

The mass distribution for the $\Lambda_c^+ \to p\phi$ candidates, satisfying the preselection described above, and additional cut on muon PID, `mu_ProbNNmu` > 0.7, is shown in Fig. **V-9**. The clear peak is visible close to the known Λ_c^+ mass. The $m(\Lambda_c^+)$ distribution is fitted using a sum of two Gaussian functions to describe the $\Lambda_c^+ \to p\phi$ signal, a second-order polynomial to model the combinatorial background and a sum of three Gaussian functions to model the misidentified background from $\Lambda_c^+ \to p\pi^+\pi^-$ decays (Section **V.9.3**). The measured $\Lambda_c^+ \to p\phi$ yield is 636 ± 32 events and the yield of the misidentified background is 45 ± 23 events.

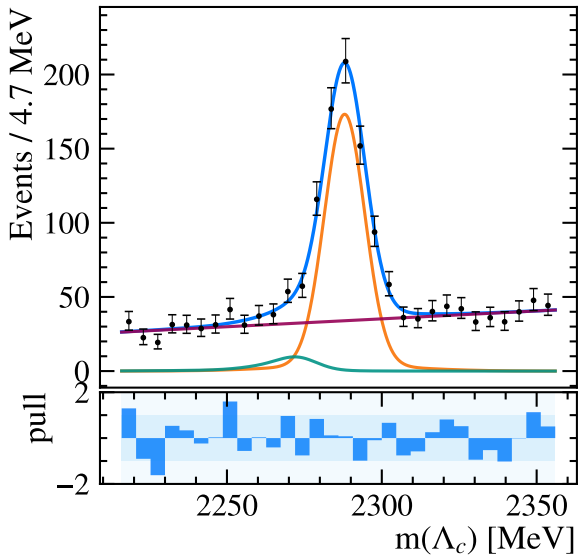

Figure **V-9**: Distribution of $m(\Lambda_c^+)$ for $\Lambda_c^+ \to p\phi$ sample after preselection and `mu_ProbNNmu` > 0.7 cut. Fit results are superimposed with (orange) $\Lambda_c^+ \to p\phi$ signal contribution, (green) misidentified background and (red) combinatorial background.

Based on the fit results shown in Fig. **V-9**, the $\Lambda_c^+ \to p\phi$ decays are unfolded from the selected reference sample with the sPlot method [70]. This procedure allows for a statistical extraction of the signal from the data that contain both signal and background, described with given PDFs. They are fitted to the data and, as a result, each data point, here each Λ_c^+ candidate, has an sWeight assigned[14]. The sum of obtained signal sWeights is equal to the signal yield measured in the fitted data sample. The sWeighted sample of the $\Lambda_c^+ \to p\phi$ decays (Fig. **V-9**) is used to estimate corrections for the data-MC difference in Section **V.7.2**.

V.7 Corrections to simulation samples

V.7.1 Particle identification

In some cases, simulations differ from data that they should imitate. In the LHCb simulation, there are some known issues that need to be taken into account in most data analyses. One of them is a poor modelling of the particle identification, which results in significant differences of the PID distributions between data and MC samples. To solve this problem, the PID calibration

[14]Signal sWeight can be, to some extent, interpreted as the probability of originating from signal PDF.

is performed, in which the simulated PID distributions are replaced by the ones based on the calibration data [71][72]. The decay channels used for the PID calibration have large yields and purity, and can be reconstructed without using PID information for a particle being calibrated. To provide both, low-momentum (soft) and high-momentum (hard) electrons, muons, pions, kaons and protons, the following calibration decays are typically used: $J/\psi \to e^+e^-$, $D_s^+ \to \mu^+\mu^-\pi^+$, $J/\psi \to \mu^+\mu^-$, $K_S^0 \to \pi^+\pi^-$, $D^{*+} \to D^0\pi^+$, with $D^0 \to K^-\pi^+$, $\Lambda^0 \to p\pi^-$, and $\Lambda_c^+ \to pK^-\pi^+$.

A given calibration sample is divided into bins of variables that are correlated with PID: p_T of a calibrated particle, its η and the number of tracks in the underlying event. A reference PID distribution is obtained in each three-dimensional bin considered. A new, calibrated PID distribution is sampled from the reference distribution using the dedicated tool, `PIDGen2`. Additionally, smoothing technics are applied. In the presented analysis, the PID variables corrected that way are `p_probNNp` in all the MC samples, as well as `mu_probNNmu` and `e_probNNe` in simulation samples of the signal and reference decays. The calibration impact on the PID distributions is presented in Fig. **V-10**.

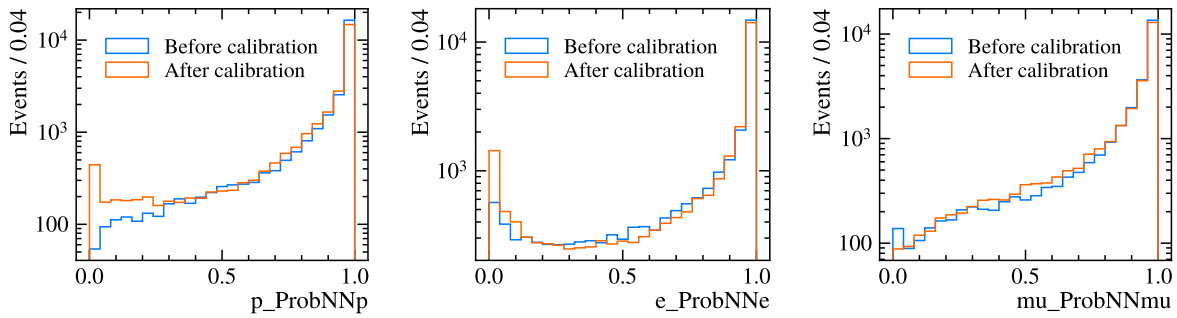

Figure **V-10**: PID observables for the signal MC sample (blue) before and (orange) after the calibration.

The calibrated PID observables assure correct estimation of a PID efficiency, defined as the fraction of correctly identified particles of a given type, as well as a misidentification (misID) rate corresponding to the fraction of wrongly identified particles. Such misID rates are used for estimating the misidentified background from $\Lambda_c^+ \to p\pi^+\pi^-$ decays, described in Section **V.8**.

V.7.2 Corrections based on the reference sample

To investigate possible data-MC differences, various kinematical and topological distributions are compared between the sWeighted $\Lambda_c^+ \to p\phi$ data (Section **V.6.1**) and the $\Lambda_c^+ \to p\phi$ simulation. All the preselection steps (prior to the XGB1 requirement), are applied to the simulation sample, to align the selection with that for the $\Lambda_c^+ \to p\phi$ data. In general, there is a good agreement between the $\Lambda_c^+ \to p\phi$ data and corresponding simulations, except for the two distributions: p_T of the Λ_c^+ baryons and the number of tracks (nTracks) in the underlying event. This is consistent with what was found in the $\Lambda_c^+ \to p\mu^+\mu^-$ analysis [30].

In order to correct for these discrepancies, weights in the two-dimensional space, $p_T(\Lambda_c^+)$ vs. nTracks, are applied to all the simulation samples. These weights are determined by dividing the $p_T(\Lambda_c^+)$ vs. nTracks distribution from the sWeighted $\Lambda_c^+ \to p\phi$ data by the corresponding distribution from the $\Lambda_c^+ \to p\phi$ simulations. The distributions of the $p_T(\Lambda_c^+)$ and nTracks from the signal MC sample, compared before and after applying the above corrections, are shown in Figure **V-11**.

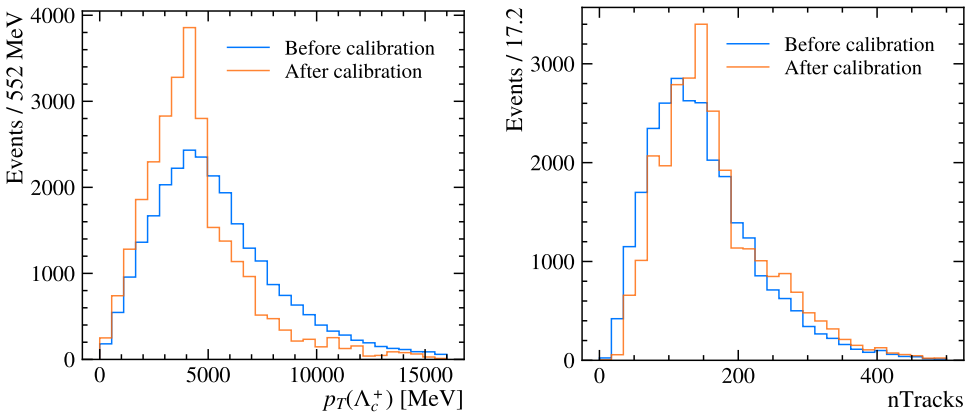

Figure **V-11**: Distributions of (left) $p_T(\Lambda_c^+)$ and (right) nTracks from the signal MC sample, (blue) before and (orange) after corrections based on the reference sample.

V.7.3 Reweighing of $\Lambda_c^+ \to p\pi^+\pi^-$ phase space

The simulation sample of $\Lambda_c^+ \to p\pi^+\pi^-$ decays is produced using the non-resonant three-body decay model. These decays are known to proceed through intermediate resonances, though $\Lambda_c^+ \to p\pi^+\pi^-$ decay model has not been measured yet. The Dalitz distribution for $\Lambda_c^+ \to p\pi^+\pi^-$ decays, $m^2(\pi^+\pi^-)$ vs. $m^2(p\pi^-)$, with background subtracted and efficiency corrections applied, was measured by LHCb in Ref. [73]. The Dalitz distribution reproduced from that measurement, divided by the Dalitz distribution for the non-resonant $\Lambda_c^+ \to p\pi^+\pi^-$ decays, provides weights, which allow for obtaining the $\Lambda_c^+ \to p\pi^+\pi^-$ sample with a realistic phase-space distribution. These weights were evaluated in Ref. [30], and used in the presented analysis to correct the $\Lambda_c^+ \to p\pi^+\pi^-$ simulation sample.

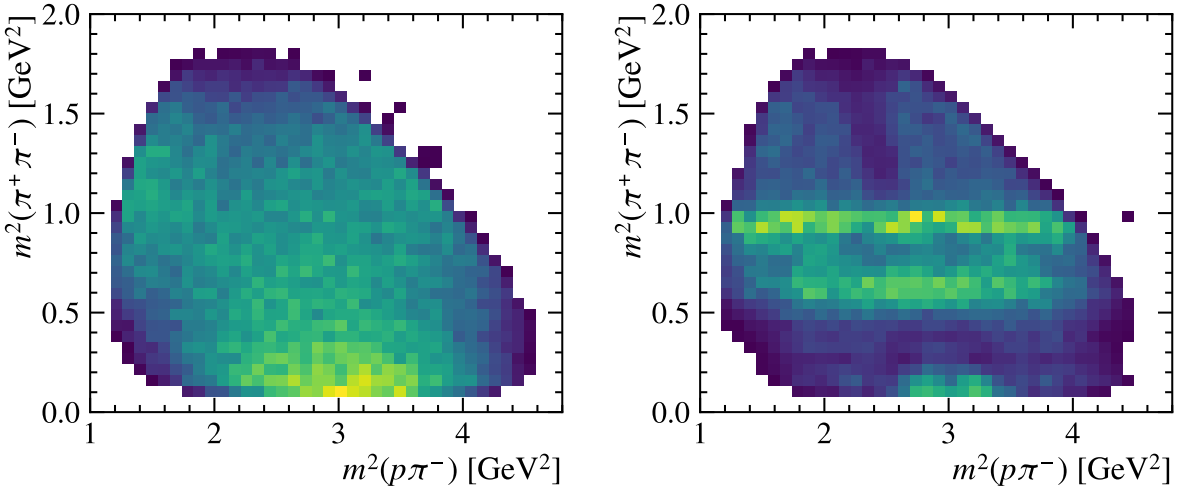

Figure **V-12**: Phase-space distribution of $\Lambda_c^+ \to p\pi^+\pi^-$decays (left) before and (right) after reweighing.

The results of this reweighing are presented in Figure **V-12**, which compares the Dalitz distributions for the $\Lambda_c^+ \to p\pi^+\pi^-$ simulations before and after applying the corrections. The presented $\Lambda_c^+ \to p\pi^+\pi^-$ sample is after the stripping selection (Table **V-1**), but the final-state

pions are reconstructed assuming the pion mass, and no PID requirements are placed on them. This treatment, necessary for the calibration purpose, is different from the default analysis, in which the simulated $\Lambda_c^+ \to p\pi^+\pi^-$ decays are reconstructed as the signal decays, i.e. assuming the muon and electron masses for the pions (Section **V.8**).

This calibration of $\Lambda_c^+ \to p\pi^+\pi^-$ decays is important for having realistic kinematic distributions of the final-state pions. The pion kinematics is correlated with the rates for $\pi \to \mu$ and $\pi \to e$ misidentification, and thus affects the estimation of the misidentified background yield (Section **V.8**).

V.8 Misidentified background

V.8.1 Mass shapes and categories

One of the main factors that affects the sensitivity of the search for $\Lambda_c^+ \to pe^\pm\mu^\mp$ decays is the amount of the misidentified background from $\Lambda_c^+ \to p\pi^+\pi^-$ decays. In contrast to the combinatorial background, it peaks in the Λ_c^+ mass spectrum close to the nominal Λ_c^+ mass, as shown in Fig. **V-13**. The misidentified background is only relevant for the samples of $\Lambda_c^+ \to pe^\pm\mu^\mp$ candidates reconstructed without bremsstrahlung radiation. As demonstrated in Fig. **V-14**, the brem sample comprises only about 4% of the misidentified $\Lambda_c^+ \to p\pi^+\pi^-$ decays. Therefore, requiring a bremsstrahlung photon suppresses misidentified background to a negligible level. Pions are much heavier than electrons, thus they do not emit (significant) bremsstrahlung radiation; any photons associated here with pions are usually random. As a result, the Λ_c^+ mass measured for the brem sample of the misidentified background is, compared to the no-brem sample, overestimated by the energy of the associated photon (Fig. **V-14**). The $m(\Lambda_c^+)$ distribution for the brem sample is shifted above the nominal Λ_c^+ mass. On the other hand, the $m(\Lambda_c^+)$ distribution for the no-brem sample of the misidentified background is shifted below the nominal Λ_c^+ mass, as the electron and muon masses assumed for the final-state pions are smaller than the nominal pion mass.

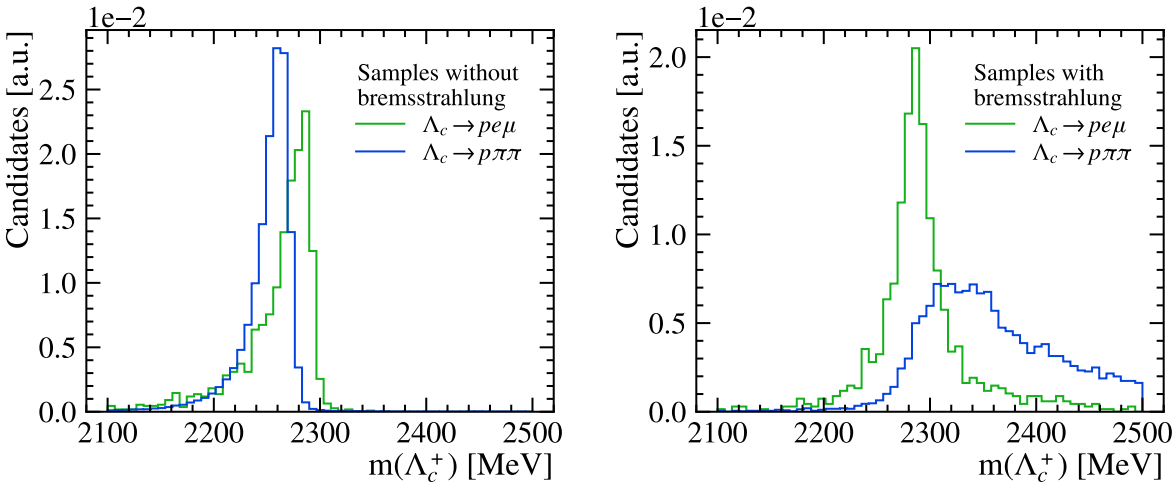

Figure **V-13**: Comparison of $m(\Lambda_c^+)$ distribution for (blue) misidentified background from $\Lambda_c^+ \to p\pi^+\pi^-$ decays and (green) signal $\Lambda_c^+ \to pe^\pm\mu^\mp$ decays in (left) no-brem and (right) brem samples reconstructed from simulations.

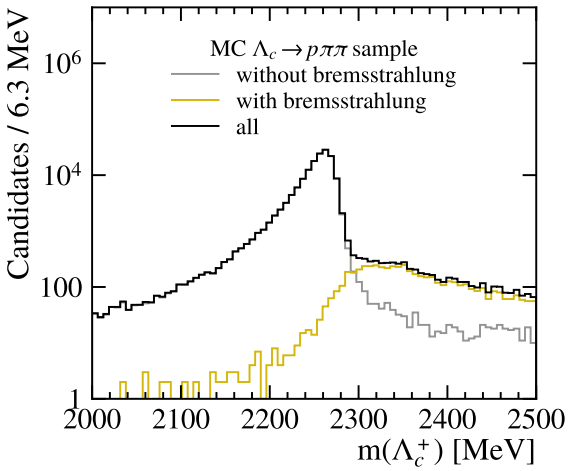

Figure **V-14**: Comparison of $m(\Lambda_c^+)$ distribution for (grey) no-brem and (orange) brem samples of the misidentified background from $\Lambda_c^+ \to p\pi^+\pi^-$ decays reconstructed from simulations.

V.8.2 Estimation of misID rates

As already mentioned, the simulated $\Lambda_c^+ \to p\pi^+\pi^-$ decays are reconstructed as the $\Lambda_c^+ \to pe^\pm\mu^\mp$ signal decays, namely the muon mass is assumed for one of the final-state pions, while the electron mass for the other one. Such misidentified decays undergo the same selection as the signal decays, except for PID requirements on the electron and muon, which are not applied. As shown below, the rates for $\pi \to e$ and $\pi \to \mu$ misID are small, therefore applying the PID selection would remove the majority of the $\Lambda_c^+ \to p\pi^+\pi^-$ simulated events.

Instead, the misID rates for the relevant PID requirements, are used to estimate the expected yield of the misidentified background. This estimation is based on the assumption that the misID rates for $\pi \to e$ and $\pi \to \mu$ are uncorrelated. Thus, the $\pi \to e$ and $\pi \to \mu$ misID rates are calculated independently using the `PIDCalib2` tool [74][75]. This calibration tool exploits a very similar method to that used for the PID calibration (Section **V.7.1**), and relies on the same calibration data samples. For a PID selection provided, misID rates are calculated in the binned space of three variables: p_T and η of a misidentified particle, as well as the number of SPD hits (nHits) registered in the event. In this analysis, the binning is optimised to keep enough statistics in each bin, while maximizing the number of bins. In particular, the p_T binning is carefully chosen to obtain meaningful estimates for low-p_T leptons.

The above procedure is applied to the PID requirements in the stripping selection (Table **V-1**), and also used to scan the full range of the PID requirements placed on `e_ProbNNe` and `mu_ProbNNmu`. The $\pi \to e$ misID rate as a function of `e_ProbNNe` cut, and the $\pi \to \mu$ misID rate as a function of `mu_ProbNNmu` cut are presented in Fig. **V-15**. The misID rates are estimated for misidentified $\Lambda_c^+ \to p\pi^+\pi^-$ decays separately for simulations of each data-taking year and magnet-polarity configurations. The misID rates for the final `mu_ProbNNmu` and `mu_ProbNNmu` requirements (Section **V.12**) are small, at the level of 10^{-3}. However, the relatively large BF of $\Lambda_c^+ \to p\pi^+\pi^-$ decays, at the 10^{-3} level [19], makes the misidentified background potentially significant.

The rates in Fig. **V-15** are applied to the misidentified $\Lambda_c^+ \to p\pi^+\pi^-$ decays, by assigning the $\pi \to e$ and $\pi \to \mu$ misID rates for each Λ_c^+ candidate depending on the p_T and η of its lepton daughters, and nHits in the underlying event. The product of these misID rates, multiplied by

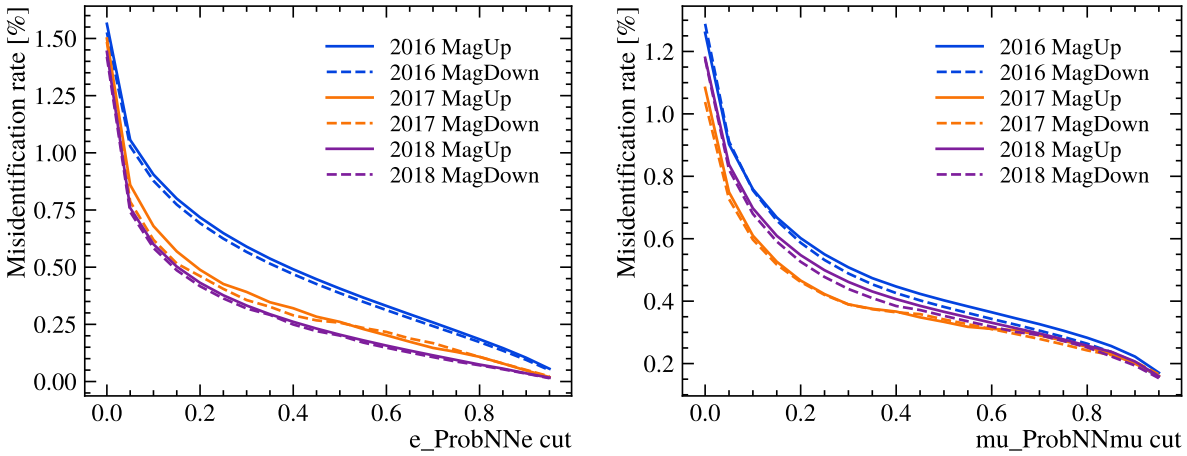

Figure **V-15**: (Left) $\pi \to e$ misID rate as a function of `e_ProbNNe` cut, and (right) $\pi \to \mu$ misID rate as a function of `mu_ProbNNmu` cut, estimated based on simulated $\Lambda_c^+ \to p\pi^+\pi^-$ decays misidentified as $\Lambda_c^+ \to pe^\pm\mu^\mp$ decays. The misID rates are given separately for each data-taking year and magnet-polarity configurations, as specified in the legend.

efficiencies of the other selection steps, allows to estimate the expected yield of the misidentified background for given `e_ProbNNe` and `mu_ProbNNmu` selection (Section **V.11.1**). These yields are used as an input to the final optimization (Section **V.12**).

The above considerations are valid for studying the misidentified background in the signal sample. A similar type of background from $\Lambda_c^+ \to p\pi^+\pi^-$ decays is expected to contribute into the reference sample, but with both pions being misidentified as muons. In this case, the product of the $\pi \to \mu$ misID rates is considered in estimating the background yield.

V.9 Modelling of $m(\Lambda_c^+)$ shapes

As mentioned before, the signal decays are identified using the mass of reconstructed Λ_c^+ candidates, $m(\Lambda_c^+)$, measured as the invariant mass of the $pe^\pm\mu^\mp$ final state. For the reference channel, the $m(\Lambda_c^+)$ observable corresponds to the invariant mass of the $p\mu^+\mu^-$ final state, with the $\mu^+\mu^-$ invariant mass selected in the ϕ region.

Selected data samples of Λ_c^+ candidates contain contributions from the signal, the misidentified background, and the combinatorial background. In order to separate them and disentangle the signal, the $m(\Lambda_c^+)$ shape is first modelled separately for each of the contributions. The shapes of the signal decays, the reference channel, and the misidentified background from $\Lambda_c^+ \to p\pi^+\pi^-$decays are measured using the corresponding simulation samples. These samples are calibrated as described in Section **V.7**. Each simulation sample is fitted using the unbinned-likelihood fit with parametric PDFs. Specific functions are chosen for each sample to precisely describe its measured properties, while the parameter values of these functions are obtained through performing the fits. The mass shapes of the combinatorial background are modelled using non-parametric approach and based on both, the mass sidebands in the signal sample, and the full mass spectrum from the wrong-charge data.

The studies presented in this Section are performed for the simulation and data samples selected after the stripping, trigger and preselection steps, as well as the XGB1 selection. The developed mass modelling approach is used in the final optimisation (Section **V.12**), taking into

account changes upon changing requirements on the underlying observable: the XGB2 output, `e_ProbNNe` and `mu_ProbNNmu`. The mass shapes after applying the final selection remain largely unchanged (Section **V.12.2**).

V.9.1 Modelling of signal shape

The signal shapes differ between the brem and no-brem categories (Section **V.4**), thus are modelled separately. On the other hand, the shapes are similar for the SS signal channel $\Lambda_c^+ \to pe^+\mu^-$ and the OS signal channel $\Lambda_c^+ \to pe^-\mu^+$, as both are assumed to proceed through non-resonant decays.

The PDF used for the brem sample is the sum of two Gaussian functions, which share a common mean (m_0), but have distinct widths (σ and σ_1). This double-Gaussian model effectively captures the signal properties: the narrower *core* Gaussian (contributing with the fraction f) describes a subsample reconstructed with a better resolution, while the broader Gaussian models a subsample affected by various experimental imperfections.

The no-brem signal sample is modelled using a Crystal Ball function [76]. This function has a Gaussian core (with σ width), providing a smooth and symmetric distribution around the mean value (m_0), and a power-law tail extending below a predefined mass threshold. This feature allows to effectively model processes with missing energy, such as not recovered bremsstrahlung radiation. The Crystal Ball function is defined as:

$$CB(m; m_0, \sigma, \alpha, n) = \begin{cases} \exp\left(-\frac{(m-m_0)^2}{2\sigma^2}\right), & \text{for } \frac{m-m_0}{\sigma} > -\alpha \\ A \cdot \left(B - \frac{m-m_0}{\sigma}\right)^{-n}, & \text{for } \frac{m-m_0}{\sigma} \leqslant -\alpha \end{cases} \quad \textbf{(V.7)}$$

where

$$A = \left(\frac{n}{|\alpha|}\right)^n \cdot \exp\left(-\frac{|\alpha|^2}{2}\right), \; B = \frac{n}{|\alpha|} - |\alpha|\,, \quad \textbf{(V.8)}$$

with a power-law tail described with an exponent n, for mass values below the threshold given by α.

Sample/Parameter	m_0 [MeV]	σ [MeV]	σ_1 [MeV]	f [%]	n	α
brem	2286.7 ± 1.3	14.1 ± 2.3	53.3 ± 6.3	0.47 ± 0.08	–	–
no-brem	2281.4 ± 1.1	10.2 ± 0.7	–	–	6.0 ± 2.1	0.41 ± 0.06

Table **V-7**: Parameter values obtained from $m(\Lambda_c^+)$ fits to SS $\Lambda_c^+ \to pe^+\mu^-$ simulation samples.

Sample/Parameter	m_0 [MeV]	σ [MeV]	σ_1 [MeV]	f [%]	n	α
brem	2286.0 ± 1.1	13.6 ± 1.7	58.5 ± 9.5	0.61 ± 0.06	–	–
no-brem	2281.2 ± 1.4	10.2 ± 0.9	–	–	7.7 ± 2.3	0.35 ± 0.05

Table **V-8**: Parameter values obtained from $m(\Lambda_c^+)$ fits to OS $\Lambda_c^+ \to pe^-\mu^+$ simulation samples.

The $m(\Lambda_c^+)$ distributions for all the signal categories considered, along with the fit results, are presented in Fig. **V-16**. The fit parameters are summarised in Tables **V-8** and Tables **V-7**.

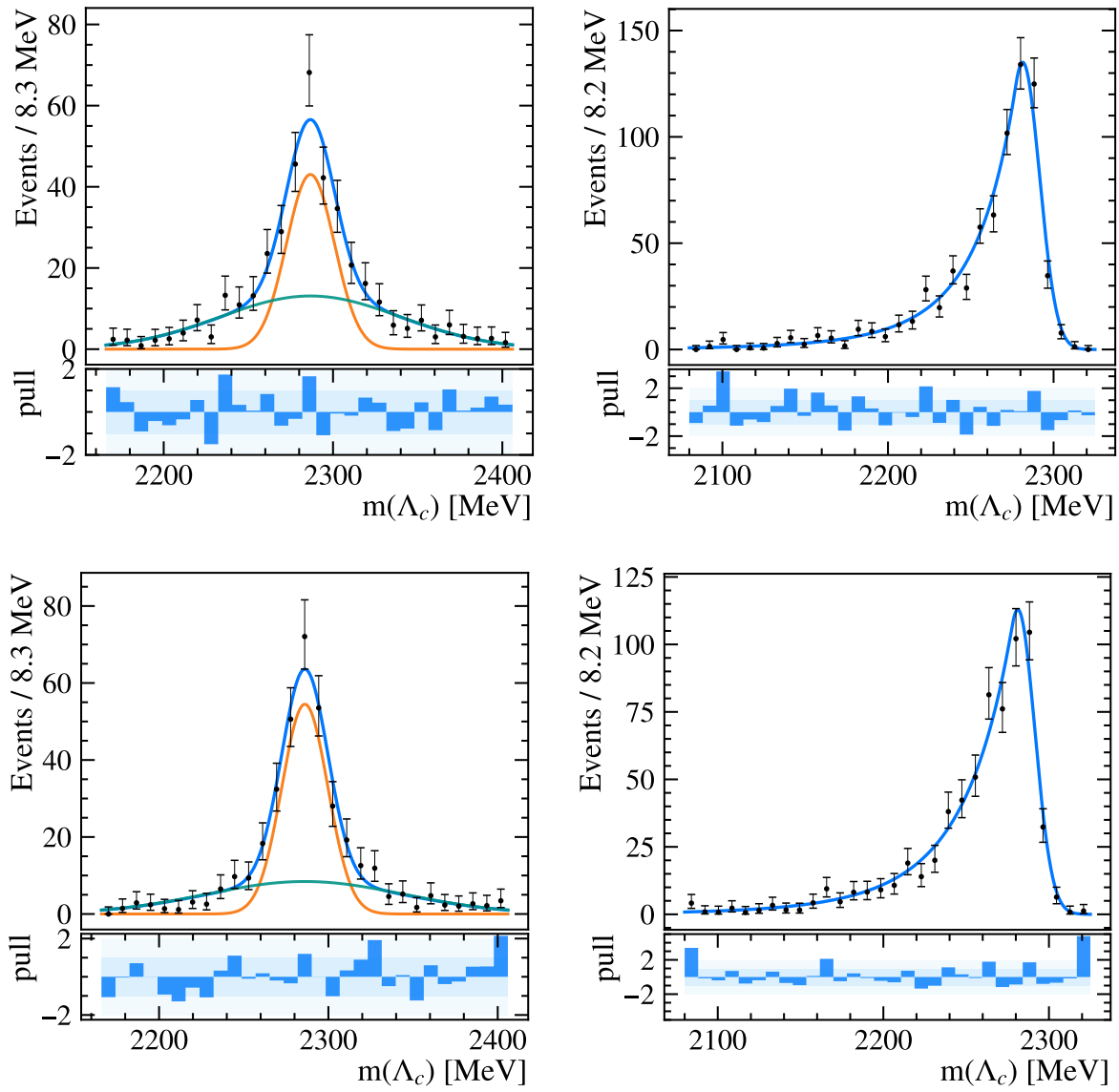

Figure **V-16**: Distribution of $m(\Lambda_c^+)$ for the signal simulation for (top) SS and (bottom) OS samples, (left) with and (right) without bremsstrahlung radiation recovered. The fit results are superimposed.

V.9.2 Modeling of reference-decay shape

The reference $\Lambda_c^+ \to p\phi$ simulation sample is fitted using a double Gaussian function, similarly to the signal decays in the brem category. The reference decays do not involve electrons, and thus do not require any brem recovery. Therefore, there is only one category for the reference channel. Its $m(\Lambda_c^+)$ distribution, along with the fit results, is shown in Fig. **V-17**. The fit parameters are summarised in Table **V-9**.

m_0 [MeV]	σ [MeV]	σ_1 [MeV]	f [%]
2288.05 ± 0.10	6.40 ± 0.15	14.8 ± 1.6	0.88 ± 0.03

Table **V-9**: Parameter values obtained from $m(\Lambda_c^+)$ fits to $\Lambda_c^+ \to p\phi$ simulation sample.

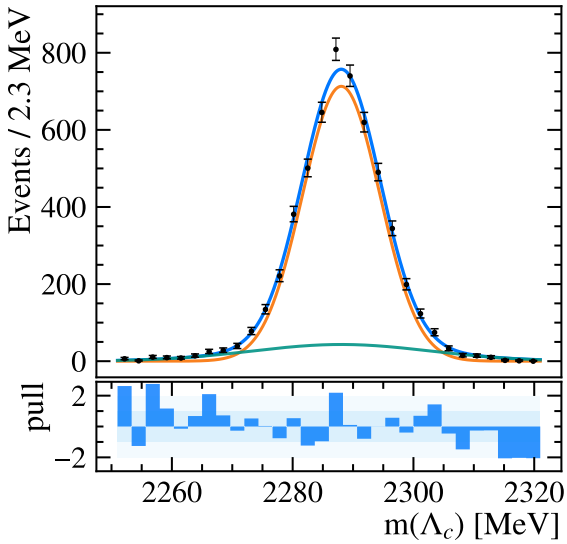

Figure **V-17**: Distribution of $m(\Lambda_c^+)$ for the $\Lambda_c^+ \to p\phi$ simulations. The fit results are superimposed.

V.9.3 Shapes of misidentified background

The $\Lambda_c^+ \to p\pi^+\pi^-$decays misidentified as $\Lambda_c^+ \to pe^\pm\mu^\mp$ signal are significantly affected by the presence of the bremsstrahlung radiation (Section **V.8.1**), and thus their brem and no-brem categories are modelled separately. The no-brem sample is fitted with the sum of a Crystal Ball function and a Gaussian function. The brem sample is modelled with a reversed Crystal Ball function, in which α is negative to describe a tail in the higher masses above the peak. A high-mass tail is due to a wrongly associated bremsstrahlung photon. As discussed in Section **V.8.1**, the brem sample of the misidentified $\Lambda_c^+ \to p\pi^+\pi^-$ decays is largely suppressed.

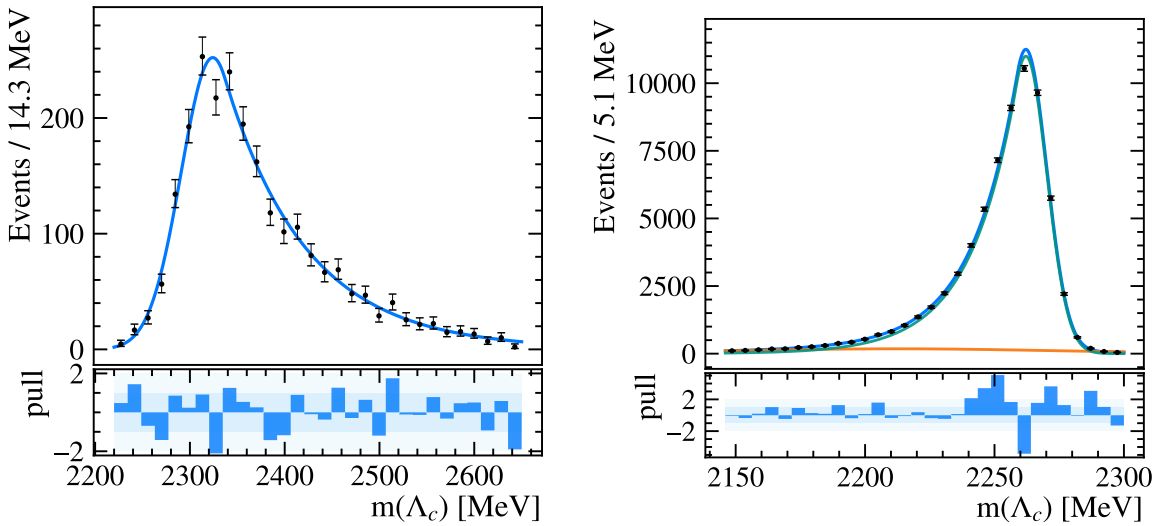

Figure **V-18**: Distribution of $m(\Lambda_c^+)$ for $\Lambda_c^+ \to p\pi^+\pi^-$ decays misidentified as $\Lambda_c^+ \to pe^\pm\mu^\mp$ decays for (left) brem and (right) no-brem category. The fit results are superimposed.

To have a sufficient number of events in this sample, the $\Lambda_c^+ \to p\pi^+\pi^-$ simulations are about

three times larger than the signal simulations. As a result, the no-brem sample is of a relatively large statistics. The $m(\Lambda_c^+)$ distributions for both categories of the misidentified background in the signal channels, along with the fit results, are presented in Fig. **V-18**.

The misidentified background in the reference channel is described with the sum of three Gaussian functions of independent means and widths. The $m(\Lambda_c^+)$ distribution for $\Lambda_c^+ \to p\pi^+\pi^-$ decays misidentified as $\Lambda_c^+ \to p\phi$ decays is shown in Fig. **V-19** along with the fit results.

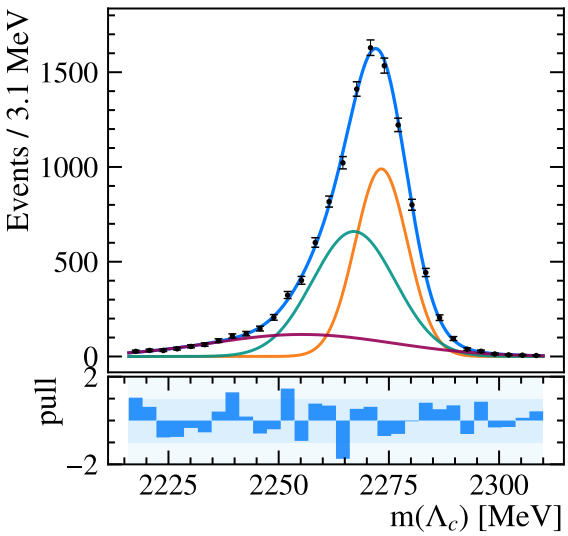

Figure **V-19**: Distribution of $m(\Lambda_c^+)$ for $\Lambda_c^+ \to p\pi^+\pi^-$ decays misidentified as $\Lambda_c^+ \to p\phi$ decays. The fit results are superimposed.

V.9.4 Shapes of combinatorial background

Shapes based on wrong-charge data

Shapes of the combinatorial background distributions are modelled with a kernel density estimation (KDE) applied to the data samples with wrong-charge combinations. The KDE uses a kernel smoothing technique to approximate a continuous PDF of a random variable. This non-parametric method is chosen due to the relatively wide fit range that leads to a challenging shape of the combinatorial background distribution. In this case, a Gaussian kernel with the width of 30 MeV gives satisfactory results for both brem and no-brem samples. The $m(\Lambda_c^+)$ distributions for these samples, together with the obtained shapes, are presented in Fig. **V-20**.

The wrong-charge combinations involve the same charge for both leptons, $pe^+\mu^+$ or $pe^-\mu^-$. In the SS and OS signal categories, respectively $\Lambda_c^+ \to pe^+\mu^-$ and $\Lambda_c^+ \to pe^-\mu^+$, the charges of leptons are opposite. Because of that, the wrong-charge data cannot be split into the SS and OS categories, and the total sample is used to model the combinatorial background for both SS and OS signal decays. The wrong-charge sample is largely dominated by the $pe^-\mu^-$ combinations. The $pe^+\mu^+$ combinations have lower reconstruction efficiency, as they are even more *exotic*.

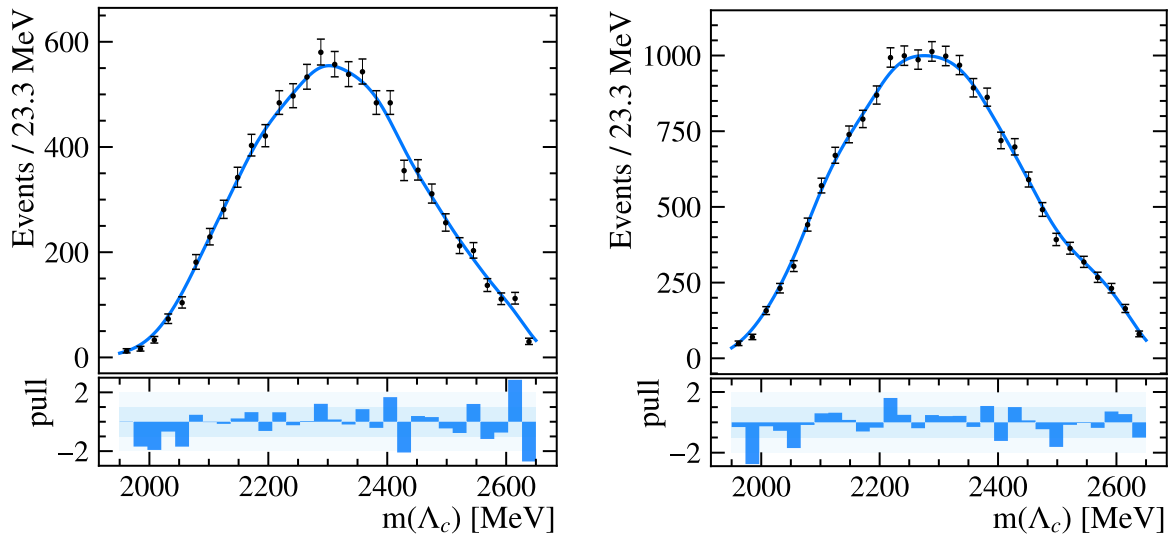

Figure **V-20**: Distribution of $m(\Lambda_c^+)$ for data with wrong-charge combinations for (left) brem and (right) no-brem samples. Shapes approximated with the KDE method are superimposed. Additional cut, `e_ProbNNe`>0.1, is applied to the no-brem sample, to align the selection in sideband-based studies below.

Comparison with signal sidebands

At this stage of the analysis, the signal regions in the reconstructed signal samples are blinded. However, studying the mass sidebands is useful to verify applicability of the wrong-charge data, and to estimate expected yields of the combinatorial background before the unblinding. The low- and high-mass sidebands are defined respectively as: $1786 < m(\Lambda_c^+) < 2146$ MeV and $2426 < m(\Lambda_c^+) < 2786$ MeV.

The mass shapes estimated for the wrong-charge data are compared with the $m(\Lambda_c^+)$ distributions measured in the data sidebands of the signal samples. To enable this comparison, the wrong-charge data in their sidebands are normalised to the number of events in the sidebands of the signal samples.

The wrong-charge data in the brem sample matches shapes of the signal-data sidebands well (Fig. **V-21** (left)), but the no-brem sample required an additional selection to achieve that. The requirement `e_ProbNNe`>0.1 is introduced to the no-brem sample, which results in a good agreement with the sidebands in the signal sample. Consequently, the minimal cut on `e_ProbNNe` considered in the final optimisation is chosen as 0.1 (Section **V.12**).

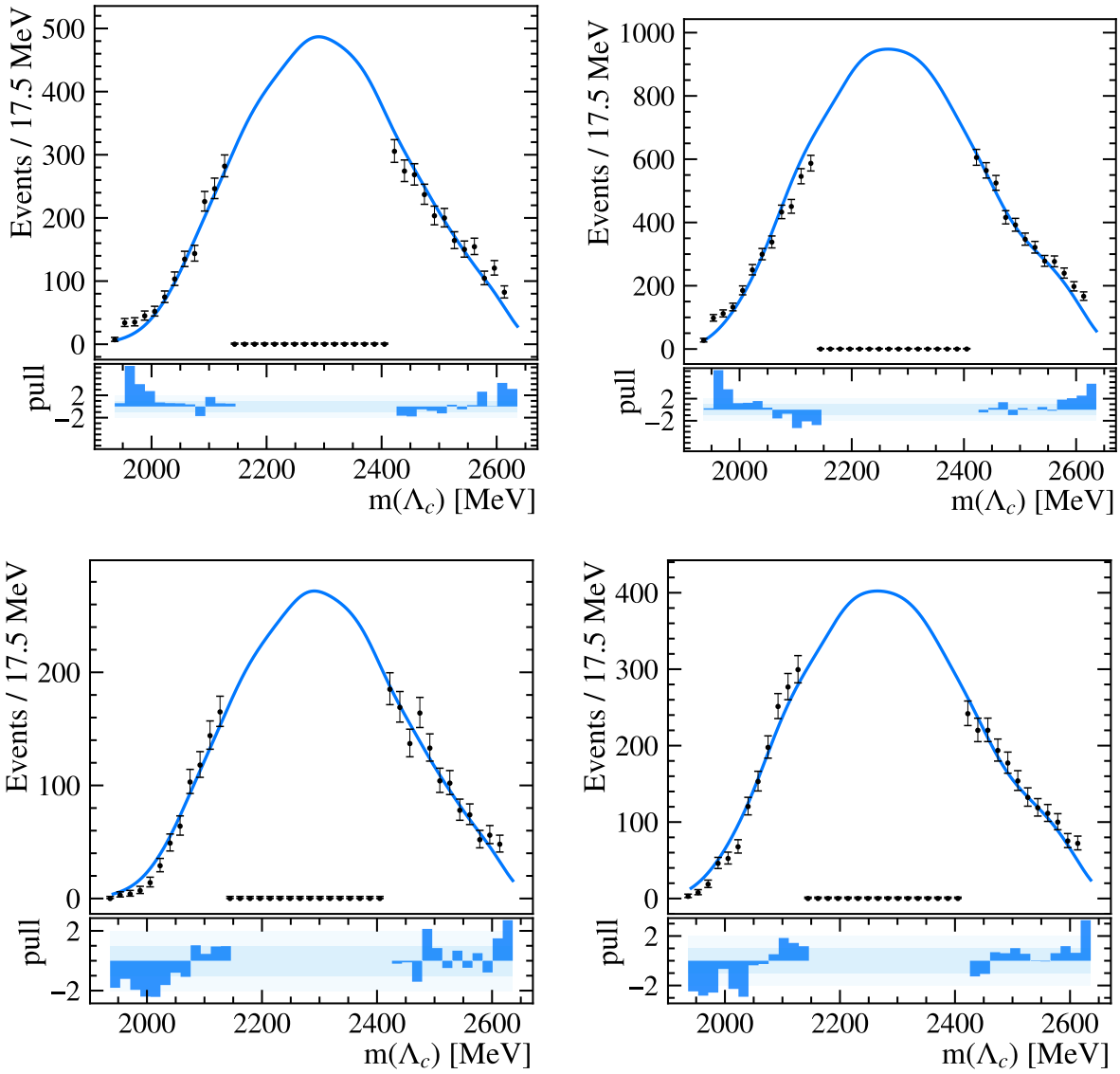

Figure **V-21**: Distribution of $m(\Lambda_c^+)$ sidebands in the signal samples for: (top) SS and (bottom) OS decays and in (left) brem and (right) no-brem categories. Shapes based on the wrong-charge data are superimposed. Additional cut, `e_ProbNNe`> 0.1, is applied to the no-brem samples.

Estimation of combinatorial background yield

An expected yield of the combinatorial background is a key input into the final optimisation performed in the variable space of `e_ProbNNe`, `mu_ProbNNmu` and the XGB2 output (Section **V.12**). For a given set of cuts, this yield can be estimated by applying to the wrong-charge sample the normalisation factor, which is measured as the ratio of the number of events in the sidebands of the signal sample and in the sidebands of the wrong-charge sample.

The number of sideband events (N_{sdb}) in these samples as a function the XGB2 output is shown in Fig. **V-22**. To smooth out statistical fluctuations present in particular for higher XGB2 values, these distributions are modelled. Each XGB2 distribution is fitted with the exponential function, and, as the XGB2 output is within the range of 0 and 1, a sigmoid dumping factor is

also added:

$$N_{sdb}(x) = \left(ae^{-bx} + c\right)\left(\frac{2}{1+e^{d(x-1)}} - 1\right), \tag{V.9}$$

where a, b, c and d are free parameters, and x denotes the XGB2 output. The total number of sideband events, expected for a given XGB2 cut, is obtained by integrating the fitted functions above this cut value.

Figure **V-22** presents the XGB2 distributions for `e_ProbNNe`>0.3 and `mu_ProbNNmu`>0.5. Similar procedure is applied for all combinations of PID criteria considered during the optimisation. This technique helps to achieve more stable optimisation results across the full space of considered requirements.

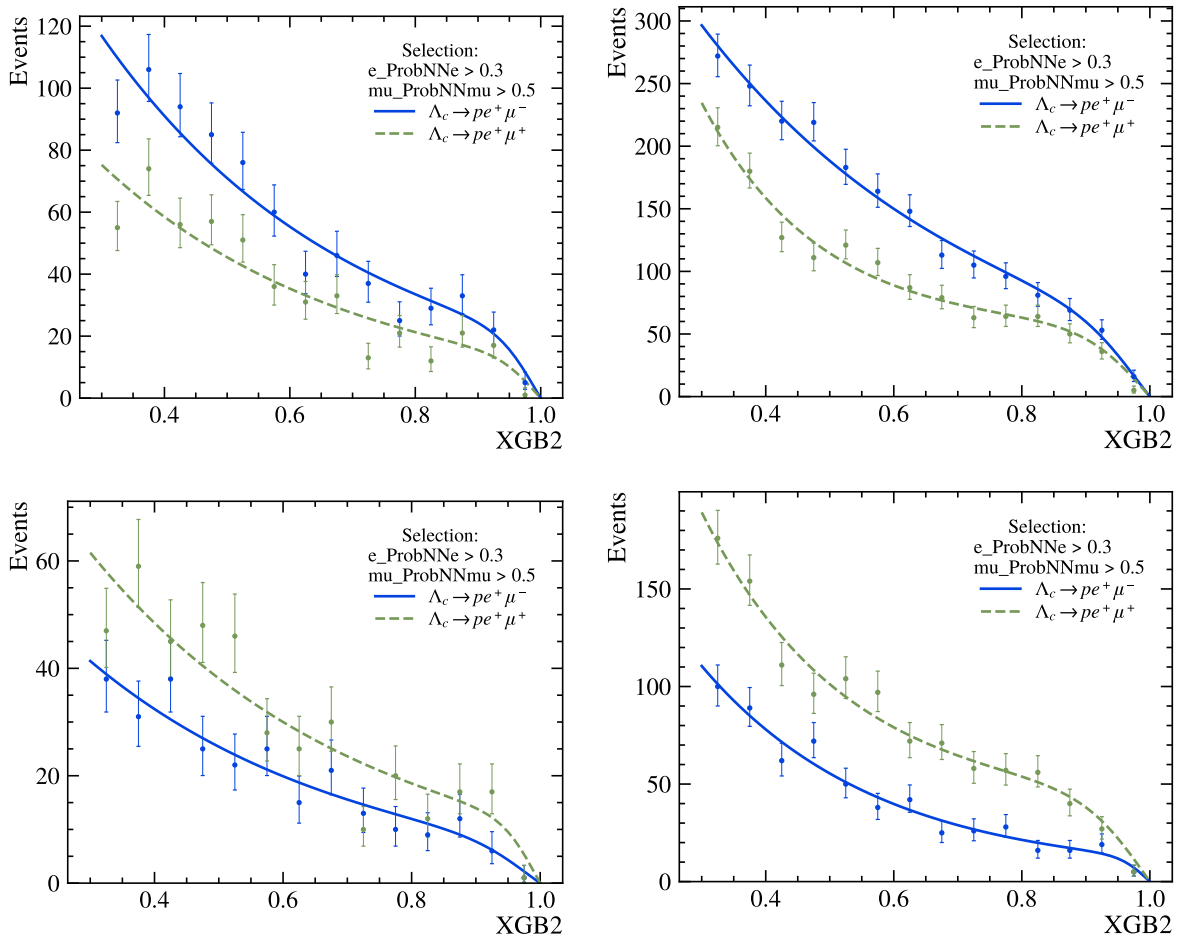

Figure **V-22**: Number of events in the sidebands of (blue) the $\Lambda_c^+ \to pe^\pm\mu^\mp$ signal sample and (green) the wrong-charge sample as a function of XGB2 output for (top) SS and (bottom) OS decays and in (left) brem and (right) no-brem categories. Results of fits are superimposed.

V.10 Formula for signal BFs

The goal of this study is to measure BF of the $\Lambda_c^+ \to pe^\pm\mu^\mp$ decays, or, if no significant signal is observed, to set an UL on this BF. The BF is measured, separately for SS and OS decays, relative

to the BF of the $\Lambda_c^+ \to p\phi$ reference channel, with $\phi \to \mu^+\mu^-$, according to the relation:

$$\mathcal{B}\left(\Lambda_c^+ \to pe^\pm\mu^\mp\right) = \frac{N_{sig}}{N_{ref}} \times \frac{\varepsilon_{ref}}{\varepsilon_{sig}} \times \mathcal{B}\left(\Lambda_c^+ \to p\phi(\to \mu^+\mu^-)\right) \quad \textbf{(V.10)}$$

where $\mathcal{B}$ denotes BF of an indicated decay, N_{sig} and N_{ref} stand for the number of events observed for the signal and reference decay, respectively, whereas ε_{sig} and ε_{ref} are the reconstruction efficiencies of these decays. The yields, efficiencies and, thus, also BFs are calculated separately for the SS $\Lambda_c^+ \to pe^+\mu^-$ and OS $\Lambda_c^+ \to pe^-\mu^+$ decays.

The BF for the reference channel, $\mathcal{B}(\Lambda_c^+ \to p\phi(\to \mu^+\mu^-)) = (3.03 \pm 0.45) \times 10^{-7}$, is the product of $\mathcal{B}(\Lambda_c^+ \to p\phi) = (1.06 \pm 0.14) \times 10^{-3}$ and $\mathcal{B}(\phi \to \mu^+\mu^-) = (2.86 \pm 0.19) \times 10^{-4}$, where both numbers are averages of existing measurements performed in Ref. [19]. Having measured the yields and efficiencies in Eq. **V.10**, one can disentangle BFs (or ULs) for the signal decays. Estimation of the reconstruction efficiencies is based on the simulation samples, and is described in Section **V.11**.

V.10.1 CLs method

The Confidence Levels (CLs) method is a statistical approach for setting an upper limit on the value of a parameter of interest, in our case BF of the $\Lambda_c^+ \to pe^\pm\mu^\mp$ decays. This procedure involves constructing a test statistic q to distinguish between the hypotheses that given data contain signal and background ($s + b$), and that of background only (b). The q is derived from signal and background PDFs, as likelihood ratio:

$$q = -2 \log \frac{\mathcal{L}(s+b)}{\mathcal{L}(b)}. \quad \textbf{(V.11)}$$

As the signal strength can vary, a range of different BFs is studied. For each BF, p-values for $s + b$ and b hypotheses considered (p_{s+b} and p_b) are calculated by integrating the corresponding q distributions.[15] These distributions are obtained from a series of pseudo-experiments based on signal and background PDFs. An example illustrating the p-value calculation is presented in Fig. **V-23**.

The CLs is defined as:

$$\text{CLs} = \frac{p_{s+b}}{1 - p_b}. \quad \textbf{(V.12)}$$

A signal of a given strength is regarded as excluded at CL of $1 - \alpha$, if it gives $CLs < \alpha$. The CLs is essentially a modified p-value that penalizes the $s + b$ hypothesis and prevents the exclusion of signal models in the case of low signal sensitivity, which can occur if q distributions for the two hypotheses are not well separated.

The p-value calculation with pseudo-experiments can be time-consuming and resource-intensive, as it requires generating a new sample for each considered BF. The asymptotic approach, utilised in this thesis, is based on the idea that the median significance of many pseudo-experiments can be obtained by using the Asimov data set, which is defined as a data set in which all observed quantities are equal to their expected values. This assumption can be mathematically proven [77] under some requirements [78], [79]. With this method, one can obtain both, the significance in given data, as well as the simulation-based expected significance distribution for different signal

[15] The p-value of the $s + b$ hypothesis is probability of finding a q value that is equal to the observed q value, or more extreme, assuming that the b-only hypothesis (i.e. null hypothesis) is true.

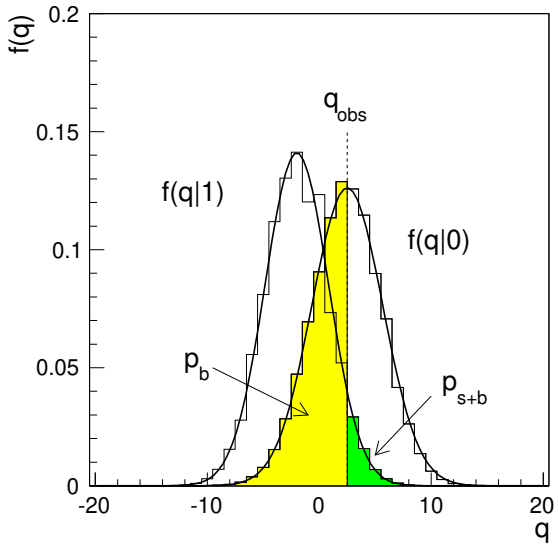

Figure **V-23**: Illustration of p-value calculations for $s + b$ and b-only hypotheses, taken from Ref. [77]. $f(q|\theta)$ is a distribution of the test statistics q for a signal strength θ. Observed q value is denoted with q_{obs}, p_{s+b} and p_b values are marked as green and yellow areas, respectively.

strengths (Section **VI.2**), without using sampling.

V.11 Efficiency estimation

The reconstruction efficiencies for both, signal and reference decays, are necessary for measuring the BF ratio (Eq. **V.10**). Both efficiencies also enter the optimisation procedure, in which the final selection is optimised to give the best ULs (Section **V.12**). The efficiency for a given decay is measured using the corresponding simulation sample as the number of reconstructed and selected decays divided by the number of the generated decays. The simulation samples are corrected as discussed in Section **V.7**. The efficiency estimation is done separately for different data-taking years, magnet polarities and, for the ε_{sig}, independently for the SS and OS categories, and the brem and no-brem cases.

The signal efficiency can be calculated at each consecutive analysis step, which allows for expressing ε_{sig} as:

$$\varepsilon_{sig} = \varepsilon_{gen} \times \varepsilon_{strip} \times \varepsilon_{presel} \times \varepsilon_{Truth} \times \varepsilon_{L0} \times \varepsilon_{Hlt1} \times \varepsilon_{Hlt2} \times \varepsilon_{XGB1} \times \varepsilon_{final}, \qquad \textbf{(V.13)}$$

where ε_{gen} denotes the efficiency of the generator-level cuts (Section **V.2**), ε_{strip} is the efficiency of the stripping selection, ε_{Truth} is the `TruthMatching` efficiency (Section **V.2**), ε_{L0}, ε_{Hlt1} and ε_{Hlt2} are the efficiencies of the trigger selection at the L0, Hlt1 and Hlt2 levels, ε_{presel} denotes the preselection efficiency, ε_{XGB1} the efficiency of the XGB1 cut, whereas ε_{final} is the efficiency of the final selection on the XGB2 output, `e_ProbNNe` and `mu_ProbNNmu`, optimised as discussed in Section **V.12**. In this notation, an efficiency of a given selection step is measured with respect to the previous step. The individual efficiencies contributing to Eq. **V.13** are given in Appendix A.

After the XGB1 selection, and after averaging over the data-taking years and magnet polarities, $\varepsilon_{sig} = 1.16 \times 10^{-4}$ for the SS decays, and $\varepsilon_{sig} = 1.08 \times 10^{-4}$ for the OS decays. These

efficiencies are also averaged for the brem and no-brem samples, whose efficiencies are consistent within uncertainties at this analysis stage.

The ε_{ref} is expressed as in Eq. **V.13**, because the same analysis steps are applied for the reference decay as for the signal decays. After the XGB1 selection, and considering all the data-taking years and magnet polarities, $\varepsilon_{ref} = 3.61 \times 10^{-4}$.

V.11.1 Efficiency and yield of misidentified background

In order to study the misidentified background from $\Lambda_c^+ \to p\pi^+\pi^-$ decays, the $\Lambda_c^+ \to p\pi^+\pi^-$ simulation samples undergo the reconstruction and selection the same as for the signal decays, except for the requirements on the electron and muon PIDs, which are not applied. Instead, the misID rates for $\pi \to e$ and $\pi \to \mu$ are used. They are estimated for given electron and muon PID requirements, as described in Section **V.8.2**. Taking this into account, the efficiency for the misidentified background (ε_{misid}) can be written as:

$$\varepsilon_{misid} = \varepsilon_{gen} \times \varepsilon_{strip}^{\text{noPID}} \times \varepsilon_{presel} \times \varepsilon_{Truth} \times \varepsilon_{L0} \times \varepsilon_{Hlt1} \times \varepsilon_{Hlt2} \times \varepsilon_{XGB1} \times \varepsilon_{final}^{\text{noPID}} \times \varepsilon_{\pi\to e} \times \varepsilon_{\pi\to\mu}, \quad \textbf{(V.14)}$$

where ε_{gen} is specific for the generator-level cuts applied when generating $\Lambda_c^+ \to p\pi^+\pi^-$ decays. `TruthMatching` underlying the ε_{Truth} corresponds to matching the Λ_c^+ candidates to the generated Λ_c^+ baryons, while allowing for the misidentification of the daughter particles. The noPID superscript means that the efficiency for a given selection step has lepton PID requirements removed. The $\varepsilon_{\pi\to e}$ and $\varepsilon_{\pi\to\mu}$ entering Eq. **V.14**, denote the $\pi \to e$ and $\pi \to \mu$ misID rates, respectively. Similar to the ε_{sig}, the ε_{misid} is measured separately for the brem and no-brem samples, and taking into account the efficiency of the brem recovery as a part of the reconstruction.

The L0 selection (Eq. **V.1**) also involves PID information, as it requires the presence of a muon based on hits in Muon Stations (Section **III.2.9**). In Eq. **V.14**, ε_{L0} is assumed to be the same as for the signal, as similar to the PID cuts, the L0 selection cannot be applied for the misidentified simulation sample. This assumption is quite conservative, as ε_{L0} for the decays with pions[16] is smaller than that for the decays involving muons. Similarly, ε_{Hlt1} and ε_{Hlt2} are also substituted by their equivalents measured for the signal decays. These trigger efficiencies are similar to those in the signal decays. Not applying the Hlt1 and Hlt2 trigger selections allows to keep the size of the misidentified simulation sample large enough for the shape estimation, etc.

An expected yield of the misidentified background in the signal samples (N_{misid}) is estimated with respect to the measured yield of the reference decay:

$$N_{misid} = N_{ref} \frac{\mathcal{B}(\Lambda_c^+ \to p\pi^+\pi^-)}{\mathcal{B}(\Lambda_c^+ \to p\phi(\to \mu^+\mu^-))} \frac{\varepsilon_{misid}}{\varepsilon_{ref}} \quad \textbf{(V.15)}$$

where $\mathcal{B}(\Lambda_c^+ \to p\pi^+\pi^-) = (4.60 \pm 0.26) \times 10^{-3}$ is taken from Ref. [19].

After the XGB1 selection, $N_{misid} \simeq 440$ is expected in the SS no-brem sample, $N_{misid} \simeq 466$ in the OS no-brem sample, and $N_{misid} \simeq 16$ in each of the brem samples. Due to the assumption on ε_{L0}, these estimates can be treated as upper limits on the background yields expected in the data.

The efficiency for the misidentified background in the reference decays is expressed similar to Eq. **V.14**, with the individual selection steps corresponding to those applied for the reference channel. The most important difference is in the misID rate contribution, which is $\varepsilon_{\pi\to\mu} \times \varepsilon_{\pi\to\mu}$

[16] Pions that decay in flight via $\pi^+ \to \mu^+\nu_\mu$ within the detector can fire L0Muon.

for the reference decays. N_{misid} for the reference sample is then estimated as in Eq. **V.15**, without considering the brem-related categories.

The final optimization (Section **V.12**) takes into account changes of N_{misid} with the scanned selection requirements. While N_{misid} is fixed in the toy data produced in the optimisation procedure, it is treated as a free parameter in the final fits to the data samples (Section **VI**). This allows to avoid a possible bias on the measured UL due to the assumption on the trigger efficiencies when estimating N_{misid}.

V.12 Optimisation of the final selection

The stripping, trigger, preselection and XGB1 classifier allow for an effective and relatively simple background reduction. The final step of the selection involves requirements on `e_ProbNNe`, `mu_ProbNNmu` and the XGB2 output. The sensitivity of the search for $\Lambda_c^+ \to pe^\pm\mu^\mp$ decays depends on threshold values of these variables. Therefore, the optimisation is performed through scanning these thresholds in a three-dimensional grid, and finding the optimal set of cuts, which gives the best (lowest) UL on $\mathcal{B}(\Lambda_c^+ \to pe^\pm\mu^\mp)$ at 90% CL. The UL is calculated using the CLs method (Section **V.10.1**), and the selection is optimised independently for the four signal categories.

The PDFs for the signal, misidentified background and combinatorial background are based on the $m(\Lambda_c^+)$ shapes, estimated as described in Section **V.9**, and taking into account an impact of the scanned selection thresholds. Some correlations between the mass shapes, in particular for the combinatorial background, and PID requirements are observed for the `e_ProbNNe` and `mu_ProbNNmu` thresholds in the range between 0 and 0.2. For the higher values, these correlations are much less severe, and the shapes do not change significantly. Therefore, to avoid statistical fluctuations, the thresholds are not increased above XGB2>0.5, `e_ProbNNe`>0.3 and `mu_ProbNNmu`>0.3 in modelling the mass shapes.

Toy data are generated based on the mentioned PDFs, and used as an input for the CLs calculations. Other inputs calculated for each combination of cuts are the efficiency for the signal (Eq. **V.13**), the efficiency for the misidentified background (Eq. **V.14**) including the corresponding misID rates (Section **V.8.2**). The expected yield of the misidentified background is then calculated according to Eq. **V.15**. The yield of the combinatorial background is estimated using the approach discussed in Section **V.9.4**. According to Eq. **V.10**, $\mathcal{B}(\Lambda_c^+ \to pe^\pm\mu^\mp)$, and its UL, include also an input from the yield and efficiency of the reference channel, which are also estimated for each set of cuts. For all the signal categories, the same reference sample is considered, with the mass PDF as discussed in Section **V.9.2**. With all these yields and efficiencies set, toy data samples are produced from the input PDFs, and the UL calculation is performed.

A significant effort has been put into tuning the fitting procedure, to make sure that ULs are properly calculated in the whole three-dimensional optimisation space. The fits are sensitive to the amount of the background, both combinatorial and misidentified. The parametrization of the XGB2 distribution for the sideband events (Fig. **V-22**), as well as the fixed expected yield of the misidentified background, substantially improve stability of the fitting. The tools utilised in the fitting toy data and the UL calculations are a part of the scikit-hep project [80], and include the zfit [81], hepstats [82] and mplhep [83] packages.

V.12.1 Optimisation results

The optimisation results for the four signal categories are presented in Figs. **V-24**, **V-25**, **V-26** and **V-27**, showing the calculated UL across the two-dimensional space of `e_ProbNNe` cut vs. XGB2 cut and `mu_ProbNNmu` cut vs. XGB2 cut. In these projections, the optimal cut is applied on the third observable.

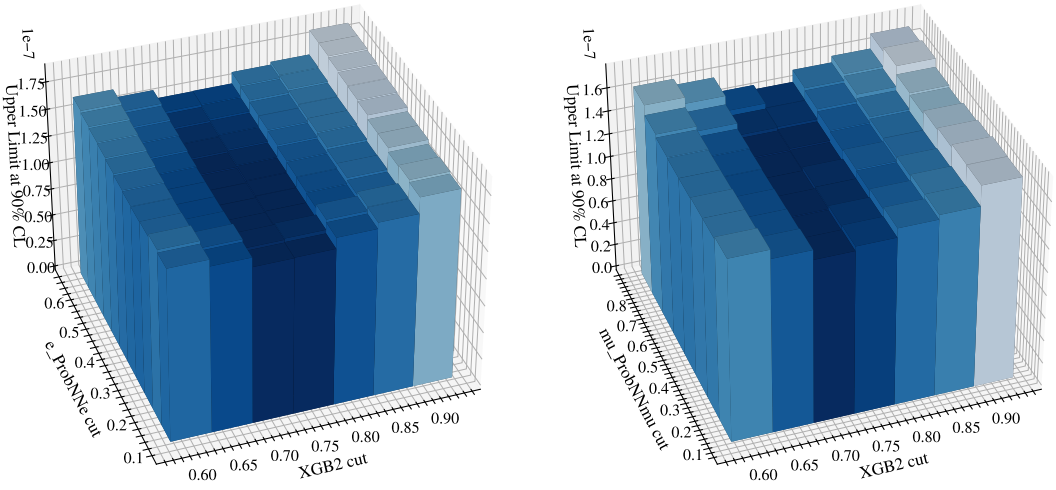

Figure **V-24**: UL on the signal BF at 90% CL, calculated for the SS brem signal category in the final three-dimensional optimisation, and projected onto the two-dimensional space of (left) `e_ProbNNe` cut vs. XGB2 cut and (right) `mu_ProbNNmu` cut vs. XGB2 cut.

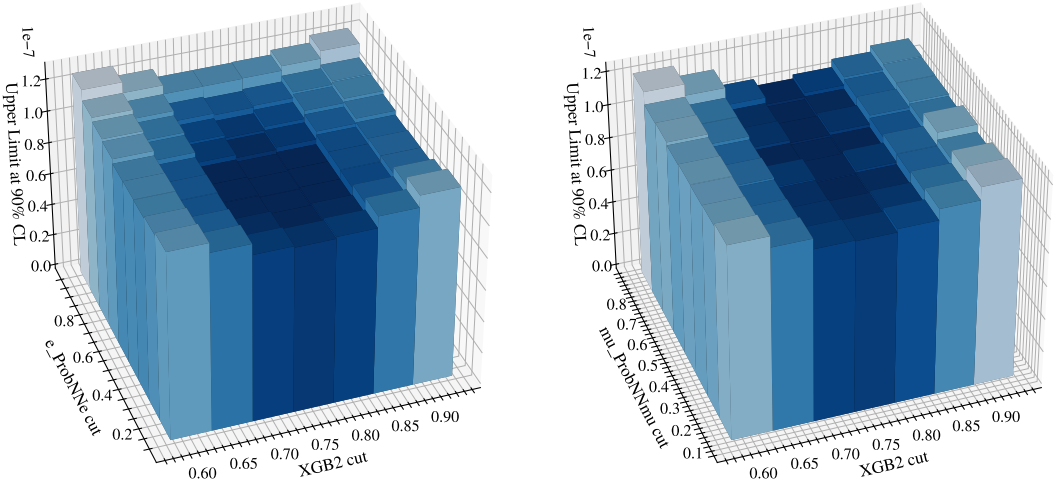

Figure **V-25**: UL on the signal BF at 90% CL, calculated for the SS no-brem signal category in the final three-dimensional optimisation, and projected onto the two-dimensional space of (left) `e_ProbNNe` cut vs. XGB2 cut and (right) `mu_ProbNNmu` cut vs. XGB2 cut.

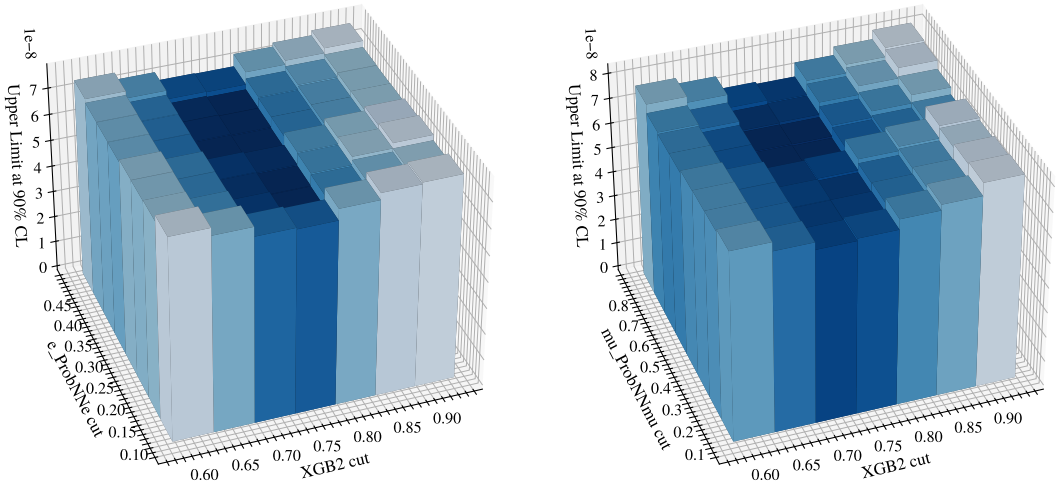

Figure **V-26**: UL on the signal BF at 90% CL, calculated for the OS brem signal category in the final three-dimensional optimisation, and projected onto the two-dimensional space of (left) `e_ProbNNe` cut vs. XGB2 cut and (right) `mu_ProbNNmu` cut vs. XGB2 cut.

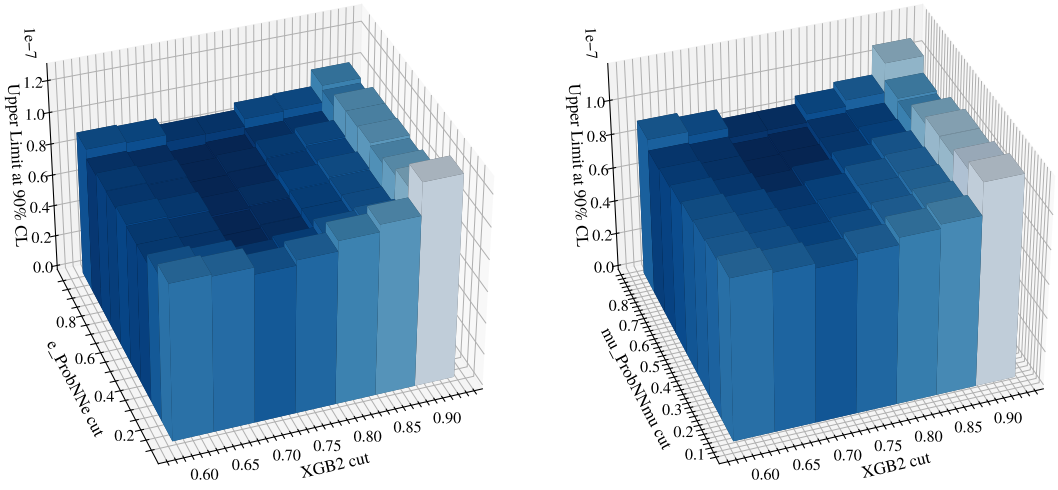

Figure **V-27**: UL on the signal BF at 90% CL, calculated for the OS no-brem signal category in the final three-dimensional optimisation, and projected onto the two-dimensional space of (left) `e_ProbNNe` cut vs. XGB2 cut and (right) `mu_ProbNNmu` cut vs. XGB2 cut.

The ULs are quite strongly dependent on the XGB2 cut, with the minimum located between 0.70 and 0.75 for all the signal categories. The dependence on the PID cuts is less pronounced. The optimal requirements selected for each signal category, the signal reconstruction/selection efficiency, and the expected ULs at 90% CL, are presented in Table **V-10**. Examples of the toy data produced with the optimal selection, along with the fit results, are shown in Fig. **V-28**.

Signal category	XGB2 output	`e_ProbNNe`	`mu_ProbNNmu`	ε_{sig} $[10^{-5}]$	Expected UL at 90%CL
SS brem	> 0.70	> 0.25	> 0.50	6.76 ± 0.52	1.4×10^{-7}
SS no-brem	> 0.75	> 0.30	> 0.50	6.10 ± 0.41	1.0×10^{-7}
OS brem	> 0.75	> 0.30	> 0.50	5.51 ± 0.46	6.7×10^{-8}
OS no-brem	> 0.70	> 0.80	> 0.70	4.79 ± 0.35	8.0×10^{-8}

Table **V-10**: The optimal cuts selected for each $\Lambda_c^+ \to pe^\pm\mu^\mp$ signal category, the signal reconstruction/selection efficiency, and expected UL on the signal BF at 90% CL.

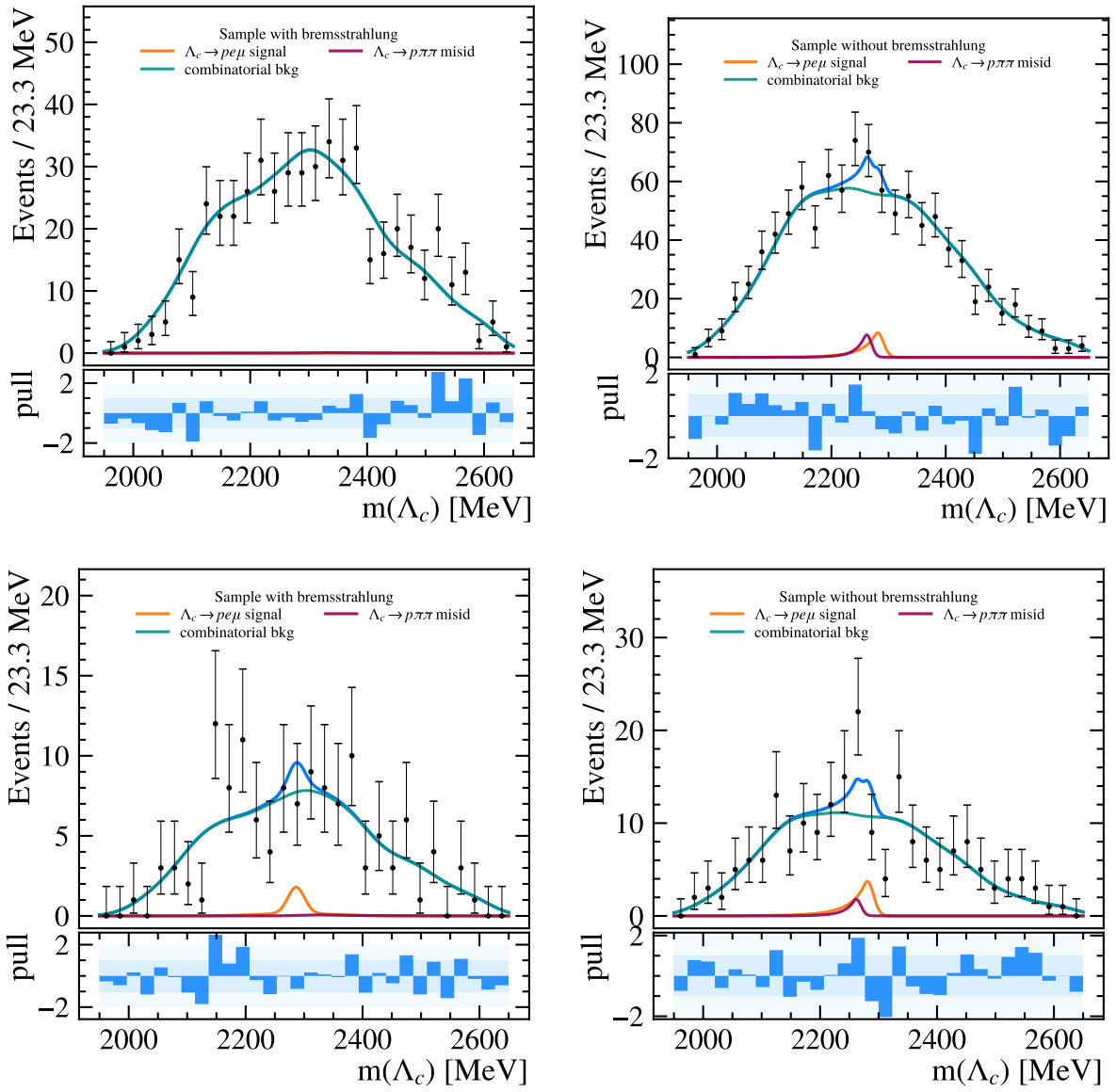

Figure **V-28**: Toy data for $m(\Lambda_c^+)$ distributions selected with the optimal cuts, with the fit results superimposed, for (top) SS and (bottom) OS signal categories, (left) brem and (right) no-brem samples. Signal component is shown in orange, misidentified background in red, and combinatorial background in green.

V.12.2 Mass shapes after the final selection

After the final selection, the shapes of the Λ_c^+ mass distributions for the signal and reference decays, as well as for the misidentified background, have not changed significantly compared to those measured after the XGB1 selection (Section **V.9.1**). The most significant change is found in the combinatorial-background shape, in particular for the no-brem sample, which after the final selection becomes more uniform in the signal region. The KDE method, used for modelling the wrong-charge samples, is adapting well to these changes. The wrong-charge data samples, with the optimal cuts applied, are presented, together with the fits, in Fig. **V-29**.

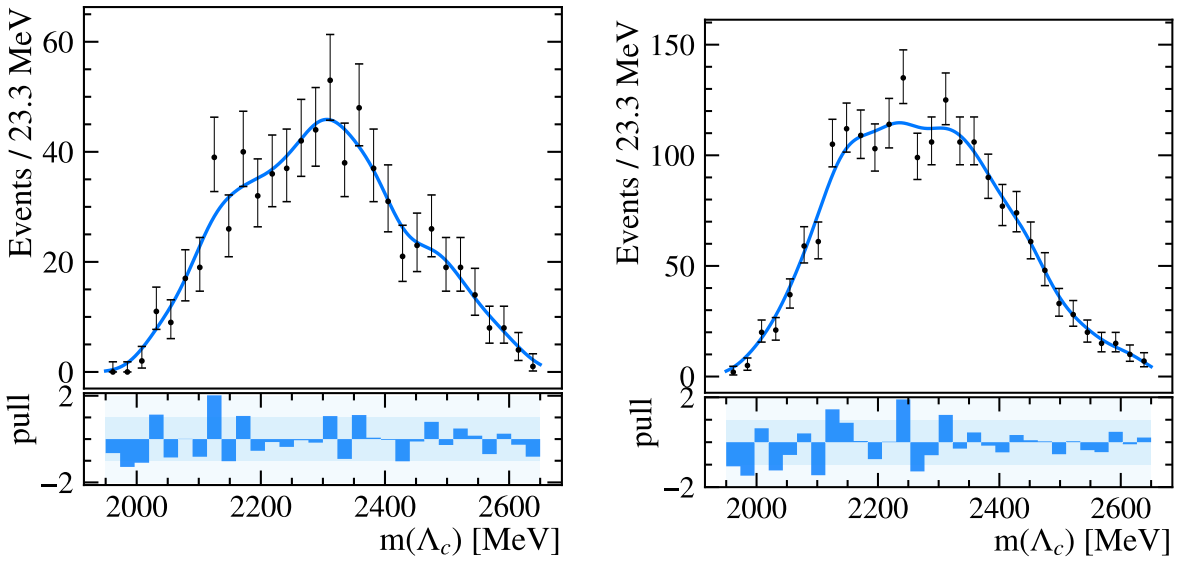

Figure **V-29**: Distribution of $m(\Lambda_c^+)$ for the wrong-charge data, selected with the optimal cuts, for (left) brem and (right) no-brem samples. Shapes approximated with the KDE method are superimposed.

V.13 Systematic uncertainties

Although the optimisation is performed independently for the four signal categories, the brem and no-brem data samples are fitted simultaneously in order to calculate the ULs for the SS and OS signal decays (Section **VI.2**). The systematic uncertainties taken into account in the determination of these ULs are summarised in Table **V-11**.

The largest systematic uncertainty, originates from the $\mathcal{B}(\Lambda_c^+ \to p\phi(\to \mu^+\mu^-))$ value, which is measured with 14.8% uncertainty [19]. As this analysis relies on the BF of the reference decay, it is the external uncertainty that cannot be mitigated.

The primary contributions from the presented analysis itself are: the statistical uncertainty of the $\varepsilon_{ref}/\varepsilon_{sig}$ efficiency ratio, driven by the size of the simulation samples, and the statistical uncertainty on the reference channel yield. The latter is measured in the fit performed to the $\Lambda_c^+ \to p\phi$ data sample after the final selection (Section **VI.1**). These two uncertainties are directly dependent on the final selection, so they differ between the four signal categories. Other uncertainties are evaluated by examining how modifications to the fit models affect the calculated BFs. These contributions are common for the brem and no-brem categories, as they are fitted

simultaneously. The estimation of these uncertainties is performed using a simultaneous fit to toy data samples.

Source	Uncertainty [%]			
	SS		OS	
	brem	no-brem	brem	no-brem
BF of reference decay (external)	14.8			
Efficiency ratio	7.6	6.7	7.9	7.3
Reference yield	5.6	6.5	6.5	6.0
Shape of signal	3.6		4.7	
KDE kernel size	0.70		1.0	
Shape of combinatorial	0.68		0.29	
Selection	0.57		0.49	
Fit bias	0.10		0.10	
Total (internal)	10.6	10.1	11.6	10.6
Total	18.2	17.9	18.8	18.3

Table **V-11**: Summary of systematic uncertainties on signal BF for each signal category.

The uncertainty related to the signal shape is calculated by changing the default signal PDFs (Section **V.9.1**) to a Johnson function [84], defined as:

$$f(m; s, t, m_0, \sigma) = \frac{t}{\sigma\sqrt{2\pi\left(1 + \left(\frac{m-m_0}{\sigma}\right)^2\right)}} \exp\left(-\frac{1}{2}\left[s + t \cdot arcsinh\left(\frac{m-m_0}{\sigma}\right)\right]^2\right), \quad \textbf{(V.16)}$$

where s is interpreted as a distribution skewness, t denotes tail weight, m_0 is peak position and σ represents width. The fits to the simulated signal samples performed with this alternative model are presented in Fig. **V-30**. The relative difference in the BFs measured with the default and alternative signal PDFs is taken as the systematic uncertainty. As toy data may introduce statistical fluctuations, the sampling and fitting are repeated till the average BFs are stable with respect to the measured differences.

The uncertainty related to the combinatorial background originates from the background shape, and the chosen kernel in the KDE method. In the default fit, both $pe^-\mu^-$ and $pe^+\mu^+$ combinations contribute to the wrong-charge sample (Section **V.9.4**). To obtain an alternative shape, only the $pe^-\mu^-$ data are used. The kernel, in the context of the KDE method, is a contribution to the PDF from a single decay candidate, described with a Gaussian function. To check an impact of changing the kernel, the Gaussian width is reduced from 30 MeV to 25 MeV.

Although the simulation samples are calibrated/corrected as much as possible, there still can be some differences between data and MC, for instance in the isolation variables. They could lead to data-MC difference in the XGB2 output, and result in a possible bias in the efficiency of the final selection. To account for this, the measurement is performed with the final selection slightly

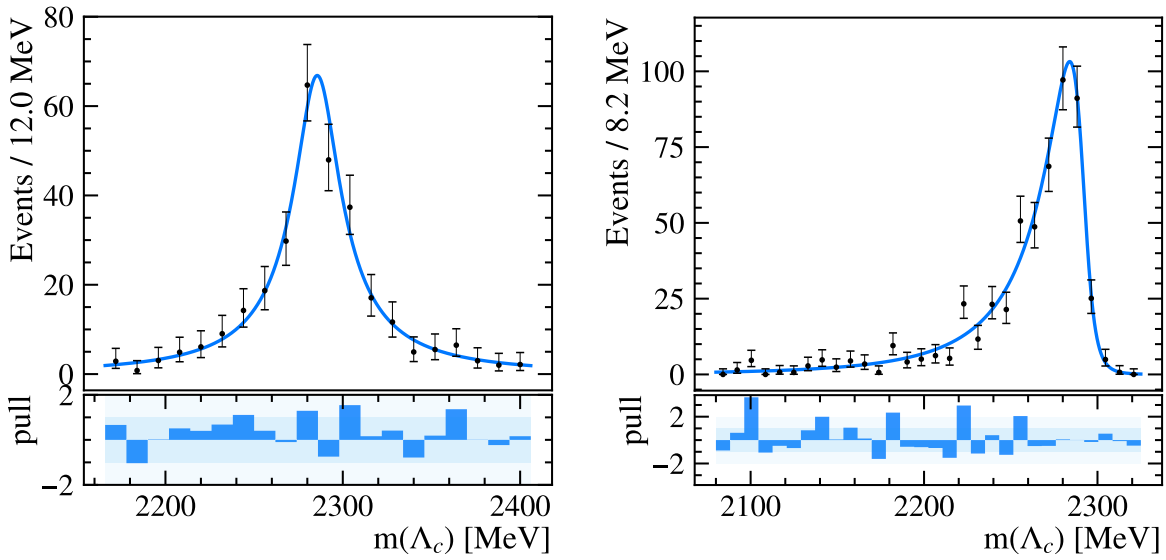

Figure **V-30**: Distribution of $m(\Lambda_c^+)$ for the signal simulation fitted with Johnson function for (left) brem and (right) no-brem sample.

changed. This is a conservative approach, as in principle, related systematic uncertainties are expected to largely cancel in the efficiency ratio of the signal decays and the reference channel.

The bias due to the fitting procedure is determined using toy data based on the measured distributions and with the signal artificially injected, assuming $\mathcal{B}(\Lambda_c^+ \to pe^{\pm}\mu^{\mp}) = 1{\times}10^{-7}$. These data are sampled and fitted in series of pseudo-experiments. The residual difference between the injected BF value and the values measured in the pseudo-experiments is taken as the systematic uncertainty.

The total systematic uncertainty ranges from 17.9% to 18.8%, depending on the signal category, with the highest contribution coming from the BF of the reference channel.

Chapter VI

Results

VI.1 Reference channel

The number of decays measured for the reference channel, $\Lambda_c^+ \to p\phi$, with $\phi \to \mu^+\mu^-$, is explicitly used in measuring BFs of the signal channels (Eq. **V.10**). As the optimal cuts (Table **V-10**) differ between the different signal categories, N_{ref} is measured for them separately. The corresponding optimal selection is applied to the reference sample; the `mu_ProbNNmu` cut is used for both final-state muons. The resulting $m(\Lambda_c^+)$ distributions are then fitted to extract N_{ref}.

After the final selection, the $\Lambda_c^+ \to p\phi$ signal retains similar $m(\Lambda_c^+)$ shape as after the pre-selection (Section **V.6.1**). Thus, the same PDF as in Section **V.9.2** is used to model the signal, with the parameters fixed and the yield kept free. Similar applies to the misidentified background PDF (Fig. **V-19**). Its parameters are also fixed to those measured in the simulations, and the yield is free. The main difference comes from the level of the combinatorial background, which is significantly reduced. It is described with a first-order polynomial. The $m(\Lambda_c^+)$ distributions, along with the fit results, are shown in Fig. **VI-1** for the selections corresponding to each signal category. The same reference sample, and thus also N_{ref}, are relevant for the SS no-brem and OS brem signal categories, as they have the same optimal cuts.

The reference channel yields are: 367 ± 24 events for the SS brem final selection, 320 ± 19 for the SS no-brem and OS brem cuts, and 331 ± 21 for the OS no-brem cuts. The corresponding yields of the misidentified background are: 18 ± 13, 20.5 ± 9.7 and 13.5 ± 8.9.

VI.2 Upper limits for signal decays

To measure ULs on the BFs of the signal decays, the $m(\Lambda_c^+)$ distributions measured in the data are unblinded, and fitted with the method similar to that applied for toy data in Fig. **V-28**. The fit components are the signal, the misidentified background and the combinatorial background, and their PDFs are as described in Sections **V.9.1**, **V.9.3** and **V.9.4**. All the shape parameters in these PDFs are fixed to those in the simulations or, in the case of the combinatorial background, to the wrong-charge data, measured after the final selection. The yield of each component is treated as a free parameter in the fit. The efficiencies for the signal and reference decays, the reference channel yield and BF, needed for measuring the signal BFs (Eq. **V.10**) are fixed. The fit is performed simultaneously for the brem and no-brem samples, and independently for the

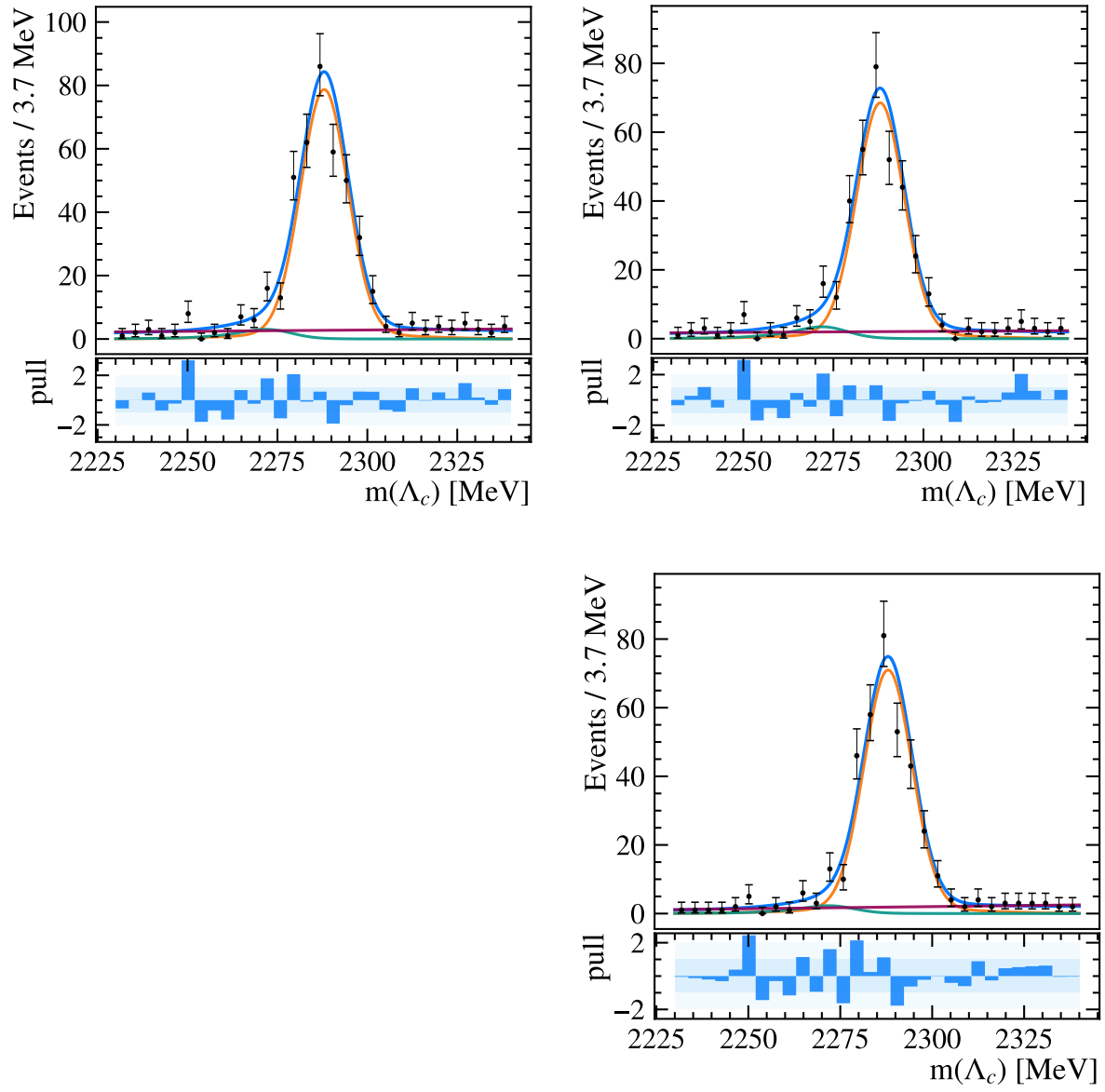

Figure **VI-1**: Distribution of $m(\Lambda_c^+)$ for $\Lambda_c^+ \to p\phi$ sample after the optimal selection aligned with (top left) SS brem, (top right) SS no-brem and OS brem, (bottom right) OS no-brem signal categories. The fit results are superimposed, with (orange) $\Lambda_c^+ \to p\phi$ signal, (green) misidentified background from $\Lambda_c^+ \to p\pi^+\pi^-$ decays, and (red) combinatorial background contributions.

SS and OS categories. The BFs are measured for the OS and SS signal decays. The systematic uncertainties on the signal BFs (Section **V.13**) are included in calculating the ULs. Figures **VI-2** and **VI-3** present the distributions with the fit results for the OS and OS samples, respectively.

The shape of the combinatorial background, obtained from the data with wrong-charge combinations, matches the observed background in the signal region quite well for all the data samples. The observed misidentified background yield (Table **VI-1**) is, within its statistical uncertainty, consistent with the expected yield based on the misID rates (Section **V.11.1**). For the OS no-brem sample, the misidentified background exhibits an upward fluctuation.

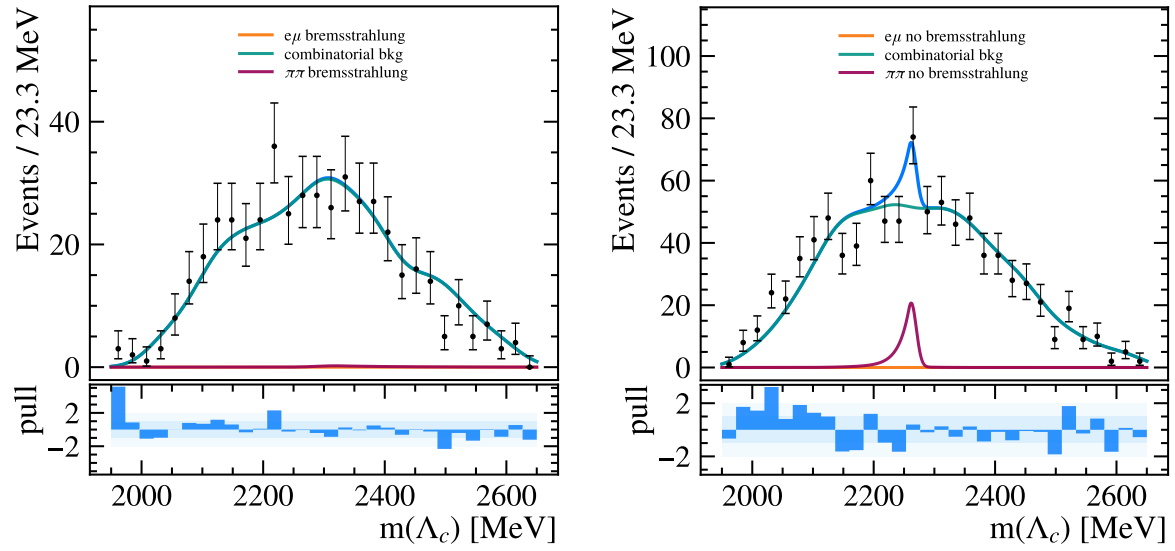

Figure **VI-2**: Distribution of $m(\Lambda_c^+)$ for the SS signal category and (left) brem and (right) no-brem sample, with the results of simultaneous fit superimposed. Signal component is shown in orange, misidentified background in red, and combinatorial background in green.

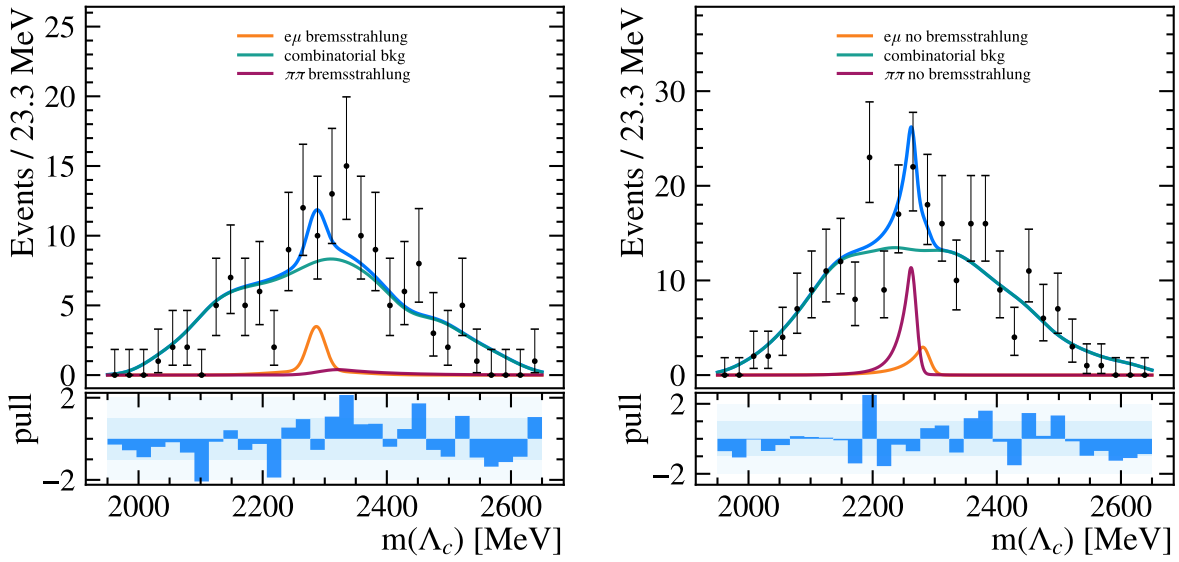

Figure **VI-3**: Distribution of $m(\Lambda_c^+)$ for the OS signal category and (left) brem and (right) no-brem sample, with the results of simultaneous fit superimposed. Signal component is shown in orange, misidentified background in red, and combinatorial background in green.

The measured signal yields are $5.1^{+5.5}_{-5.1}$ for the SS brem sample, $9.1^{+6.6}_{-9.1}$ for the SS no-brem sample, $0.0^{+5.3}_{-0.0}$ for the OS brem sample and $0.0^{+8.2}_{-0.0}$ for the OS no-brem sample. Neither of them is significant. The corresponding ULs, measured with the CLs method (Section **V.10.1**), are:

$$\begin{aligned} \mathcal{B}(\Lambda_c^+ \to p e^+ \mu^-) &< 7.73 \times 10^{-8} \text{ at } 90\% \text{ CL}, \\ \mathcal{B}(\Lambda_c^+ \to p e^- \mu^+) &< 9.48 \times 10^{-8} \text{ at } 90\% \text{ CL}. \end{aligned} \quad \textbf{(VI.1)}$$

Sample	Expected yield	Observed yield
SS brem	0.93	1.23 ± 0.60
SS no-brem	20.5	28.1 ± 13.1
OS brem	0.66	2.15 ± 1.16
OS no-brem	4.79	15.5 ± 8.38

Table **VI-1**: The observed and expected misidentified background yields.

The observed and expected CLs distributions, as functions of the assumed signal BF, are shown in Fig. **VI-4**. The expected CLs values are obtained using the asymptotic approach (Section **V.10.1**), and are the expected limits under the assumption of no signal.

The observed ULs are consistent with the expectations within 1σ for the SS decays, and within 2σ for the OS decays. The measured ULs improve those set by BaBar (Eq. **II.7**) by about two orders of magnitude. At the same time, they comprise one of the most sensitive searches performed so far in charm sector(Table **II-1**).

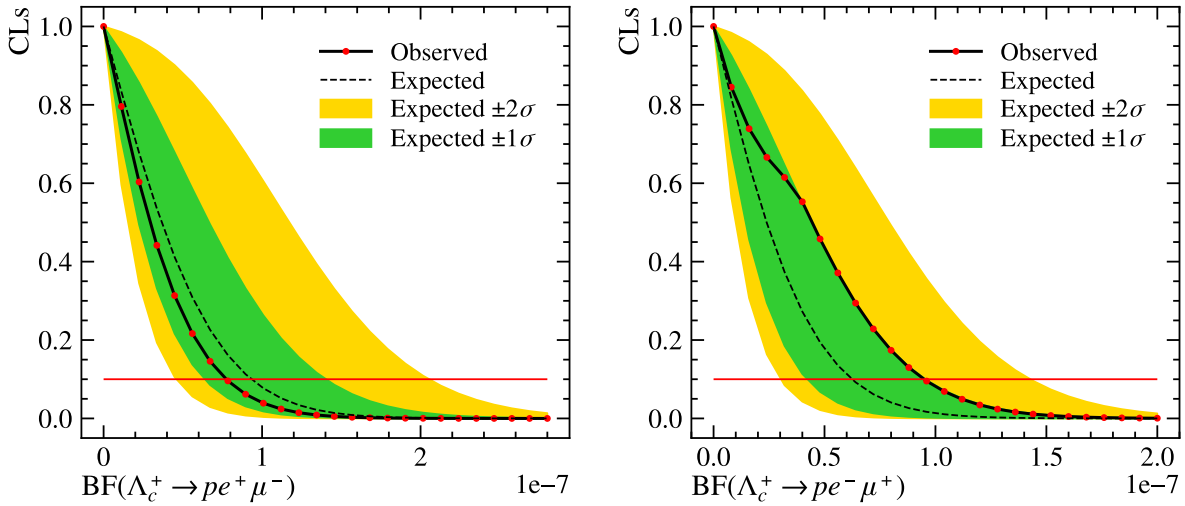

Figure **VI-4**: Distribution of CLs as a function of (left) $\mathcal{B}(\Lambda_c^+ \to pe^+\mu^-)$ and (right) $\mathcal{B}(\Lambda_c^+ \to pe^-\mu^+)$. Central values of the expected CLs for the background-only hypothesis, are shown by dashed line, with confidence intervals corresponding to (green) $\pm 1\sigma$ and (yellow) $\pm 2\sigma$. The observed CLs distribution is shown by solid black line connecting (red) data points. The observed UL at 90% CL is set at the BF value for which the 90% CL (red) horizontal line crosses the observed CLs distribution.

Chapter VII

Summary and outlook

This thesis presents the search for the lepton-flavour violating decays, $\Lambda_c^+ \to pe^+\mu^-$ and $\Lambda_c^+ \to pe^-\mu^+$, and their charge conjugates. It is performed using 5.4 fb^{-1} of the pp collision data collected at the centre-of-mass energy of 13 TeV by the LHCb experiment. These decays are effectively forbidden within the SM. Therefore, finding any significant $\Lambda_c^+ \to pe^\pm\mu^\mp$ signal would be a clear sign of BSM effects.

The primary challenge in this study lies in identifying and suppressing background. The dominant background stems from frequent $\Lambda_c^+ \to p\pi^+\pi^-$ decays, with pions misidentified as leptons, and from random $pe^\pm\mu^\mp$ combinations. Multivariate classification models based on kinematical, topological and PID observables are employed to reduce these backgrounds. Signal decays are identified with the reconstructed mass of the Λ_c^+ candidates. The selection efficiencies for the signal and misidentified decays are determined using the calibrated simulations. Expected yields and shapes of the combinatorial background are estimated through fitting the data in the $m(\Lambda_c^+)$ sidebands, as well as the wrong-charge data. The decay $\Lambda_c^+ \to p\phi$, followed by $\phi \to \mu^+\mu^-$, is chosen as the reference channel, with respect to which the signal BFs are measured.

Selection requirements on the multivariate classifier output and electron and muon PID observables are optimised to provide the best i.e. lowest ULs on $\mathcal{B}(\Lambda_c^+ \to pe^\pm\mu^\mp)$ at 90% CL. The ULs are calculated using the CLs method. To avoid any experimental bias, the analysis is conducted with the $m(\Lambda_c^+)$ signal region blinded until the methods have been established and the final selection optimised. No significant signal has been observed, and the ULs at 90% CL are set as:

$$\mathcal{B}(\Lambda_c^+ \to pe^+\mu^-) < 7.73 \times 10^{-8},$$
$$\mathcal{B}(\Lambda_c^+ \to pe^-\mu^+) < 9.48 \times 10^{-8}.$$

Both, statistical and systematic uncertainties are considered in these limits. The statistical uncertainty is dominant one, while the largest systematic contribution comes from the BF of the reference channel. This analysis, as well as many other charm measurements, would certainly benefit from improved measurement of $\mathcal{B}(\Lambda_c^+ \to p\phi)$.

The ULs measured in this thesis comprise a significant improvement compared to the previous limits from the BaBar experiment, $\mathcal{B}(\Lambda_c^+ \to pe^+\mu^-) < 9.9 \times 10^{-6}$ and $\mathcal{B}(\Lambda_c^+ \to pe^-\mu^+) < 1.9 \times 10^{-5}$ [29]. The presented study is one of the most sensitive BSM searches performed so far in charm sector.

The improvement achieved in the presented analysis can be primarily attributed to the large

LHCb data sample collected during Run-2. Further advancement is expected with the data from the ongoing Run-3, in which the 50 fb^{-1} data sample is planned to be accumulated by 2027. However, the increase of the instantaneous luminosity in Run-3 is likely to result in a higher background, while the purely software trigger introduced will bring new challenges into the HLT1 and HLT2 selections. Looking further ahead, the LHCb experiment is actively preparing for its Upgrade II, within which Magnet Stations are planned to improve the reconstruction of low-momentum particles. This subdetector will increase sensitivities of many charm studies, including future searches for $\Lambda_c^+ \to p e^\pm \mu^\mp$ decays. The contribution into the development of Magnet Stations, presented within this thesis, will help to reach expected goals.

Appendix A

Efficiency table

Sample name	ε_{gen}	ε_{strip}	ε_{truth}	ε_{presel}	ε_{L0}	ε_{Hlt1}	ε_{Hlt2}	ε_{XGB1}	ε_{tot}	$un(\varepsilon_{tot})$
Lc2pemu_MC_2016_MagDown_osign_Brem	0.154	0.0065	0.814	0.888	0.268	0.932	0.222	0.801	3.94E-05	8.44E-06
Lc2pemu_MC_2016_MagDown_ssign_Brem	0.154	0.0070	0.811	0.918	0.257	0.906	0.208	0.917	4.40E-05	9.07E-06
Lc2pemu_MC_2016_MagUp_osign_Brem	0.154	0.0069	0.813	0.898	0.255	0.873	0.237	0.889	4.48E-05	9.06E-06
Lc2pemu_MC_2016_MagUp_ssign_Brem	0.154	0.0071	0.776	0.895	0.258	0.893	0.171	0.825	3.15E-05	7.54E-06
Lc2pemu_MC_2017_MagDown_osign_Brem	0.154	0.0074	0.819	0.909	0.355	0.875	0.604	0.804	1.56E-04	1.74E-05
Lc2pemu_MC_2017_MagDown_ssign_Brem	0.154	0.0073	0.827	0.919	0.307	0.916	0.536	0.834	1.30E-04	1.57E-05
Lc2pemu_MC_2017_MagUp_osign_Brem	0.154	0.0072	0.822	0.897	0.323	0.833	0.641	0.864	1.47E-04	1.71E-05
Lc2pemu_MC_2017_MagUp_ssign_Brem	0.154	0.0073	0.821	0.920	0.321	0.893	0.641	0.868	1.65E-04	1.81E-05
Lc2pemu_MC_2018_MagDown_osign_Brem	0.154	0.0079	0.811	0.905	0.264	0.856	0.619	0.865	1.32E-04	1.65E-05
Lc2pemu_MC_2018_MagDown_ssign_Brem	0.154	0.0077	0.848	0.910	0.298	0.939	0.651	0.840	1.66E-04	1.86E-05
Lc2pemu_MC_2018_MagUp_osign_Brem	0.154	0.0079	0.824	0.908	0.284	0.884	0.604	0.811	1.35E-04	1.65E-05
Lc2pemu_MC_2018_MagUp_ssign_Brem	0.154	0.0079	0.818	0.924	0.292	0.903	0.633	0.867	1.62E-04	1.82E-05
Lc2ppipi_MC_2016_MagDown_osign_Brem	0.079	0.0205	0.309	0.901				0.825	6.73E-05	
Lc2ppipi_MC_2016_MagDown_ssign_Brem	0.079	0.0201	0.354	0.912				0.789	5.58E-05	
Lc2ppipi_MC_2016_MagUp_osign_Brem	0.079	0.0207	0.347	0.893				0.799	6.18E-05	
Lc2ppipi_MC_2016_MagUp_ssign_Brem	0.079	0.0201	0.330	0.908				0.795	4.54E-05	
Lc2ppipi_MC_2017_MagDown_osign_Brem	0.079	0.0196	0.258	0.885				0.800	2.07E-04	
Lc2ppipi_MC_2017_MagDown_ssign_Brem	0.079	0.0187	0.209	0.892				0.803	1.60E-04	
Lc2ppipi_MC_2017_MagUp_osign_Brem	0.079	0.0193	0.304	0.893				0.822	1.94E-04	
Lc2ppipi_MC_2017_MagUp_ssign_Brem	0.079	0.0208	0.329	0.879				0.778	2.07E-04	
Lc2ppipi_MC_2018_MagDown_osign_Brem	0.079	0.0211	0.265	0.897				0.764	1.61E-04	
Lc2ppipi_MC_2018_MagDown_ssign_Brem	0.079	0.0238	0.344	0.924				0.787	2.50E-04	
Lc2ppipi_MC_2018_MagUp_osign_Brem	0.079	0.0205	0.312	0.890				0.813	1.79E-04	
Lc2ppipi_MC_2018_MagUp_ssign_Brem	0.079	0.0217	0.322	0.930				0.813	2.17E-04	

Sample name	ε_{gen}	ε_{strip}	ε_{truth}	ε_{presel}	ε_{L0}	ε_{Hlt1}	ε_{Hlt2}	ε_{XGB1}	ε_{tot}	$un(\varepsilon_{tot})$
Lc2pemu_MC_2016_MagDown_osign_noBrem	0.154	0.0070	0.829	0.912	0.259	0.900	0.231	0.872	4.57E-05	7.02E-06
Lc2pemu_MC_2016_MagDown_ssign_noBrem	0.154	0.0065	0.806	0.908	0.269	0.897	0.228	0.889	4.40E-05	6.84E-06
Lc2pemu_MC_2016_MagUp_osign_noBrem	0.154	0.0071	0.833	0.904	0.236	0.875	0.206	0.830	3.45E-05	6.08E-06
Lc2pemu_MC_2016_MagUp_ssign_noBrem	0.154	0.0070	0.824	0.914	0.250	0.886	0.211	0.872	4.02E-05	6.57E-06
Lc2pemu_MC_2017_MagDown_osign_noBrem	0.154	0.0071	0.819	0.891	0.351	0.908	0.584	0.862	1.56E-04	1.42E-05
Lc2pemu_MC_2017_MagDown_ssign_noBrem	0.154	0.0077	0.828	0.908	0.334	0.883	0.634	0.864	1.72E-04	1.50E-05
Lc2pemu_MC_2017_MagUp_osign_noBrem	0.154	0.0073	0.829	0.919	0.332	0.862	0.569	0.814	1.36E-04	1.31E-05
Lc2pemu_MC_2017_MagUp_ssign_noBrem	0.154	0.0072	0.819	0.898	0.362	0.855	0.574	0.824	1.45E-04	1.36E-05
Lc2pemu_MC_2018_MagDown_osign_noBrem	0.154	0.0075	0.817	0.902	0.251	0.917	0.636	0.887	1.35E-04	1.35E-05
Lc2pemu_MC_2018_MagDown_ssign_noBrem	0.154	0.0082	0.824	0.905	0.280	0.917	0.587	0.897	1.53E-04	1.45E-05
Lc2pemu_MC_2018_MagUp_osign_noBrem	0.154	0.0081	0.835	0.885	0.279	0.879	0.581	0.860	1.35E-04	1.35E-05
Lc2pemu_MC_2018_MagUp_ssign_noBrem	0.154	0.0076	0.800	0.918	0.291	0.906	0.581	0.869	1.42E-04	1.39E-05
Lc2ppipi_MC_2016_MagDown_osign_noBrem	0.079	0.0204	0.554	0.916				0.845	6.75E-05	
Lc2ppipi_MC_2016_MagDown_ssign_noBrem	0.079	0.0204	0.554	0.918				0.846	6.95E-05	
Lc2ppipi_MC_2016_MagUp_osign_noBrem	0.079	0.0203	0.572	0.925				0.854	5.40E-05	
Lc2ppipi_MC_2016_MagUp_ssign_noBrem	0.079	0.0203	0.573	0.919				0.851	5.89E-05	
Lc2ppipi_MC_2017_MagDown_osign_noBrem	0.079	0.0196	0.505	0.924				0.850	2.28E-04	
Lc2ppipi_MC_2017_MagDown_ssign_noBrem	0.079	0.0196	0.506	0.926				0.852	2.30E-04	
Lc2ppipi_MC_2017_MagUp_osign_noBrem	0.079	0.0196	0.547	0.921				0.850	1.98E-04	
Lc2ppipi_MC_2017_MagUp_ssign_noBrem	0.079	0.0195	0.543	0.925				0.851	2.17E-04	
Lc2ppipi_MC_2018_MagDown_osign_noBrem	0.079	0.0218	0.557	0.926				0.853	2.01E-04	
Lc2ppipi_MC_2018_MagDown_ssign_noBrem	0.079	0.0217	0.549	0.926				0.847	2.04E-04	
Lc2ppipi_MC_2018_MagUp_osign_noBrem	0.079	0.0217	0.580	0.926				0.852	1.94E-04	
Lc2ppipi_MC_2018_MagUp_ssign_noBrem	0.079	0.0217	0.577	0.925				0.854	2.09E-04	

Sample name	ε_{gen}	ε_{strip}	ε_{truth}	ε_{presel}	ε_{L0}	ε_{Hlt1}	ε_{Hlt2}	ε_{XGB1}	ε_{tot}	$un(\varepsilon_{tot})$
Lc2pphimumu_MC_2016_MagDown	0.191	0.0091	0.881	0.913	0.49	0.916	0.281	0.823	1.65E-04	8.00E-06
Lc2pphimumu_MC_2016_MagUp	0.191	0.0089	0.892	0.901	0.486	0.921	0.301	0.846	1.75E-04	8.23E-06
Lc2pphimumu_MC_2017_MagDown	0.191	0.0091	0.877	0.914	0.591	0.904	0.692	0.85	5.02E-04	1.51E-05
Lc2pphimumu_MC_2017_MagUp	0.191	0.0088	0.878	0.904	0.57	0.895	0.672	0.827	4.32E-04	1.38E-05
Lc2pphimumu_MC_2018_MagDown	0.191	0.0096	0.882	0.918	0.489	0.909	0.680	0.827	4.21E-04	1.41E-05
Lc2pphimumu_MC_2018_MagUp	0.191	0.0105	0.88	0.912	0.501	0.921	0.684	0.817	4.70E-04	1.50E-05
Lc2ppipi_mumu_MC_2016_MagDown	0.079	0.0103	0.541	0.920				0.845	8.04E-05	
Lc2ppipi_mumu_MC_2016_MagUp	0.079	0.0103	0.556	0.923				0.848	8.59E-05	
Lc2ppipi_mumu_MC_2017_MagDown	0.079	0.0097	0.483	0.926				0.852	2.24E-04	
Lc2ppipi_mumu_MC_2017_MagUp	0.079	0.0099	0.531	0.922				0.854	2.12E-04	
Lc2ppipi_mumu_MC_2018_MagDown	0.079	0.0110	0.542	0.925				0.85	2.08E-04	
Lc2ppipi_mumu_MC_2018_MagUp	0.079	0.0110	0.565	0.929				0.853	2.18E-04	

Bibliography

[1] R. P. Feynman and M. Gell-Mann, "Theory of the fermi interaction," *Phys. Rev.*, vol. 109, pp. 193–198, 1 Jan. 1958. DOI: 10.1103/PhysRev.109.193.

[2] S. Weinberg, "A model of leptons," *Phys. Rev. Lett.*, vol. 19, pp. 1264–1266, 21 Nov. 1967. DOI: 10.1103/PhysRevLett.19.1264.

[3] S. L. Glashow, J. Iliopoulos, and L. Maiani, "Weak interactions with lepton-hadron symmetry," *Phys. Rev. D*, vol. 2, pp. 1285–1292, 7 Oct. 1970. DOI: 10.1103/PhysRevD.2.1285.

[4] A. Salam and J. Ward, "Electromagnetic and weak interactions," *Physics Letters*, vol. 13, no. 2, pp. 168–171, 1964, ISSN: 0031-9163. DOI: 10.1016/0031-9163(64)90711-5.

[5] B. Abi *et al.*, "Measurement of the positive muon anomalous magnetic moment to 0.46 ppm," *Phys. Rev. Lett.*, vol. 126, p. 141 801, 14 Apr. 2021. DOI: 10.1103/PhysRevLett.126.141801.

[6] S. Borsanyi, Z. Fodor, J. N. Guenther, *et al.*, "Leading hadronic contribution to the muon magnetic moment from lattice qcd," *Nature*, vol. 593, no. 7857, pp. 51–55, May 2021, ISSN: 1476-4687. DOI: 10.1038/s41586-021-03418-1.

[7] Fukuda, Y. et al. Super-Kamiokande Collaboration, "Evidence for oscillation of atmospheric neutrinos," *Phys. Rev. Lett.*, vol. 81, pp. 1562–1567, 8 Aug. 1998. DOI: 10.1103/PhysRevLett.81.1562.

[8] L. Canetti, M. Drewes, and M. Shaposhnikov, "Matter and antimatter in the universe," *New Journal of Physics*, vol. 14, no. 9, p. 095 012, Sep. 2012. DOI: 10.1088/1367-2630/14/9/095012.

[9] M. Dine and A. Kusenko, "Origin of the matter-antimatter asymmetry," *Rev. Mod. Phys.*, vol. 76, pp. 1–30, 1 Dec. 2003. DOI: 10.1103/RevModPhys.76.1.

[10] H. Andernach and F. Zwicky, *English and spanish translation of zwicky's (1933) the redshift of extragalactic nebulae*, 2017. DOI: 10.48550/arXiv.1711.01693.

[11] E. Corbelli and P. Salucci, "The extended rotation curve and the dark matter halo of M33," *Monthly Notices of the Royal Astronomical Society*, vol. 311, no. 2, pp. 441–447, Jan. 2000. DOI: 10.1046/j.1365-8711.2000.03075.x.

[12] S. M. Carroll, W. H. Press, and E. L. Turner, "The cosmological constant," *Annual Review of Astronomy and Astrophysics*, vol. 30, no. 1, pp. 499–542, 1992. DOI: 10.1146/annurev.aa.30.090192.002435.

[13] A. G. Riess, A. V. Filippenko, P. Challis, *et al.*, "Observational evidence from supernovae for an accelerating universe and a cosmological constant," *The Astronomical Journal*, vol. 116, no. 3, p. 1009, Sep. 1998. DOI: 10.1086/300499.

[14] L. Calibbi and G. Signorelli, "Charged lepton flavour violation: An experimental and theoretical introduction," *La Rivista del Nuovo Cimento*, vol. 41, no. 2, pp. 71–174, Feb. 2018. DOI: 10.1393/ncr/i2018-10144-0.

[15] A. M. Baldini, Y. Bao, E. Baracchini, *et al.*, "Search for the lepton flavour violating decay $\mu^+ \to e^+\gamma$ with the full dataset of the meg experiment," *The European Physical Journal C*, vol. 76, no. 8, p. 434, Aug. 2016. DOI: 10.1140/epjc/s10052-016-4271-x.

[16] U. Bellgardt, G. Otter, R. Eichler, *et al.*, "Search for the decay $\mu^+ \to e^+e^+e^-$," *Nuclear Physics B*, vol. 299, no. 1, pp. 1–6, 1988. DOI: 10.1016/0550-3213(88)90462-2.

[17] R. Aaij et al. LHCb Collaboration, *Physics case for an LHCb Upgrade II - Opportunities in flavour physics, and beyond, in the HL-LHC era*, 2019. arXiv: 1808.08865 [hep-ex].

[18] S. F. Novaes, "Standard model: An Introduction," in *10th Jorge Andre Swieca Summer School: Particle and Fields*, Jan. 1999, pp. 5–102. DOI: 10.48550/arXiv.hep-ph/0001283.

[19] P. D. Group, "Review of Particle Physics," *Progress of Theoretical and Experimental Physics*, vol. 2022, no. 8, p. 083C01, Aug. 2022. DOI: 10.1093/ptep/ptac097.

[20] M. Golz, G. Hiller, and T. Magorsch, "Probing for new physics with rare charm baryon (Λ_c, Ξ_c, Ω_c) decays," *Journal of High Energy Physics*, vol. 2021, no. 9, p. 208, 2021. DOI: 10.1007/JHEP09(2021)208.

[21] R. Aaij et al. LHCb Collaboration, "Observation of D^0 Meson Decays to $\pi^+\pi^-\mu^+\mu^-$ and $K^+K^-\mu^+\mu^-$ Final States," *Phys. Rev. Lett.*, vol. 119, p. 181 805, 18 Oct. 2017. DOI: 10.1103/PhysRevLett.119.181805.

[22] L. Cappiello, O. Catà, and G. D'Ambrosio, "Standard Model prediction and new physics tests for $D^0 \to h_1^+ h_2^- \ell^+\ell^-$ ($h = \pi, K; \ell = e, \mu$)," *Journal of High Energy Physics*, vol. 2013, no. 4, p. 135, 2013, ISSN: 1029-8479. DOI: 10.1007/JHEP04(2013)135.

[23] S. de Boer and G. Hiller, "Null tests from angular distributions in $D \to P_1P_2l^+l^-$, $l = e$, μ decays on and off peak," *Phys. Rev. D*, vol. 98, p. 035 041, 3 Aug. 2018. DOI: 10.1103/PhysRevD.98.035041.

[24] S. Fajfer, S. Prelovsek, and P. Singer, "Rare charm meson decays $D \to Pl^+l^-$ and $c \to ul^+l^-$ in the standard model and the minimal supersymmetric standard model," *Phys. Rev. D*, vol. 64, p. 114 009, 11 Nov. 2001. DOI: 10.1103/PhysRevD.64.114009.

[25] S. Fajfer, N. Košnik, and S. Prelovšek, "Updated constraints on new physics in rare charm decays," *Phys. Rev. D*, vol. 76, p. 074 010, 7 Oct. 2007. DOI: 10.1103/PhysRevD.76.074010.

[26] A. Paul, I. I. Bigi, and S. Recksiegel, "On $D \to X_u l^+ l^-$ within the Standard Model and frameworks like the littlest Higgs model with T Parity," *Phys. Rev. D*, vol. 83, p. 114 006, 11 Jun. 2011. DOI: 10.1103/PhysRevD.83.114006.

[27] S. de Boer and G. Hiller, "Flavor and new physics opportunities with rare charm decays into leptons," *Phys. Rev. D*, vol. 93, p. 074 001, 7 Apr. 2016. DOI: 10.1103/PhysRevD.93.074001.

[28] R. Aaij et al. LHCb Collaboration, "Searches for 25 rare and forbidden decays of D^+ and D_s^+ mesons," *Journal of High Energy Physics*, vol. 2021, no. 6, p. 44, 2021. DOI: 10.1007/JHEP06(2021)044.

[29] J. P. Lees, V. Poireau, V. Tisserand, *et al.*, "Searches for rare or forbidden semileptonic charm decays," *Phys. Rev. D*, vol. 84, p. 072 006, 7 Oct. 2011. DOI: 10.1103/PhysRevD.84.072006.

[30] R. Aaij et al. LHCb Collaboration, "Search for the rare decay of charmed baryon Λ_c^+ into the $p\mu^+\mu^-$ final state," *Phys. Rev. D*, vol. 110, p. 052 007, 5 Sep. 2024. DOI: 10.1103/PhysRevD.110.052007.

[31] G. Burdman, E. Golowich, J. Hewett, and S. Pakvasa, "Rare charm decays in the standard model and beyond," *Phys. Rev. D*, vol. 66, p. 014 009, 1 Jul. 2002. DOI: 10.1103/PhysRevD.66.014009.

[32] A. Paul, I. I. Bigi, and S. Recksiegel, "$D^0 \to \gamma\gamma$ and $D^0 \to \mu^+\mu^-$ rates on an unlikely impact of the littlest Higgs model with T parity," *Phys. Rev. D*, vol. 82, p. 094 006, 9 Nov. 2010. DOI: 10.1103/PhysRevD.82.094006.

[33] R. Aaij et al. LHCb Collaboration, "Search for Rare Decays of D^0 Mesons into Two Muons," *Phys. Rev. Lett.*, vol. 131, p. 041 804, 4 Jul. 2023. DOI: 10.1103/PhysRevLett.131.041804.

[34] M. Petrič, M. Starič, I. Adachi, *et al.*, "Search for leptonic decays of D^0 mesons," *Phys. Rev. D*, vol. 81, p. 091 102, 9 May 2010. DOI: 10.1103/PhysRevD.81.091102.

[35] R. Aaij et al. LHCb Collaboration, "Search for the lepton-flavour violating decay $D_0 \to e^\pm\mu^\mp$," *Physics Letters B*, vol. 754, pp. 167–175, 2016. DOI: 10.1016/j.physletb.2016.01.029.

[36] J. P. Lees, V. Poireau, V. Tisserand, *et al.*, "Search for Rare or Forbidden Decays of the D^0 Meson," *Phys. Rev. Lett.*, vol. 124, p. 071 802, 7 Feb. 2020. DOI: 10.1103/PhysRevLett.124.071802.

[37] R. Aaij et al. LHCb Collaboration, "Measurement of Angular and CP Asymmetries in $D^0 \to \pi^+\pi^-\mu^+\mu^-$ and $D^0 \to K^+K^-\mu^+\mu^-$ Decays," *Phys. Rev. Lett.*, vol. 121, p. 091 801, 9 Aug. 2018. DOI: 10.1103/PhysRevLett.121.091801.

[38] B. Diaz, M. Schmaltz, and Y.-M. Zhong, "The leptoquark hunter's guide: Pair production," *Journal of High Energy Physics*, vol. 97, no. 10, pp. 1029–8479, Oct. 2017. DOI: 10.1007/jhep10(2017)097.

[39] R. Aaij et al. LHCb Collaboration, "Prompt charm production in pp collisions at $\sqrt{s} = 7$ TeV," *Nuclear Physics B*, vol. 871, no. 1, pp. 1–20, 2013, ISSN: 0550-3213. DOI: 10.1016/j.nuclphysb.2013.02.010.

[40] R. Aaij et al. LHCb Collaboration, "Measurements of prompt charm production cross-sections in pp collisions at $\sqrt{s} = 13$ TeV," *Journal of High Energy Physics*, vol. 2016, no. 3, p. 159, Mar. 2016, ISSN: 1029-8479. DOI: 10.1007/JHEP03(2016)159.

[41] R. Aaij et al. LHCb Collaboration, "Measurement of the b-Quark Production Cross Section in 7 and 13 TeV pp Collisions," *Phys. Rev. Lett.*, vol. 118, p. 052 002, 5 Feb. 2017. DOI: 10.1103/PhysRevLett.118.052002.

[42] R. Aaij et al. LHCb Collaboration, "Measurement of the $D^\pm$ production asymmetry in 7 TeV pp collisions," *Physics Letters B*, vol. 718, no. 3, pp. 902–909, 2013, ISSN: 0370-2693. DOI: 10.1016/j.physletb.2012.11.038.

[43] R. Aaij et al. LHCb Collaboration, "Measurement of $D_s^{\pm}$ production asymmetry in pp collisions at $\sqrt{s} = 7$ and 8 TeV," *Journal of High Energy Physics*, vol. 2018, no. 8, p. 8, Aug. 2018, ISSN: 1029-8479. DOI: 10.1007/JHEP08(2018)008.

[44] R. Lindner, "LHCb layout_2," LHCb Collection., 2008. [Online]. Available: https://cds.cern.ch/record/1087860.

[45] I. Bediaga, J. M. De Miranda, F. Ferreira Rodrigues, *et al.*, "Framework TDR for the LHCb Upgrade: Technical Design Report," CENR, Tech. Rep., 2012. [Online]. Available: https://cds.cern.ch/record/1443882.

[46] R. Antunes-Nobrega et al. LHCb Collaboration, *LHCb reoptimized detector design and performance: Technical Design Report* (Technical design report. LHCb). Geneva: CERN, 2003. [Online]. Available: http://cds.cern.ch/record/630827.

[47] T. Ruf, "Three modules of the LHCb Vertex Locator in the H8 test beam in the North Area," LHCb Collection., 2008. [Online]. Available: http://cds.cern.ch/record/1118792.

[48] W. Baldini, J. Blouw, S. Blusk, *et al.*, "Overview of lhcb alignment," *Proceedings of the 1st LHC Detector Alignment Workshop*, Jan. 2007.

[49] M. Witek, "VELO-TT matching and momentum determination at Level-1 trigger," Tech. Rep., Aug. 2003.

[50] R. Aaij et al. LHCb Collaboration, "Measurement of the track reconstruction efficiency at LHCb," *JINST*, vol. 10, no. 02, P02007, 2015. DOI: 10.1088/1748-0221/10/02/P02007. arXiv: 1408.1251 [hep-ex].

[51] R. Aaij et al. LHCb Collaboration, "Measurement of the electron reconstruction efficiency at lhcb," *Journal of Instrumentation*, vol. 14, no. 11, P11023, Nov. 2019. DOI: 10.1088/1748-0221/14/11/P11023.

[52] P. R. Barbosa-Marinho, I. Bediaga, G. Cernicchiaro, *et al.*, *LHCb muon system: Technical Design Report* (Technical design report. LHCb). Geneva: CERN, 2001. [Online]. Available: https://cds.cern.ch/record/504326.

[53] D. Derkach, M. Hushchyn, T. Likhomanenko, *et al.*, "Machine-learning-based global particle-identification algorithms at the lhcb experiment," *Journal of Physics: Conference Series*, vol. 1085, no. 4, p. 042 038, Sep. 2018. DOI: 10.1088/1742-6596/1085/4/042038.

[54] R. Aaij et al. LHCb Collaboration, "Design and performance of the LHCb trigger and full real-time reconstruction in Run 2 of the LHC," *Journal of Instrumentation*, vol. 14, no. 04, P04013, Apr. 2019. DOI: 10.1088/1748-0221/14/04/P04013.

[55] A. Martin Sanchez, P. Robbe, and M.-H. Schune, "Performances of the LHCb L0 Calorimeter Trigger," CERN, Geneva, Tech. Rep., 2012. [Online]. Available: https://cds.cern.ch/record/1407893.

[56] Torbjörn Sjöstrand and Stephen Mrenna and Peter Skands, "A brief introduction to pythia 8.1," *Computer Physics Communications*, vol. 178, no. 11, pp. 852–867, 2008, ISSN: 0010-4655. DOI: https://doi.org/10.1016/j.cpc.2008.01.036.

[57] Torbjörn Sjöstrand, "The pythia event generator: Past, present and future," *Computer Physics Communications*, vol. 246, p. 106 910, 2020, ISSN: 0010-4655. DOI: 10.1016/j.cpc.2019.106910.

[58] M. Clemencic, G. Corti, S. Easo, *et al.*, "The lhcb simulation application, gauss: Design, evolution and experience," *Journal of Physics: Conference Series*, vol. 331, no. 3, p. 032 023, Dec. 2011. DOI: 10.1088/1742-6596/331/3/032023.

[59] D. J. Lange, "The evtgen particle decay simulation package," *Nuclear Instruments and Methods in Physics Research Section A: Accelerators, Spectrometers, Detectors and Associated Equipment*, vol. 462, no. 1, pp. 152–155, 2001, BEAUTY2000, Proceedings of the 7th Int. Conf. on B-Physics at Hadron Machines, ISSN: 0168-9002. DOI: https://doi.org/10.1016/S0168-9002(01)00089-4.

[60] W. Slominski, H. Abramowicz, and A. Levy, "Nlo photon parton parametrization using ee and ep data," *The European Physical Journal C - Particles and Fields*, vol. 45, no. 3, pp. 633–641, Mar. 2006, ISSN: 1434-6052. DOI: 10.1140/epjc/s2005-02458-7.

[61] D. J. Lange, "The evtgen particle decay simulation package," *Nuclear Instruments and Methods in Physics Research Section A: Accelerators, Spectrometers, Detectors and Associated Equipment*, vol. 462, no. 1, pp. 152–155, 2001, BEAUTY2000, Proceedings of the 7th Int. Conf. on B-Physics at Hadron Machines, ISSN: 0168-9002. DOI: https://doi.org/10.1016/S0168-9002(01)00089-4.

[62] C. L. da Silva. "Magnet stations model." (2023), [Online]. Available: https://twiki.cern.ch/twiki/pub/LHCb/LHCbMagnetStation/MagnetStationModel.png (visited on 11/09/2024).

[63] R. Aaij et al. LHCb Collaboration, "Framework TDR for the LHCb Upgrade II: Opportunities in flavour physics, and beyond, in the HL-LHC era," CERN, Geneva, Tech. Rep., 2021. [Online]. Available: https://cds.cern.ch/record/2776420.

[64] M. Frank, F. Gaede, M. Petric, and A. Sailer, *Aidasoft dd4hep*, Oct. 2018. DOI: 10.5281/zenodo.592244. [Online]. Available: http://dd4hep.cern.ch/.

[65] K. Abe, K. Abe, T. Akagi, *et al.*, "Measurement of R_b Using a Vertex Mass Tag," *Phys. Rev. Lett.*, vol. 80, pp. 660–665, 4 Jan. 1998. DOI: 10.1103/PhysRevLett.80.660.

[66] T. Chen and C. Guestrin, "Xgboost: A scalable tree boosting system," in *Proceedings of the 22nd ACM SIGKDD International Conference on Knowledge Discovery and Data Mining*, ser. KDD '16, San Francisco, California, USA: Association for Computing Machinery, 2016, pp. 785–794, ISBN: 9781450342322. DOI: 10.1145/2939672.2939785.

[67] V. Krutelyov, "Search for Supersymmetry Using Rare $B^0_{s(d)} \to \mu^+\mu^-$ Decays at CDF Run II," Doctoral dissertation, Texas A&M University, Dec. 2005.

[68] A. Abulencia et al. CDF Collaboration, "Search for $B^0_s \to \mu^+\mu^-$ and $B^0_d \to \mu^+\mu^-$ Decays in $p\overline{p}$ Collisions with CDF II," *Phys. Rev. Lett.*, vol. 95, p. 221 805, 22 Nov. 2005. DOI: 10.1103/PhysRevLett.95.221805.

[69] L. Gavardi, "Search for lepton flavour violation in τ decays at the LHCb experiment," Presented 28 Nov 2013, Milan Bicocca U., 2013. [Online]. Available: https://cds.cern.ch/record/1645251.

[70] M. Pivk and F. Le Diberder, "Plots: A statistical tool to unfold data distributions," *Nuclear Instruments and Methods in Physics Research Section A: Accelerators, Spectrometers, Detectors and Associated Equipment*, vol. 555, no. 1, pp. 356–369, 2005, ISSN: 0168-9002. DOI: 10.1016/j.nima.2005.08.106.

[71] O. Lupton, L. Anderlini, B. Sciascia, and V. Gligorov, "Calibration samples for particle identification at LHCb in Run 2," CERN, Geneva, Tech. Rep., 2016. [Online]. Available: http://cds.cern.ch/record/2134057.

[72] R. Aaij et al. LHCb Collaboration, "Selection and processing of calibration samples to measure the particle identification performance of the lhcb experiment in run 2," *EPJ Techniques and Instrumentation*, vol. 6, no. 1, p. 1, Feb. 2019, ISSN: 2195-7045. DOI: 10.1140/epjti/s40485-019-0050-z.

[73] M. P. et al. Belle Collaboration, "Search for leptonic decays of D^0 mesons," *Phys. Rev. D*, vol. 81, p. 091 102, 9 May 2010. DOI: 10.1103/PhysRevD.81.091102.

[74] D. C. on behalf of the LHCb Collaboration, *Pidcalib2*, 2023. [Online]. Available: https://gitlab.cern.ch/lhcb-rta/pidcalib2.

[75] L. Anderlini *et al.*, "The pidcalib package," CERN, Tech. Rep., 2016.

[76] T. Skwarnicki, "A study of the radiative CASCADE transitions between the Upsilon-Prime and Upsilon resonances," Ph.D. dissertation, Cracow, INP, 1986.

[77] G. Cowan, K. Cranmer, E. Gross, and O. Vitells, "Asymptotic formulae for likelihood-based tests of new physics," *Eur. Phys. J. C*, vol. 71, p. 1554, 2011, [Erratum: Eur.Phys.J.C 73, 2501 (2013)]. DOI: 10.1140/epjc/s10052-011-1554-0. arXiv: 1007.1727 [physics.data-an].

[78] S. S. Wilks, "The Large-Sample Distribution of the Likelihood Ratio for Testing Composite Hypotheses," *Annals Math. Statist.*, vol. 9, no. 1, pp. 60–62, 1938. DOI: 10.1214/aoms/1177732360.

[79] A. Wald, "Tests of statistical hypotheses concerning several parameters when the number of observations is large," *Transactions of the American Mathematical Society*, vol. 54, no. 3, pp. 426–482, 1943, ISSN: 00029947, 10886850. [Online]. Available: http://www.jstor.org/stable/1990256 (visited on 10/10/2024).

[80] E. Rodrigues *et al.*, "The Scikit HEP Project – overview and prospects," *EPJ Web Conf.*, vol. 245, C. Doglioni, D. Kim, G. A. Stewart, L. Silvestris, P. Jackson, and W. Kamleh, Eds., p. 06 028, 2020. DOI: 10.1051/epjconf/202024506028. arXiv: 2007.03577 [physics.comp-ph].

[81] J. Eschle, A. Puig Navarro, R. Silva Coutinho, and N. Serra, "Zfit: Scalable pythonic fitting," *SoftwareX*, vol. 11, p. 100 508, 2020, ISSN: 2352-7110. DOI: 10.1016/j.softx.2020.100508.

[82] M. Marinangeli, J. Eschle, E. Rodrigues, A. Desai, H. Schreiner, and B. Pollack, *Scikit-hep/hepstats: Python 3.11 support*, version v0.7.0, Jun. 2023. DOI: 10.5281/zenodo.8070070.

[83] A. Novak, H. Schreiner, and M. Feickert, *Mplhep*, version v0.3.35, Feb. 2024. DOI: 10.5281/zenodo.10697954.

[84] N. L. JOHNSON, "SYSTEMS OF FREQUENCY CURVES GENERATED BY METHODS OF TRANSLATION," *Biometrika*, vol. 36, no. 1-2, pp. 149–176, Jun. 1949, ISSN: 0006-3444. DOI: 10.1093/biomet/36.1-2.149.